

https://dspace.org/

Supersonic and transonic viscous corner flows

Naidoo, Prinal

2012-07-06
http://hdl.handle.net/10539/11629

Downloaded from a DSpace repository. https://dspace.org/

SUPERSONIC AND TRANSONIC VISCOUS CORNER FLOWS

Prinal Naidoo

A thesis submitted to the Faculty of Engineering and the Built Environment, University of the Witwatersrand, Johannesburg, in fulfillment of the requirements for the degree of Doctor of Philosophy.

Johannesburg, December 2011

Declaration

I, Prinal Naidoo, declare that the content of this report is my own unaided work, unless stated otherwise, and that I own copyright in this. This report also conforms to the requirements for report writing, as prescribed by the School of Mechanical, Aeronautical and Industrial Engineering of the University of the Witwatersrand.

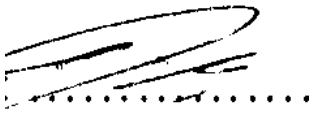

Prinal Naidoo

Date: 12/12 /2011

Acknowledgments

To GOD and the late Shri Mataji Nirmala Devi, thank you for the spiritual support, for always providing me with the strength, energy and determination needed to get through the trying times of this project.

To my dad, mum, brother and sister, thank you for the overwhelming love and support that you have given me throughout my life.

To Professor B.W. Skews, thank you for allowing me to do this project under your supervision. Your help, guidance and advice will forever be greatly appreciated.

To Dr. Igle Geldhill and the Fluxion National Bursary program, thank you for the continued financial support during my postgraduate studies.

When once you have tasted flight, you will forever walk the earth with your eyes turned skyward, for there you have been and there you will always long to return….

Leonardo da Vinci

Abstract

An investigation into steady state supersonic and transonic viscous corner flows has been conducted. The supersonic research focused on the development of the three shock structure along various fillet and sharp corner geometries, specifically the formation and growth of the shear layers that result from the Mach reflection. The resultant effects of these shear layers on the pressure distributions, shear stresses and the changes in Mach numbers were analyzed together with the shock wave boundary layer interaction. Experimental supersonic work includes the use of the oil film flow visualization technique to visualize the surface flow patterns. The transonic research focused on numerically verifying the existence of the transonic shock wave within a corner configuration. The supersonic and transonic flows considered are symmetric about the corner bisector. These flows are numerically calculated by using the CFD code of Fluent and include the use of standard turbulence models. The geometries analyzed resembled simplified wing body-fuselage and wing-winglet/wingtip intersections for both supersonic and transonic aircraft. These geometries had varying geometric parameters. The supersonic results showed that the inclusion of a fillet profile between two aerodynamic surfaces or wing sections results in the delay of the formation of the Mach reflection and shear layer. Neglecting the effect of the fillet profile (sharp corner) resulted in the formation of the Mach reflection and shear layer starting at the leading edge of the geometry, hence a greater increase in pressure and shear stress was seen on the sharp corner geometries. The impingement of the reflected shock waves on the boundary layer results in a large variation in the boundary layer thickness for the sharp corner geometries however no separation is observed. The supersonic experimental work validates the numerical results produced by accurately depicting the surface flow patterns. The transonic numerical results verified the existence of a transonic shock wave within a corner configuration for all the geometries analyzed. The shock wave boundary layer interaction was strong enough to cause reversed flow and separation within the transonic corner.

Published Work

Certain aspects of this thesis have been published in the following references:

- NAIDOO P. SKEWS B.W. 2009. ***Flow features on supersonic bodies with camber, dihedral and fillets*****.** 27th International Symposium on Shock Waves (ISSW 27). July 19-23. St. Petersburg, Russia. Awarded the prize for best student paper.

- NAIDOO P. SKEWS B.W. 2011. ***Supersonic viscous corner flows***. Proceedings of the Institution of Mechanical Engineers, Part G: Journal of Aerospace Engineering. In Press. DOI: 10.1177/0954410011416709

Table of Contents

Declaration i
Acknowledgments ii
Abstract iii
Published Work iv
Table of Contents v
List of Figures viii
List of Tables xiv
List of Symbols xv
1. Introduction 1
2. Objectives, Scope and Organization 3
2.1 Objectives 3
2.1.1 Supersonic Flow Research 3
2.1.2 Transonic Flow Research 4
2.2 Scope 4
2.3 Organization 5
3. Literature Review 6
3.1 Shock Wave Theory 6
3.1.1 Normal Shock Waves 6
3.1.2 Oblique Shock Waves 8
3.1.3 Shock Wave Reflections 10
3.1.4 Shock Wave Boundary Layer Interaction (SWBLI) 12
3.2 Supersonic Corner Flows 15
3.2.1 Background 15
3.2.2 Early Research 15
3.3 Transonic Corner Flows 21
3.3.1 Background 21
3.3.2 Transonic Shock Waves 21
3.3.3 Previous Research 23
3.3.4 Transonic Airfoils 24

3.3.4.1 Rae 2822 25
3.3.4.2 Onera M6 25
3.4 Surface Flow Visualization 27
3.4.1 Oil Film Technique 27
4. Supersonic and Transonic Geometries 30
4.1 Computational Transonic Geometries 30
4.1.1 Straight Wing with Camber and Dihedral 30
4.1.2 Swept Wing with Camber and Dihedral 31
4.2 Computational Supersonic Geometries 33
4.2.1 Straight Wing with Camber and Dihedral 33
4.2.2 Straight Wing with Varying Fillet Radii 34
4.2.3 Straight Wing with Varying Camber 35
4.3 Experimental Supersonic Test Specimens 36
5. Experimentation 38
5.1 Experimental Facilities 38
5.1.1 Supersonic Wind Tunnel and Components 38
5.2 Surface Flow Visualization 40
5.2.1 Oil Film Technique 40
5.3 Summary of Experimental Analysis 41
6. Numerical Simulation 42
6.1 Pre - Processing 43
6.1.1 Supersonic and Transonic Geometries 43
6.1.2 Domain Boundaries 43
6.1.3 Boundary Layer and Volume Mesh Generation 44
6.2 Processing 47
6.2.1 Solver Options and Boundary Conditions 47
6.2.2 Convergence 49
6.2.3 Mesh Adaptation 51
6.2.4 Mesh Independence 54
6.2.5 Turbulence Modeling 57
6.3 Summary of Numerical Analysis 59

6.3.1 Supersonic Analysis 59
6.3.2 Transonic Analysis 61
7. Supersonic Numerical Results and Discussions 62
7.1 General formation and development of the shock structure within a supersonic corner 64
7.2 Iso surfaces showing the formation and development of the shock structure within a supersonic corner 69
7.3 Pressure, shear stress and Mach number distributions 76
7.4 Influence of varying dihedral angles and thickness/chord ratios 80
7.5 Influence of varying fillet radii and Mach numbers on the shock formation 85
7.5.1 Variation of pressure associated with different fillet radii and Mach numbers 85
7.5.2 Influence of varying fillet radii and Mach number on the transition point 88
7.6 Influence of varying camber profiles on the shock formation 89
7.7 Shock Wave-Boundary Layer Interaction 92
7.8 Turbulence Modeling: Viscous vs. Inviscid 96
8. Supersonic Experimental Images and Numerical Surface Streamlines, Results and Discussion 99
9. Transonic Numerical Results and Discussion 105
9.1 General formation of the transonic shock wave within a corner configuration 106
9.1.1 Rae 2822 106
9.1.2 Onera M6 113
9.2 Numerical surface streamlines and vector plots 119
10. Conclusions 121
11. Recommendations 123
12. References 124
Appendix A Supersonic Wind Tunnel Components 126
Appendix B Supersonic Results, Iso Surfaces of Mach number 140
Electronic Appendix 146

List of Figures

Figure 1.1: Wing body representation on a SR 71 2
Figure 3. 1: Simplified diagram of a normal shock wave and the associated changes in the flow properties 6
Figure 3. 2: Schematic representation of an oblique shock wave 8
Figure 3. 3: Schematic depicting oblique shock wave geometry [1] 9
Figure 3. 4: Flow chart depicting the different types of shock wave reflections 10
Figure 3. 5: Schematic representation of Regular (left) and Irregular (right) reflections . 11
Figure 3. 6: Schematic representation of shock wave boundary layer interaction on a flat plate 13
Figure 3. 7: Velocity profiles showing attached and separated flow 14
Figure 3. 8: Supersonic corner flow with Mach reflection on two plane wedges 16
Figure 3. 9: Comparison of numerical and experimental corner flows, (a) Numerical contour plots, (b) Experimental laser vapour screen flow visualization 20
Figure 3.10: Wing-winglet intersections, (a) Blended winglet, (b) Wingtip fence, (c) Spiroids winglet 22
Figure 3. 11: Progression of shock waves over an airfoil in transonic flow 23
Figure 3. 12: Schematic representation of the Rae 2822 airfoil 25
Figure 3. 13: Schematic representation of the Onera M6 airfoil 26
Figure 4. 1: Transonic straight wing geometries, (a) Fillet profile, (b) Sharp corner profile 31
Figure 4. 2: Transonic swept wing geometries, (a) Fillet profile, (b) Sharp corner profile 32
Figure 4. 3: Schematic showing variation in thickness for the sharp corner geometries.. 33
Figure 4. 4: Supersonic geometries, (a) Fillet profile, (b) Sharp Corner profile 34
Figure 4. 5: Varying fillet radii geometries 35
Figure 4. 6: Wedge and Circular arc geometries with the same leading edge angle 36
Figure 4. 7: Solid edge drawings of test specimens 37
Figure 4. 8: Manufactured experimental test specimens 37

Figure 5. 1: Schematic representation of the supersonic wind tunnel and internal components 38
Figure 6. 1: Illustrations of (a) transonic and (b) supersonic geometries 43
Figure 6. 2: Computational domain boundaries 43
Figure 6. 3: Volume meshes taken along symmetry plane, (a) Supersonic mesh, (b) Transonic mesh 46
Figure 6. 4: Graph of Wall y^+ vs. position on geometry 47
Figure 6. 5: Plot of residuals showing convergence and adaptation 49
Figure 6. 6: Plot of drag coefficient showing convergence 50
Figure 6. 7: Supersonic mesh refinement, (a) Initial Mesh (b) 1st Adapted mesh (c) 2nd Adapted mesh 52
Figure 6. 8: Transonic mesh refinement, (a) Initial Mesh, (b) 1st adapted mesh, (c) 2nd Adapted mesh 53
Figure 6. 9: Graphs of Pressure, Temperature and Mach number showing mesh independence for the 90° circular arc fillet (a-c) at M 3.2 and Onera M6 sharp corner (d-f) geometries at Mach 0.9 56
Figure 6. 10: Graphs of Pressure, Temperature and Mach number for different turbulence models for the 90° fillet and sharp corner geometries at Mach 3.0 58
Figure 7. 1: Illustration of chordwise and spanwise directions 63
Figure 7. 2: Shock structure cross sections for the 90° fillet geometry, (a) Mach number line contour plots, (b) Numerical schlieren 66
Figure 7. 3: Shock structure cross sections for the 90° sharp corner geometry, (a) Mach number line contour plots, (b) Numerical schlieren 67
Figure 7. 4: Shock structure cross sections for the 135° fillet geometry, (a) Mach number line contour plots, (b) Numerical schlieren 68
Figure 7. 5: Iso surfaces of Mach number for the 135° dihedral angle 3% thickness/chord ratio fillet geometry, Isometric views, (a) Front, (b) Rear 71
Figure 7. 6: Iso surfaces of Mach number for the 90° dihedral angle 10% thickness/chord ratio fillet geometry, Isometric views, (a) Front, (b) Rear 72
Figure 7. 7: Iso surfaces of Mach number for the 90° dihedral angle 10% thickness/chord ratio sharp corner geometry, Isometric views, (a) Front, (b) Rear 73

Figure 7. 8: Graphs of Mach stem length for varying t/c ratios and dihedral angles, (a) fillet profile, (b) sharp corner profile 75
Figure 7. 9: Graphs of variation in transition point for varying t/c ratios and dihedral angles 75
Figure 7. 10: Surface properties for the 90° fillet geometry, (a) Pressure (Pa), (b) Shear stress (Pa), (c) Mach number 78
Figure 7. 11: Surface properties for the 90° sharp corner geometry, (a) Pressure (Pa), (b) Shear stress (Pa), (c) Mach number 78
Figure 7. 12: Surface properties for 135° fillet geometry, (a) Pressure (Pa), (b) Shear stress (Pa), (c) Mach number 79
Figure 7. 13: Graphs of pressure variation for different thickness/chord ratios for the fillet (a-c) and sharp corner (d-f) geometries 81
Figure 7. 14: Graphs of pressure variation for different dihedral angles for the fillet (a-c) and sharp corner (d, e,) geometries 83
Figure 7. 15 : Graphs comparing pressure variation for the 90,120 and 135 degree fillet and sharp corner geometries for the 3 percent (a, c, e) and the 10% percent (b, d, f) t/c ratios 84
Figure 7. 16: Graphs comparing pressure variation for the sharp corner and varying fillet radii geometries for varying freestream Mach numbers, (a) Mach 2.5, (b) Mach 3.0 and (c) Mach 5.0 87
Figure 7. 17: Graph of fillet radius vs. transition point for varying Mach numbers 89
Figure 7. 18: Numerical schlieren images showing the shock structure for the (a) Circular arc and (b) Wedge geometries 91
Figure 7. 19: Boundary Layer Velocity Vectors (a) leading edge, (b) midpoint, (c) trailing edge 93
Figure 7. 20: SWBLI, Mach number contours, thickening of boundary layer for the (a) 90° fillet geometry (b) 90° sharp corner geometry 95
Figure 7. 21: Variation of pressure showing a comparison between the inviscid and viscous flow computations 98
Figure 8. 1: Experimental and surface streamlines for the 90° sharp corner geometry at M 3.0, ... 100

Figure 8. 2: Experimental and surface streamlines for the 90° fillet geometry at M 3.0, (a) Experimental top view (b) Isometric view of the surface streamlines..... 101
Figure 8. 3: Experimental and surface streamlines for the 120° fillet geometry at M3.0, (a) Experimental top view (b) Isometric view of the surface streamlines..... 103
Figure 8. 4: Experimental and surface streamlines for the 120° sharp corner geometry at M 3.0, (a) Experimental top view (b) Isometric view of the surface streamlines..... 104
Figure 9. 1: Pressure contours for the Rae 2822 straight wing fillet geometries, (a) M 0.75, (b) M 0.80, (c) M 0.85, (d) M 0.90 108
Figure 9. 2: Mach number contours taken along the symmetry plane for the Rae 2822 straight wing fillet geometries, (a) M 0.75, (b) M 0.80, (c) M 0.85, (d) M 0.90 108
Figure 9. 3: Pressure contours for the Rae 2822 straight wing sharp corner geometries, (a) M 0.75, (b) M 0.80, (c) M 0.85, (d) M 0.90..... 109
Figure 9. 4: Mach number contours taken along the symmetry plane for the Rae 2822 straight wing sharp corner geometries, (a) M 0.75, (b) M 0.80, (c) M 0.85, (d) M 0.90 109
Figure 9. 5: Pressure contours for the Rae 2822 swept wing fillet geometries, (a) M 0.75, (b) M 0.80, (c) M 0.85, (d) M 0.90 111
Figure 9. 6: Mach number contours taken along the symmetry plane for the Rae 2822 swept wing fillet geometries, (a) M 0.75, (b) M 0.80, (c) M 0.85, (d) M 0.90..... 111
Figure 9. 7: Pressure contours for the Rae 2822 swept wing sharp corner geometries, (a) M 0.75, (b) M 0.80, (c) M 0.85, (d) M 0.90..... 112
Figure 9. 8: Mach number contours taken along the symmetry plane for the Rae 2822 swept wing sharp corner geometries, (a) M 0.75, (b) M 0.80, (c) M 0.85, (d) M 0.9 112
Figure 9. 9: Pressure contours for the Onera M6 straight wing fillet geometries, (a) M 0.75, (b) M 0.80, (c) M 0.85, (d) M 0.90 114
Figure 9. 10: Mach number contours taken along the symmetry plane for the Onera M6 straight wing fillet geometries, (a) M 0.75, (b) M 0.80, (c) M 0.85, (d) M 0.90 114
Figure 9. 11: Pressure contours for the Onera M6 straight wing sharp corner geometries, (a) M 0.75, (b) M 0.80, (c) M 0.85, (d) M 0.90 115
Figure 9. 12: Mach number contours taken along the symmetry plane for the Onera M6 straight wing sharp corner geometries, (a) M 0.75, (b) M 0.80, (c) M 0.85, (d) M 0.90 115

Figure 9. 13: Pressure contours for the Onera M6 swept wing fillet geometries, (a) M 0.75, (b) M 0.80, (c) M 0.85, (d) M 0.90 117
Figure 9. 14: Mach number contours taken along the symmetry plane for the Onera M6 swept wing fillet geometries, (a) M 0.75, (b) M 0.80, (c) M 0.85, (d) M 0.90..... 117
Figure 9. 15: Pressure contours for the Onera M6 swept wing sharp corner geometries, (a) M 0.75, (b) M 0.80, (c) M 0.85, (d) M 0.90..... 118
Figure 9. 16: Mach number contours taken along the symmetry plane for the Onera M6 swept wing sharp corner geometries, (a) M 0.75, (b) M 0.80, (c) M 0.85, (d) M 0.90 .. 118
Figure 9. 17: Flow directions over the Rae 2822 airfoil, (a) Numerical surface streamlines, (b) Vector plot of Mach number 120

Figure A. 1: Wind tunnel test section 127
Figure A. 2: Reciprocating compressor 128
Figure A. 3: Storage vessel 129
Figure A. 4: Air dryer 130
Figure A. 5: Schematic representation of the settling chamber. 131
Figure A. 6: Settling chamber. 132
Figure A. 7: First throat 133
Figure A. 8: Calibration curve for the throat counter 134
Figure A. 9: Mach and Reynolds number curves for a Mach 3.0 test run 135
Figure A. 10: Experimental sting and backing plate..... 136

Figure B. 1: Iso surfaces of Mach number for the 90° dihedral angle 3 and 6% thickness/chord ratio fillet profiles, Isometric views, (a) Front, (b) Rear..... 140
Figure B. 2: Iso surfaces of Mach number for the 120° dihedral angle 3, 6, and 10% thickness/chord ratio fillet geometries, Isometric views, (a) Front, (b) Rear 141
Figure B. 3: Iso surfaces of Mach number for the 135° dihedral angle 6 and 10% thickness/chord ratio fillet geometries, Isometric views, (a) Front, (b) Rear 142
Figure B. 4: Iso surfaces of Mach number for the 90° dihedral angle 3 and 10% thickness/chord ratio sharp corner geometries, Isometric views, (a) Front, (b) Rear..... 143

Figure B. 5: Iso surfaces of Mach number for the 120° dihedral angle 3 and 10% thickness/chord ratio sharp corner geometries, Isometric views, (a) Front, (b) Rear 144
Figure B. 6: Iso surfaces of Mach number for the 135° dihedral angle 3 and 10% thickness/chord ratio sharp corner geometries, Isometric views, (a) Front, (b) Rear 145

List of Tables

Table 3. 1: Summary of cases for the transonic investigation 26
Table 4. 1: Geometric parameters for the straight wing transonic geometries 31
Table 4. 2: Geometric parameters for the swept wing transonic geometries 32
Table 4. 3: Geometric parameters for the supersonic geometries 34
Table 4. 4: Geometric parameters for the varying fillet radii geometries 35
Table 4. 5: Wedge camber profile geometric parameters 35
Table 4. 6: Classification of experimental test specimens 36
Table 5. 1: Summary of experimental analysis 41
Table 6. 1: Size functions and boundary layer mesh specifications 45
Table 6. 2: Solver options selected for the numerical analysis 48
Table 6. 3: Boundary conditions selected for the numerical analysis 48
Table 6. 4: Mesh adaptation parameters 51
Table 6. 5: Summary of turbulence modeling study 59
Table 6. 6: Summary of Mach number variation study 59
Table 6. 7: Summary of geometric parameters study 60
Table 6. 8: Summary of fillet radius change study 60
Table 6. 9: Summary of straight wing geometries 61
Table 6. 10: Summary of swept wing geometries 61

Table A. 1: Technical specifications of the supersonic wind tunnel 127
Table A. 2: Technical specifications of the compressor 128
Table A. 3: Technical Specifications of storage vessel 129
Table A. 4: Technical specifications of dryer 130
Table A. 5: Stagnation Pressure, Throat Counter and Mach numbers 135

List of Symbols

β	Wall turning angle [°]
θ	Shock deflection angle [°]
M	Mach number
M_∞	Freestream Mach number
Re	Reynolds number
T	Temperature [K]
P	Pressure [Pa]
ρ	Density
u	Velocity
γ	Ratio of specific heats
h	Enthalpy
m	Metres

Subscripts

1 Region of flow upstream of a shock wave

2 Region of flow downstream of a shock wave

1. Introduction

The relentless study of high speed aerodynamics has attracted many aerodynamicists in the past few decades. The transonic and supersonic flow regimes have witnessed the progression of major developments and projects that have changed modern day high speed research. As a result, there are significant areas of transonic and supersonic aerodynamics that are important to ensure the effective design of aircrafts or aircraft components. One of the major factors in the design process is the shock wave formation on both transonic and supersonic wing profiles, as well as the changes in the flow characteristics that result from these shock formations. For the effective design of supersonic and transonic aircraft, accurate simulation methods are required to predict aerodynamic characteristics such as surface pressure distributions, skin friction data, changes in Mach numbers as well as the shock wave boundary layer interaction. These simulation methods include the use of Computational Fluid Dynamics (CFD) to analyze the various flow regimes.

This research investigation focuses on shock wave reflections and interactions on three dimensional geometries that represent simplified supersonic and transonic wing body-fuselage and wing-winglet/wingtip intersections. These types of intersections have previously been studied as corner flow interactions. The three dimensional shock structures that result from the supersonic and transonic flow over the respective geometries are analyzed and presented. The foundation of the investigation will be based around both the numerical (CFD) and experimental (supersonic wind tunnel testing) aspects of shock wave analysis.

The new aspects of the research include viscous simulations of more realistic geometries that specifically focus on characterizing the shock wave transition criteria by varying geometric characteristics and Mach numbers. Quantitative and qualitative data on pressure gradients, flow separation and various other thermodynamic properties are also studied. Other new research avenues include studying the effect of the resultant shock structures on the pressure distributions and the shock wave boundary layer interactions.

Figure 1.1 is an image of a SR 71. The wing body-fuselage intersection is seen along the length of the aircraft (between dashed arrows) and is represented by a curved or fillet profile. The intersection of the engine and the wing is represented by a sharp corner (fillet profile is neglected). The geometries to be created for the investigation will replicate these types of intersections (fillet and sharp corner) for both supersonic and transonic aircraft.

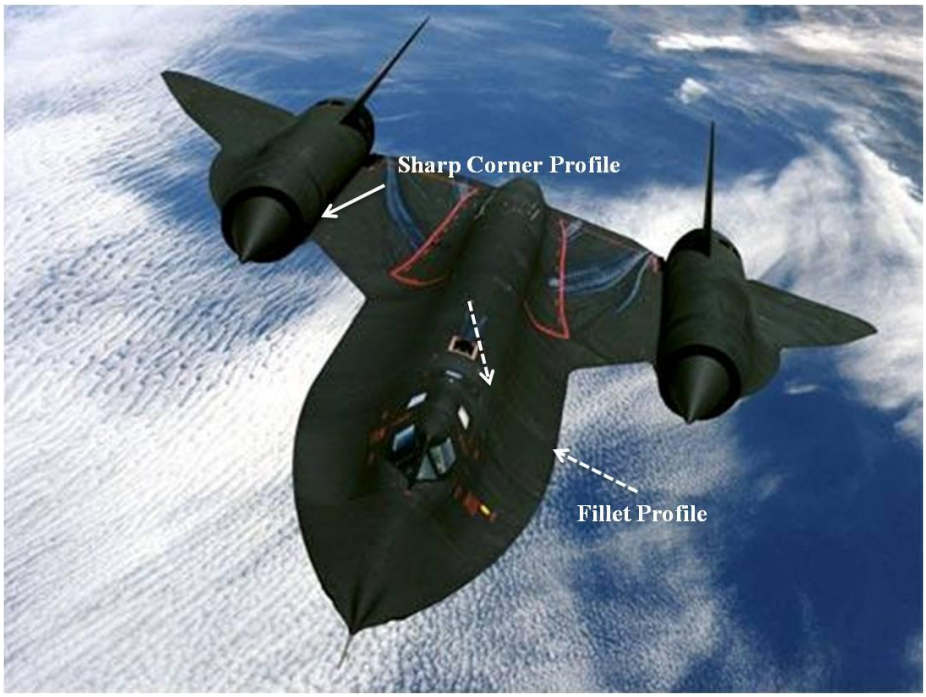

Figure 1.1: Wing body representation on a SR 71

2. Objectives, Scope and Organization

2.1 Objectives

The main objectives of this thesis are framed in such a way that the methods developed and the knowledge gained and understood from this research will serve as a platform for understanding supersonic and transonic viscous corner flow interactions.

2.1.1 Supersonic Flow Research

The main objective of the investigation is to:

- Investigate the various flow features formed on supersonic fillet and sharp corner geometries

More specifically:

- Investigate the effect of the shock discontinuity and the resultant shear layer on the surface pressure distributions

Hence:

- Analyze the boundary layer flow on the surface and deduce if this results in flow separation

This will be done both experimentally and computationally.

2.1.2 Transonic Flow Research

The main objective of the investigation is to:

- Numerically verify the existence of a transonic shock wave within a corner configuration

More specifically:

- Verify the effect of varying geometric parameters on the shock formation, the shock wave boundary layer interaction and if necessary, separation point

2.2 Scope

The experimental and computational work conducted in this thesis forms an integral part in characterizing and visualizing the three dimensional shock structures that exist within a corner configuration for both supersonic and transonic flows. More specifically, the expected contributions to knowledge are as follows:

- A comprehensive shock wave analysis into supersonic and transonic corner flow interactions;
- Analysis of the transonic shock wave that forms within a wing body-fuselage intersection or a wing-winglet intersection;
- The effect of including a viscous model into the flow computations rather than using an inviscid solver;
- Quantitative and qualitative data on pressure gradients, flow separation and other shock wave related characteristics;
- Characterization of shock structures as a function of varying geometric parameters and Mach numbers; and
- Validation of experimental and computational results for supersonic corner flow interactions.

2.3 Organization

This thesis focuses on the numerical and experimental investigations of simplified wing body-fuselage intersections for both supersonic and transonic flows. It utilizes the standard thesis organization format which includes an introduction, literature survey, experimental and numerical analysis as well as the results, discussions, conclusions and recommendations.

The experimentation chapter describes the main apparatus and all the related components used in the study. The numerical analysis chapter describes the formulation of the computational problem and the complete computational setup i.e. pre-processing, processing and post processing.

Chapters 7, 8 and 9 presents the experimental and the numerical results obtained for both the supersonic and transonic analysis.

3. Literature Review

3.1 Shock Wave Theory

It should be noted that the following sections are not detailed explanations of shock waves. They are merely qualitative discussions of shock waves and shock wave related topics, which aids in the understanding of the research conducted.

3.1.1 Normal Shock Waves

The basic definition of a normal shock wave is a shock wave that is perpendicular to the flow direction. Normal shock waves appear in many types of supersonic flow, such as flow over a flat plate, cylinder or blunt body. Another common example of a normal shock wave in supersonic nozzle flow, which is typically found in a jet or rocket engine [1]. Figure 3.1 is a simplified diagram of a normal shock wave and the relevant flow properties associated with it.

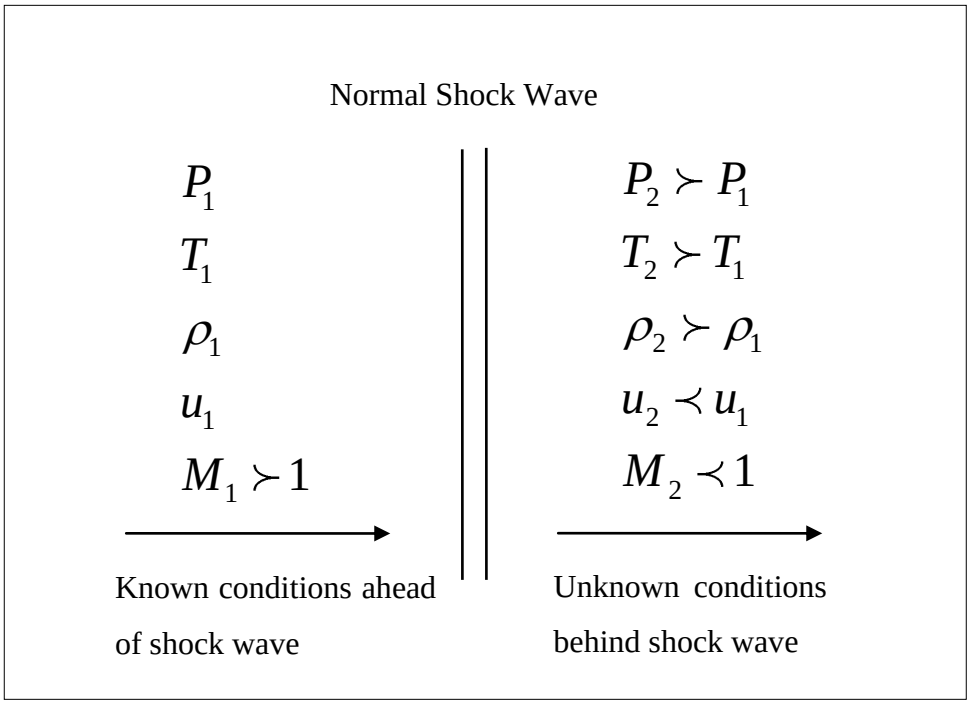

Figure 3. 1: Simplified diagram of a normal shock wave and the associated changes in the flow properties

It is assumed that the flow properties, namely pressure, temperature, density and velocity are only functions of flow direction, and as a result the shock relation is defined as one-dimensional [1]. The static pressure, temperature and density increase across the shock wave whereas the particle velocity decreases.

With reference to Figure 3.1, the basic normal shock wave equations are as follows:

Continuity: $\rho_1 u_1 = \rho_2 u_2$ (3.1)

Momentum: $P_1 + \rho_1 u_1^{\,2} = P_2 + \rho_2 u_2^{\,2}$ (3.2)

Energy: $h_1 + \frac{u_1^{\,2}}{2} = h_2 + \frac{u_2^{\,2}}{2}$ (3.3)

By using these equations and the ideal gas equation of state, the unknown flow properties behind a normal shock wave can be solved. The main flow property that is of importance is the downstream Mach number. This Mach number is given by [2]:

$$M_2^{\,2} = \left[\frac{\left(\frac{2}{\gamma - 1} + M_1^{\,2} \right)}{\left(\frac{2\gamma}{\gamma - 1} M_1^{\,2} - 1 \right)} \right] \quad (3.4)$$

Where:
γ is the ratio of specific heats

The full derivations of all the flow properties can be found in any standard gas dynamics text book or relevant course notes [2].

3.1.2 Oblique Shock Waves

Oblique shock waves are generated in the same manner as normal shock waves. They are disturbances which propagate by molecular collisions. They occur when supersonic flow is turned into itself [2]. In reality an oblique shock wave occurs in situations where the shock wave has two or three dimensional effects. Figure 3.2 is a schematic representation of an oblique shock wave. The angle θ is known as the deflection angle and is the angle of an existing corner.

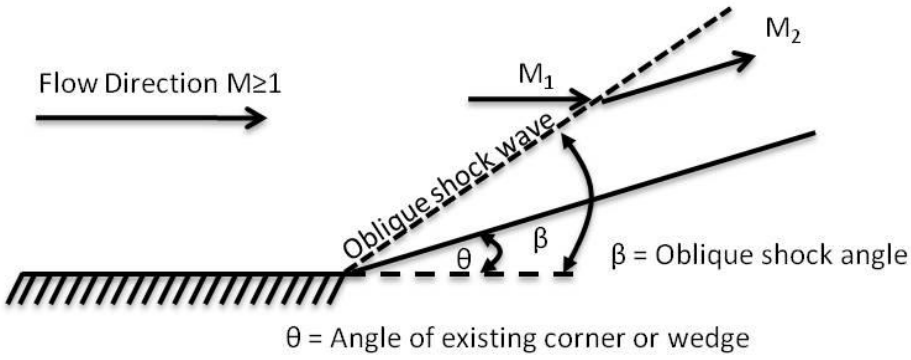

Figure 3. 2: Schematic representation of an oblique shock wave

Figure 3.3 is a simple schematic depicting oblique shock wave geometry. From the geometry shown in this figure the downstream Mach number is given as [1]:

$$M_2 = \frac{M_{n_2}}{\sin(\beta - \theta)} \tag{3.5}$$

The downstream Mach number cannot be found due to the fact that the deflection angle θ is unknown. The deflection angle is a function of the upstream Mach number M_1 and β.

The deflection angle is found using the following equation [2]:

$$\tan(\theta) = 2\cot(\beta)\left[\frac{M_1^{\,2}\sin^2(\beta)-1}{M_1^{\,2}(\gamma+\cos(2\beta))+2}\right] \tag{3.6}$$

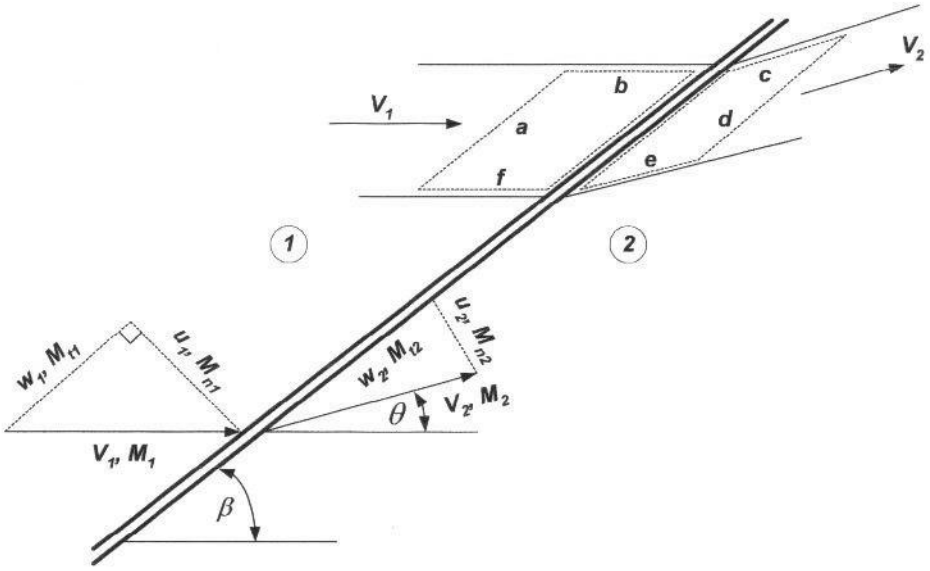

Figure 3. 3: Schematic depicting oblique shock wave geometry [1]

3.1.3 Shock Wave Reflections

The study of shock wave reflections dates back to the late 1800's at which time Ernst Mach was the first to make the important discoveries related to shock wave reflections [3]. Subsequent studies have yielded the various shock wave structures that are used in the modern era to classify each type of reflection. Following this, shock wave researchers focused on classifying the transition criteria that enabled the transition from regular to irregular reflection [3]. Figure 3.4 is a truncated flow chart depicting the shock wave reflections related to this investigation. The study of the Mach reflection will be the foundation of the supersonic investigation.

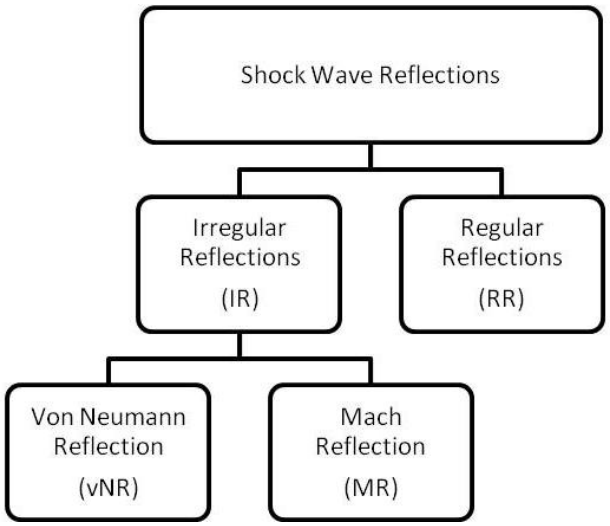

Figure 3. 4: Flow chart depicting the different types of shock wave reflections

Two types of reflections result from the interaction of an incident wave and a wedge surface and these are dependent on the incident Mach number and the reflecting wedge angle:

- Regular Reflection (RR)
- Irregular Reflection (IR)

The RR is referred to as a two shock structure, the incident wave (i) and the reflected wave (r).These two shocks meet at the reflection point (R) on the wedge surface. The IR is regarded as a three shock structure which comprises of the incident wave (i), the reflected wave (r) and the Mach stem (m). These three shocks intersect at the triple point (T). A slipstream commonly referred to as a shear layer (S) emanates from this triple point and propagates towards the wedge surface. A schematic representation of regular and irregular reflections is shown in Figure 3.5. A more detailed explanation of regular and irregular reflections can be found in Ben Dor [3]. The simple two dimensional cases for the IR show that the Mach stem is in contact with the wedge surface while the reflected wave is away from the wedge surface.

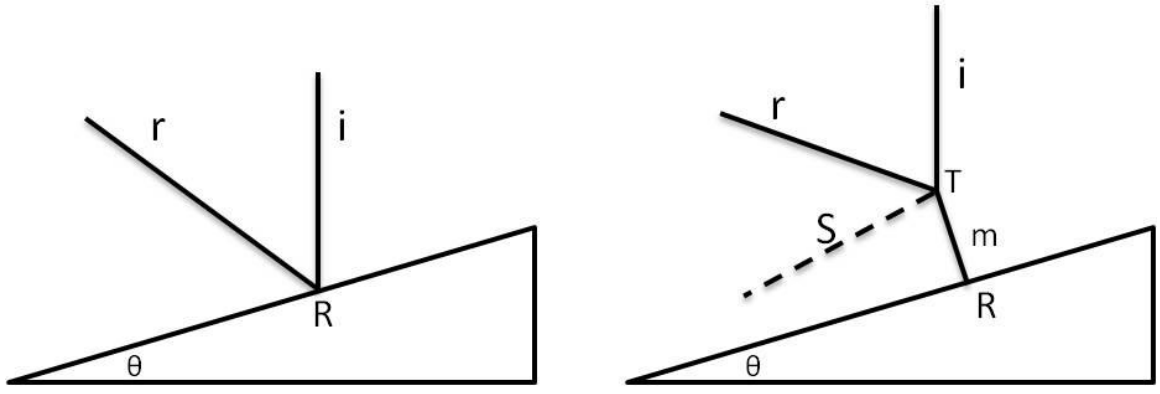

Figure 3. 5: Schematic representation of Regular (left) and Irregular (right) reflections

3.1.4 Shock Wave Boundary Layer Interaction (SWBLI)

The interaction of a shock wave with a boundary layer is a common viscous interaction problem. Interactions between shock waves and boundary layers can profoundly influence the flow over supersonic and transonic aircraft. This influence is seen in the change in the lift and drag forces, pressure distributions and resulting separation characteristics. This shock wave boundary layer interaction often results in separation or distorts the flow field which leads to a modified pressure distribution over the airfoil. This has the potential to decrease the lift force and reduce aircraft stability. These interactions can occur in engine inlets, near wing body junctures and over control surfaces. It is for this reason that the study of shock wave boundary layer interactions is an important aspect of high speed aerodynamics.

In flows without boundary layers, a shock wave would be generated or reflected by a solid surface. In such flows the pressure at the surface would increase discontinuously across the shock wave. The presence of a boundary layer does not allow this to happen, as the inner part of the boundary layer has subsonic velocities and discontinuities are not possible.

In real flows, the shock wave boundary layer interaction has a complicated structure as a result of the diverse flow regions with adjacent subsonic and supersonic regions. The viscous boundary layer is predominantly subsonic, which enables pressure disturbances to be transmitted in both upstream and downstream directions. This interaction generates large shear gradients normal to the wall.

Flow distribution in the boundary layer depends on the pressure distribution along the wall. If the pressure gradient is favorable i.e. the pressure decreases downstream, then the boundary layer remains well attached to the wall. With adverse pressure gradients, when the pressure starts to rise in the direction of the flow, the boundary layer tends to separate from the body of the surface [4].

The common interaction between a shock wave and a boundary layer is shown in Figure 3.6 [5]. This figure depicts the simplest case that describes shock wave boundary layer interaction, i.e. the interaction on a flat plate. As mentioned earlier, if the external flow is supersonic, the boundary layer velocity profile is partially subsonic. When an incident shock wave impinges on the boundary layer, a severe adverse pressure gradient is imposed on the boundary layer [5]. This may cause the boundary layer to separate. Shock wave boundary layer interaction has a major effect on the pressure and shear stress along the walls of the object being analyzed.

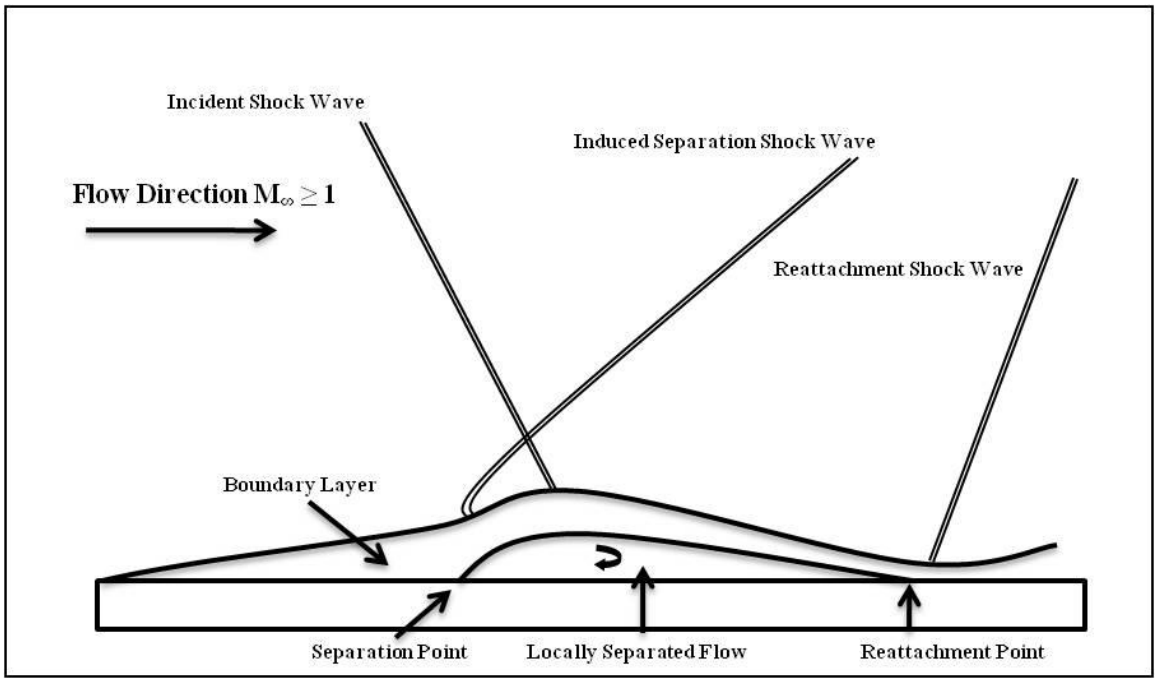

Figure 3. 6: Schematic representation of shock wave boundary layer interaction on a flat plate

The study of flow separation from the surface of a solid body has been regarded as one of the most fundamental and difficult problems to solve. Added to this problem is the determination of flow features associated with this separation. The velocity profiles for attached (V1 and V2) and separated flow (V3) are shown on a surface (although portrayed as a circular surface, this surface could also be a flat plate) in Figure 3.7 [5] (flow moving from left to right). The circular arc surface used in Figure 3.7 does not necessarily imply that reversed flow occurs on circular arc surfaces. If the flow over the

surface produces an adverse pressure gradient i.e. the pressure increases in the direction of the flow, a region of reversed flow may exist. This region of reversed flow will cause the flow to separate from the surface and as a result a large wake of recirculating flow occurs downstream of the surface [5].

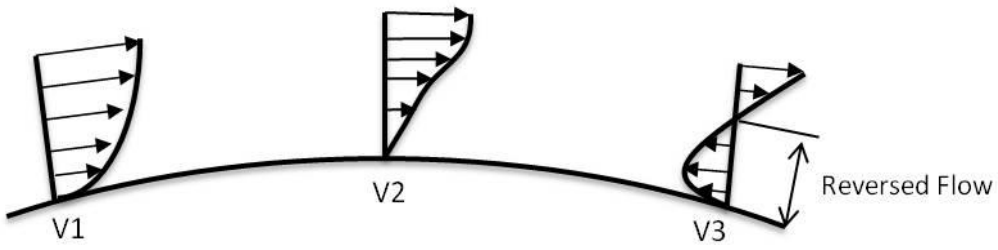

Figure 3. 7: Velocity profiles showing attached and separated flow

Separation enforces a considerable limitation on the operating characteristics of aircraft wings, helicopter blades, turbines etc. This leads to a significant degradation to their performance. Separation is normally accompanied by a reduction of the lift force, sharp increase in drag, increases in heat transfer at the reattachment region and pulsations of pressure which result in flutter and buffet onset.

3.2 Supersonic Corner Flows

3.2.1 Background

The study of supersonic flows in corner configurations is a topic that has generated a great deal of interest amongst aerodynamicists and shock wave researchers. Interest in this topic lies in both the practical and theoretical aspects of supersonic flows. Researchers have associated the corner configurations to intersections between certain aircraft components namely, wing body-fuselage intersections, several air intake configurations and in recent times the wing-wing tip/winglet configurations. Simplifying these types of intersections has enabled both the theoretical and experimental evaluation of simplified corner flow interactions.

Shock wave researchers have studied these types of corner configurations to analyze the shock structure that is formed by two intersecting aerodynamic surfaces. This analysis has led to numerous numerical and analytical investigations of steady state supersonic ***inviscid*** flows in corner configurations. The foundation of the early research revolved around the shock wave reflections and interactions. The corner configuration produces a complicated three dimensional shock wave reflection pattern.

3.2.2 Early Research

Studies have been conducted on simplified geometries which comprise of two aerodynamic surfaces (plane wedges) at a specified dihedral angle to each other, commonly referred to as the sharp corner case. In these cases two oblique bow shock waves are attached to the leading edges and interact with one another to form a three dimensional shock structure as shown in Figure 3.8. Early experimental work was done on these geometries by Charwat and Redekopp [6]. A Mach stem surface (m) develops between the two incident shocks (i) and the reflected shocks (r) propagate back to the airfoil surface. As in the case of the Mach reflection shown in Figure 3.5, a shear layer (S) develops from the shock intersection and also propagates towards the surface.

Additional research conducted by Watson and Weinstein [7] and by West and Korkegi [8] into supersonic and hypersonic corner flow interactions all showed a similar corner flow structure to that of Charwat and Redekopp. However, further experimental research conducted by Korkegi [9] showed a region of disturbed flow that extended from the corner interaction far beyond the location of the reflected shocks in a spanwise direction and Korkegi associated this with boundary layer separation.

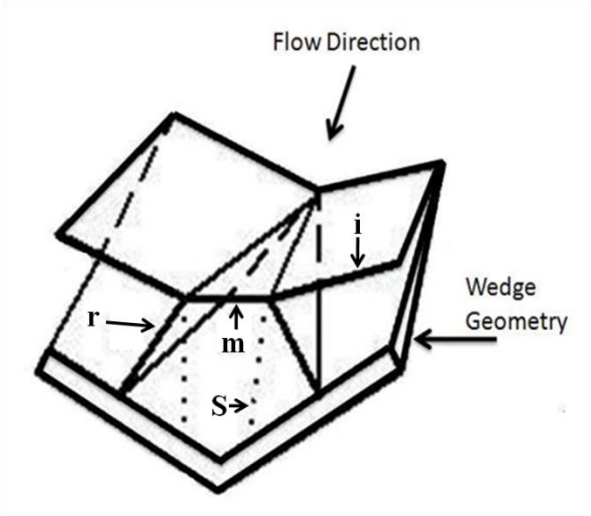

Figure 3. 8: Supersonic corner flow with Mach reflection on two plane wedges

The research that followed the early experimental work focused on the development of numerical techniques that enabled the accurate prediction of the shock structure (Mach reflection) within a supersonic sharp corner. These shock structures were detected in the numerical solutions of the Euler equations using either a second order shock capturing finite difference technique or a second order shock fitting finite difference technique. The shock capturing techniques were used by Kutler [10], Shankar *et al.* [11] while the shock fitting techniques were used by Marconi [12]. Due to the fact that the inviscid corner flows are conically self similar Kutler, Shankar *et al.* and Marconi all reduced the three dimensional problem to a two dimensional problem. Kutler and Marconi both replicated the experimental conditions used by West and Korkegi [8]. The results produced by the numerical techniques were found to be in good agreement with each other.

The early inviscid numerical research conducted on supersonic sharp corners was extensive [6-13]; however Martin [14] extended this research by including a rounded internal corner (fillet profile) between two wedge surfaces. Martin investigated, both numerically and experimentally, the supersonic flow field in a rounded internal corner. Numerically Martin developed a shock fitting scheme that differed from those utilized in previous publications as it included a rounded internal corner in the numerical setup. The geometries investigated consisted of a conical segment at the leading edge. The radius of the rounded corner increased along the length of the chord hence rendering the flow conical and self similar. Given the lack of available data on the flow field conditions for a rounded internal corner at the time, a comparison had to be made with previous data obtained for the sharp corner case. Martin's results did however show that as the radius of the rounded corner increased along the length of the chord, the pressure gradient towards the corner increased. This early research thus provided an initial insight into the flow field within a rounded internal corner.

Subsequent studies completed on supersonic corner flows which included a rounded internal corner between two wedge surfaces were done by Skews *et al.* [15]. In contrast to the study completed by Martin [14], this research focused on non-conical flows by including fillets, camber and varying the dihedral angles of the respective geometries. Both experimental and inviscid numerical investigations were considered. Unlike the work done by Martin [14], Skews *et al*. [15] used a corner with a constant radius fillet i.e. the fillet radius was constant along the length of the chord, to ensue non-conical flow. The inviscid numerical research was a fully three dimensional problem. The preliminary experimental and numerical results produced showed that the incident shock profile initially corresponds to that of the leading edge of the geometry, but as the shock moves away from the leading edge, the cross sectional shock profile becomes that of the commonly known Mach reflection (Figure 3.8).

A study on supersonic inviscid corner flows was also completed by Goonko *et al.* [16]. This research was a comprehensive numerical and analytical study of steady state supersonic inviscid flows within sharp corner geometries. The flow features that resulted from the formation of the wedge generated shocks were identified and compared to previous available data. The research focused on the transition criterion that enables the transition from regular to irregular reflection. The transition values of the wedge, sweep and dihedral angles were the foundation of the study. The analytical results showed that for corner flows with unswept wedges and a 90 degree dihedral angle between the wedge surfaces, the conditions of regular to irregular shock reflection transition correspond to either the detachment or sonic criterion [16]. The results produced also showed that the von Neumann transition is possible and achieved in corner configurations with a forward swept angle ≤ 0 and a 90 degree dihedral angle between the wedges. Goonko *et al.* [16] thus focused on transition criterion for shock reflections and the results were in good agreement with previous analytical investigations into supersonic inviscid corner flows.

The early numerical research that solved the Navier Stokes equations for three dimensional corner flows was completed by Shang *et al.* [17]. A numerical scheme that utilized the Navier Stokes equations in combination with a turbulence model was developed and this scheme was used to capture the shock structure within a supersonic sharp corner. Shang *et al.* showed that the concept of utilizing a turbulence model is not restricted to two dimensional flows but can be extended to three dimensional flows. The results from the early viscous simulations adequately predicted the shock structure within a supersonic corner and were in good agreement with the experimental data obtained.

Settles *et al*. [18] focused on experimental investigations for a SWBLI on swept compression corners. Compression leading edge angles of 16 and 24 degrees were used on all the geometries and these angles caused near incipient and separated two dimensional flows at Mach 3. The compression corners were also swept incrementally from 0 to 50 degrees. The study focused on surface flow patterns and surface pressure distributions, amongst many other aspects, similar to that being investigated in the current study. Settles and Tang [19] also conducted a study on the above mentioned compression

corners but focused on flow visualization techniques. These techniques included vapour visualization, stereoscopic schlieren, conical shadowgraph, particle tracer methods and kerosene-lampblack surface streak traces i.e. the oil film technique. The study explored the validity of using these techniques for three dimensional SWBLI.

The research into corner flow interactions has thus been extensive on plane wedges, both experimentally and computationally; more specifically the simple sharp corner case (Figure 3.8) has been the core case of study for many researchers. Skews *et al*. [15] produced inviscid computational results as well as preliminary experimental results for the rounded internal corner case but apart from this very little research has been conducted and documented on these types of geometries i.e. geometries that include a rounded corner between two aerodynamic surfaces. More specifically, the effect of the rounded corner on the formation of the Mach reflection and shear layer as well as the effect on the surface pressures is yet to be fully investigated.

Numerically, these cases have limited data available when using a ***viscous*** model. The shock wave boundary layer interaction resulting from the interaction of the reflected wave and the surface has not been investigated. More so, the transition from the original wedge geometry to a more realistic camber profile for both the sharp corner case and the rounded internal corner case has not been investigated.

Experimentally, the flow patterns on the surface of the above mentioned geometries have not been investigated. Skews *et al*. [15] performed experimental work using the laser vapour screen technique and this flow visualization method enabled the cross sections of the shock structure to be viewed. The experimental and numerical results produced are shown in Figure 3.9. The cross sectional shock profile for the sharp corner case establishes the formation of the Mach reflection for both the numerical and experimental analysis. The current study will make use of an alternate flow visualization technique to study the flow patterns on the surface of the geometries.

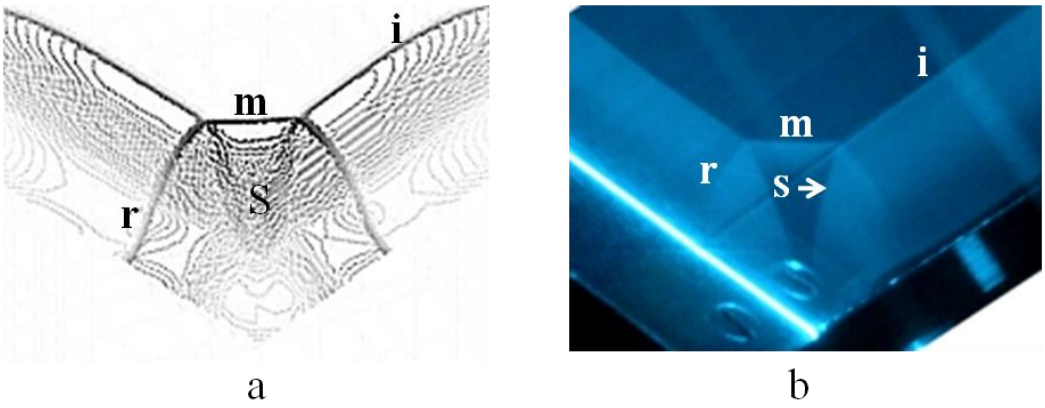

Figure 3. 9: Comparison of numerical and experimental corner flows, (a) Numerical contour plots, (b) Experimental laser vapour screen flow visualization

3.3 Transonic Corner Flows

3.3.1 Background

Supersonic corner flow interaction focuses on the shock wave interactions and reflections on geometries that may represent engine inlets, certain control surfaces or wing body-fuselage intersections. For high speed shock wave research it is thus not uncommon to isolate these components and conduct research similar to that mentioned in Section 3.2. However, most experimental and computational research conducted in the transonic flow regime (generally M 0.7 to M 1.2) is conducted on complete aircraft geometries; as a result the detailed study of transonic corner flow interactions has been minimal, with only a few authors contributing to this field. Aircraft components that resemble corner flow intersections are the common wing body-fuselage intersections and the wing-wingtip/winglet intersections. The wing-winglet intersection has different geometries associated with it. Examples of these are blended winglets, wingtip fences and the recently designed spiroids winglets. The blended winglets have a fillet profile (rounded corner) between the wing and the winglet. The wingtip fences have a sharp corner between the wing and the winglet while the spiroids winglets have both fillet and sharp corner profiles associated with it. These different winglets are shown in Figure 3.10.

3.3.2 Transonic Shock Waves

A general definition of transonic flow is flow that is associated with both subsonic and supersonic regions. Transonic shock wave analysis and the resultant shock wave boundary layer analysis thus become more complicated when compared to purely subsonic or supersonic flow. The typical progression of shock waves in transonic flow is shown in Figure 3.11. The development of the shock wave and its associated flow properties is dependant of the free stream Mach number and airfoil geometry.

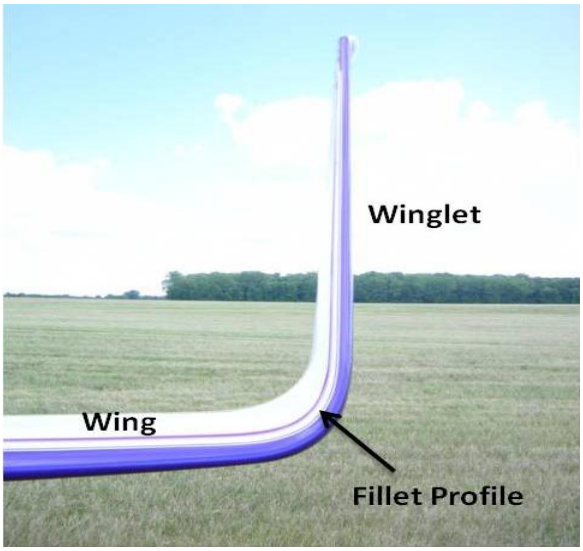

(a)

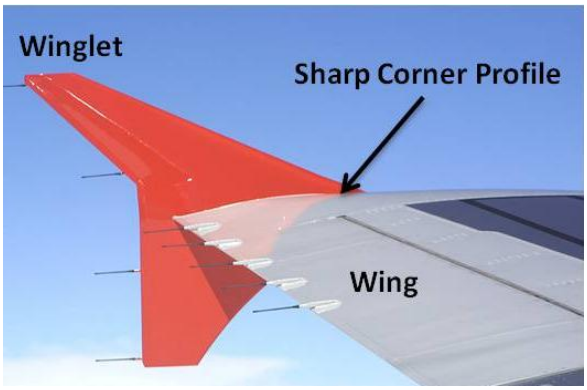

(b)



(c)

Figure 3.10: Wing-winglet intersections, (a) Blended winglet, (b) Wingtip fence, (c) Spiroids winglet

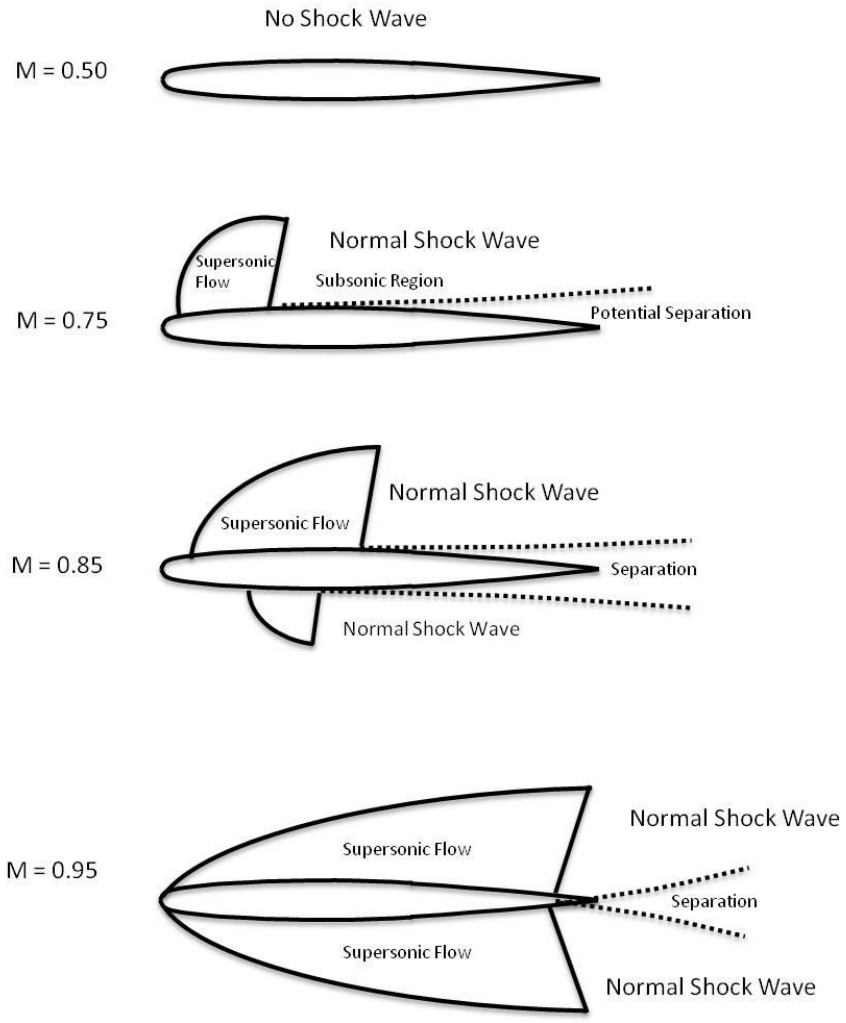

Figure 3. 11: Progression of shock waves over an airfoil in transonic flow

3.3.3 Previous Research

The study on transonic corner flows has not been investigated in great detail. In 2009, Grenon *et al* [20] completed a research investigation at ONERA, The French Aerospace Laboratory, which focused on the aerodynamic design of flying wing configurations. According to Grenon *et al*, a blended winglet is generated by moving an airfoil section along curved spanwise direction lines and it may be considered a smooth deformation of the original straight wing tip. The study focused on two aspects, the first was the optimization of a blended winglet using a plain flap control surface. This was to be used

on the VELA2 (Very Efficient Large Aircraft) blended aircraft configuration. The second was to achieve a flying wing configuration with satisfactory aerodynamic characteristics in transonic conditions. The blended wing concept in the first study is similar to that seen in Figure 3.10*a*.

The first study, which has more relevance to the current study was a numerically analysis, that was completed to determine the efficiency of the winglet to improve the lift to drag ratio, lateral stability and control. A performance evaluation was completed using Euler equations and a rough estimation of the viscous drag was done using the flat plate boundary layer theory [20]. These simulations were completed at cruise conditions (M 0.85 and angle of attack 3°). The objectives of the second study were to design viable wing geometries to account for aerodynamic cruise performances, while taking into account longitudinal trimming and geometric constraints. The results for the study showed that a significant drag reduction was obtained when using the blended wing configuration in transonic cruise and landing or take-off conditions. The inclusion of a winglet also improves lateral stability both in yaw and roll [20].

These preliminary investigations showed that winglets are an important aspect of transonic aircraft design, however both these studies focused on the aerodynamic characteristics associated with these winglets. Shock wave formations, surface pressure distributions, the SWBLI and associated separation characteristics were not studied in immense detail. The current study focuses more on these aspects and draws a comparison between blended (fillet) and sharp corner winglets. The effects of sweep are on the shock formation and pressure distributions are also studied.

3.3.4 Transonic Airfoils

The early research conducted on supersonic corner flows utilized simple wedge geometries as its camber profile to facilitate the formation of the shock structure along the chord. However for the transonic corner flow study, realistic or existing airfoils were selected. Research conducted on transonic airfoils showed that the Rae 2822 and the

Onera M6 airfoils have the most published experimental and 2D computational data available.

3.3.4.1 Rae 2822

The Rae 2822 airfoil is a supercritical airfoil that has become the standard test case for turbulence modeling validation. Extensive experimental work was also performed by Cook *et al*. [21] and this work focused on pressure distributions and boundary layer measurements. This supercritical airfoil is generally regarded as a thick airfoil. A chord length of 1 metre generates a maximum thickness of 0.122 metres. Figure 3.12 illustrates the shape of the airfoil.



Figure 3. 12: Schematic representation of the Rae 2822 airfoil

Fluent® [22] and Star CCM+® researchers have both used the Rae 2822 airfoil as their airfoil of choice to validate their respective turbulence modeling software packages. The results obtained are seen to validate the experimental work done by Cook *et al*. [21].

3.3.4.2 Onera M6

The Onera M6 airfoil is a simple symmetric airfoil. It is also a common airfoil used to validate turbulence models for external flows because of its simple geometry combined with complexities of transonic flow. Experimental work was carried out by Schmitt *et al*. [23] and this focused on pressure distributions at transonic Mach numbers. A chord length of 1 metre generates a maximum thickness of 0.0979 metres. Figure 3.13 illustrates the shape of the airfoil.



Figure 3. 13: Schematic representation of the Onera M6 airfoil

The previous research conducted on the Rae 2822 and the Onera M6 airfoils established the fact that the flow over the airfoils does in fact induce separation at high transonic Mach numbers [21, 23]. The current research includes extending the 2D research previously conducted on these airfoils by creating a three dimensional geometry that comprises of two aerodynamic surfaces joined together by a blended surface (fillet profile) and utilizes the Rae 2822 and Onera M6 airfoils as the selected camber profiles; this will closely resemble a wing-winglet configuration (Figure 3.10*a*). A contrasting case in which the fillet profile will be neglected (sharp corner) will also be analyzed and this resembles the common wing body-fuselage configurations.

Four cases of transonic flows have been considered by researchers over the past few decades and these cases will be the foundation of the current transonic investigation for both the above mentioned airfoils. Table 3.1 summarizes the cases for the investigation.

Table 3. 1: Summary of cases for the transonic investigation

Airfoil	Corner Profile	Mach No.
Rae 2822	Fillet/Sharp Corner	0.75
	Fillet/Sharp Corner	0.80
	Fillet/Sharp Corner	0.85
	Fillet/Sharp Corner	0.90
Onera M6	Fillet/Sharp Corner	0.75
	Fillet/Sharp Corner	0.80
	Fillet/Sharp Corner	0.85
	Fillet/Sharp Corner	0.90

3.4 Surface Flow Visualization

3.4.1 Oil Film Technique

Oil flow visualization has been used for decades to visualize the flow patterns near the surface of a solid body or geometry exposed to air flow. Boundary layer transition, shock wave location, regions of separation and reattachment as well as surface flow directions are a few examples of the flow characteristics that can be seen using the oil film technique.

During a typical wind tunnel test, a layer of a specific oil mixture is applied to the test specimen. Once the test specimen is subjected to the desirable Mach number, frictional forces in the air flow carry the oil with it and the remaining deposits reveals specific characteristics which are interpreted by the researcher. The patterns revealed by the oil flow visualization provide information about the flow near the surface.

The pattern revealed by the oil mixture may be analyzed during a typical wind tunnel run by taking photographs from outside the wind tunnel or in certain instances the pattern will be analyzed after the tunnel run. The oil film technique can only be of a qualitative nature. [24]

One of the major problems with oil flow visualization is whether the presence of the oil film affects the boundary conditions for the air flow near the surface of the test specimen. Analysis performed by Squire [25] showed that the direction of the oil flow is dependent on the wall shear stress of the air flow and the pressure gradient.

Squire's analysis used the following boundary conditions to determine whether the visible oil flow pattern is in agreement with the direction of the surface streamlines:

- The oil velocity is equal to the air velocity in the boundary layer at the surface of the oil;
- The viscous stresses in the oil and in the air are also equal at the oil-air surface;

- The oil is at rest on the surface of the body.

The resultant equation used for determining the direction of an oil film streamline is given by [23]:

$$\left(\frac{dx}{dz}\right)_{oil} = \frac{\left(\frac{\partial u_{air}}{\partial y}\right)_{y=0} \mu_{air} + \left(\frac{\partial p}{\partial x}\right)\left[\frac{y}{2} - h\right]}{\left(\frac{\partial w_{air}}{\partial y}\right)_{y=0} \mu_{air} + \left(\frac{\partial p}{\partial z}\right)\left[\frac{y}{2} - h\right]} \tag{3.7}$$

Where,
h is the oil film thickness (mm),
u and w are velocity components,
x and z are coordinates in the surface of the wall
y is the coordinate normal to the wall (mm)
μ_{air} is the viscosity of air
∂p is the pressure gradient

In general the pressure term is relatively small compared to the skin friction and the resulting oil film pattern is a good representation of the actual surface streamlines [25], however if the pressure term is too large i.e. near separation, then the oil flow is decelerated, the oil film thickness increases and the oil film may pile up to form a steep ramp which affects the position where the flow separates from the wall.

The creation of the oil mixture varies according to each experiment and the experimenter. Merzkirch [24] suggests the following requirements for any oil flow mixture:

- Squire assumptions regarding the oil viscosity and skin friction must remain valid;
- The oil mixture should leave a clearly defined pattern of streaks; and

- The ideal oil mixture should not begin to run until the desired speed is reached in the wind tunnel and the resultant surface pattern should not be disturbed when the air flow is stopped.

In order for the oil film technique to be effective the required oil mixture must be a precise combination of a certain carrier fluid, usually a commercially available oil and a fine pigment. This recipe is dependent of the experiment. The ratio of carrier fluid to pigment is decided by the experimenter but Settles [18] suggests a 1:4 pigment to carrier fluid ratio for supersonic flows at moderate Reynolds numbers or a ratio of 1:2 for flows with high wall shear.

The carrier fluid oils that are most frequently quoted and used are kerosene, light transformer oil, light diesel oil or vacuum pump oil. The most frequently used pigments are titanium dioxide, lamp black, fine chalk, china clay and fluorescent chrysene. The addition of oleic acid as an additive, dispersing agent is also recommended [24]. The use of oleic acid controls the size of the coagulating flocs. The coagulations are the concentrations of pigment in the oil flow; their resultant size determines the proportions and the scale of the streak pattern.

Merzkirch also suggests the following modification to the oil film technique depending on the experiment to be conducted [24]:

- As an alternative to applying a thin layer of the oil mixture on the entire surface of the object, apply distinct dots of the mixture on the object surface. As a result the streaks generated by the air flow give a better impression of the flow direction. More importantly, the distributions of the streak lengths may be used as a quantitative measure of the surface shear strength.

4. Supersonic and Transonic Geometries

The following section describes the overall supersonic and transonic geometries that are used in the experimental and computational analysis of the research investigation. The general descriptions of the geometries are discussed and are also presented with their respective images. It should be noted that geometrically much simpler or idealized cases that represent wing body-fuselage intersections or wing-wingtip/winglet intersections were analyzed. This was done so that the basic flow physics associated to these types of intersections could be obtained and understood.

4.1 Computational Transonic Geometries

4.1.1 Straight Wing with Camber and Dihedral

The transonic airfoils chosen were the Rae 2822 and the Onera M6 (Section 3.3.2). In order to accurately analyze the shock formation on these airfoils, two different profiles were selected i.e. a fillet and a sharp corner profile. These geometries have two aerodynamic surfaces joined by a fillet (blended) profile consisting of a particular radius or the two aerodynamic surfaces will be joined together without the fillet profile (sharp corner). To ensure a more realistic geometry, a chord length of 1 metre and a wing semi-span of 3.5 metres were chosen. The 3.5 metre wing semi span was chosen as this was seen as a sufficient distance away from the centre of the geometry (transonic corner) such that the tip effects that result from the edges of the wings do not affect the shock formation along the centre. The dihedral angle chosen for the analysis was 90 degrees i.e. the two aerodynamic surfaces were joined at 90 degrees to each other. This angle is seen as the most realistic angle with reference to real aircraft wing body-fuselage or wing-winglet/wingtip intersections. Table 4.1 describes the geometric parameters used to create the geometries for the investigation. Figure 4.1 illustrates these transonic geometries.

Table 4. 1: Geometric parameters for the straight wing transonic geometries

Airfoil	Dihedral Angle	Chord Length (m)	Corner Profile	Fillet Radius (m)	Wing Semi Span (m)
Rae 2822	90 ^{o}	1	Fillet	0.1	3.5
Rae 2822	90 ^{o}	1	Sharp Corner	N/A*	3.5
Onera M6	90 ^{o}	1	Fillet	0.1	3.5
Onera M6	90 ^{o}	1	Sharp Corner	N/A*	3.5

* Not Applicable as the sharp corner geometry neglects the fillet profile.

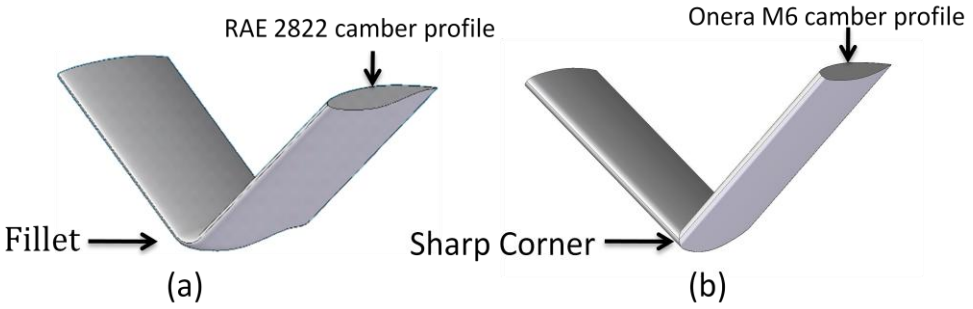

Figure 4. 1: Transonic straight wing geometries, (a) Fillet profile, (b) Sharp corner profile

4.1.2 Swept Wing with Camber and Dihedral

The effect of sweep on the shock formation was also investigated for the transonic geometries. Similar to the straight wing geometries, two profiles were analyzed i.e. a fillet and sharp corner profile. In order to maintain the 3.5 metre wing semi-span and account for the sweep angle, the root chord length had to be increased to 2 metres. The increase in chord length resulted in an increase in the fillet radius. The sweep and dihedral angles chosen were 25 and 90 degrees respectively. Table 4.2 describes the geometric parameters used to create the geometries for the investigation. Figure 4.2 illustrates these swept transonic geometries.

Table 4. 2: Geometric parameters for the swept wing transonic geometries

Airfoil	Dihedral Angle	Chord Length (m)	Corner Profile	Fillet Radius (m)	Wing Semi Span (m)	Sweep Angle
Rae 2822	90 ^{o}	2	Fillet	0.4	3.5	25°
Rae 2822	90 ^{o}	2	Sharp Corner	N/A*	3.5	25°
Onera M6	90 ^{o}	2	Fillet	0.4	3.5	25°
Onera M6	90 ^{o}	2	Sharp Corner	N/A	3.5	25°

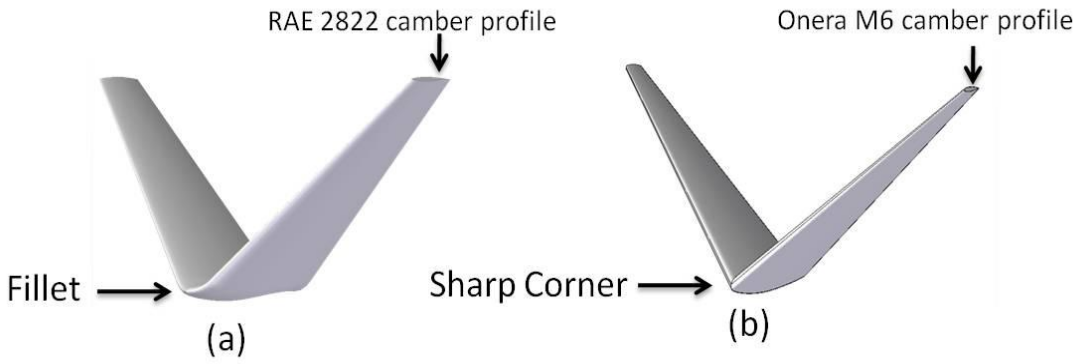

Figure 4. 2: Transonic swept wing geometries, (a) Fillet profile, (b) Sharp corner profile

It should be noted that the thickness along the centre of the sharp corner geometries are slightly higher when compared to the fillet geometries. This is a result of having the two wing sections at a 90 degree dihedral angle to each other. The maximum thickness of the all the geometries is perpendicular to the wing surface (Figure 4.3). The intersection of the two wing surfaces at 90 degrees results in the centre of the sharp corner geometries having a slightly higher thickness. The inclusion of a fillet profile enables the two wing surfaces to be joined together continuously at 90 degrees resulting in the thickness of the wing staying constant.

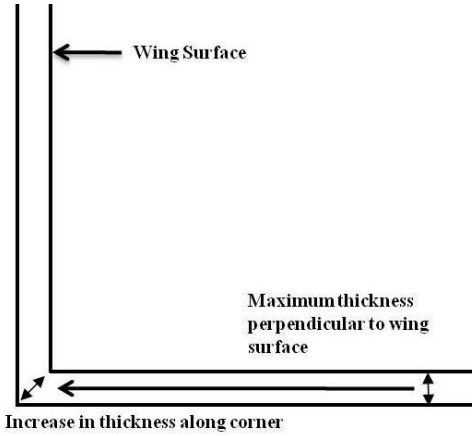

Figure 4. 3: Schematic showing variation in thickness for the sharp corner geometries

4.2 Computational Supersonic Geometries

4.2.1 Straight Wing with Camber and Dihedral

The creation of the geometries for the computational supersonic investigation took into account the experimental investigation that was performed. This was done so that a direct computational-experimental comparison could be conducted.

Two profiles were preferred for the supersonic computational analysis, a fillet and a sharp corner profile. A chord length of 0.035 metres and a wing semi-span of 0.075 metres were selected for the respective geometries. The fillet profile had a fillet radius of 0.01 metres. The dihedral angles chosen were 90, 120 and 135 degrees. The camber profile chosen was a simple circular arc (radius constant in the chordwise direction). The thickness/chord ratios varied for these cambered geometries. The maximum thickness of all the supersonic geometries occurs at 50% of the chord length. The above geometric characteristics enable a broad numerical analysis to be conducted. Table 4.3 summarizes the geometric parameters for the circular arc camber geometries and Figure 4.4 is an illustration of the supersonic geometries.

Table 4. 3: Geometric parameters for the supersonic geometries

Camber	Dihedral Angles	Chord Length (m)	Thickness/Chord ratio (%)	Corner Profile	Fillet Radius (m)	Wing semi span (m)
Circular Arc	90° 120°,135°	0.035	3,6,10	Fillet	0.01	0.075
Circular Arc	90° 120°,135°	0.035	3.10	Sharp Corner	N/A	0.075

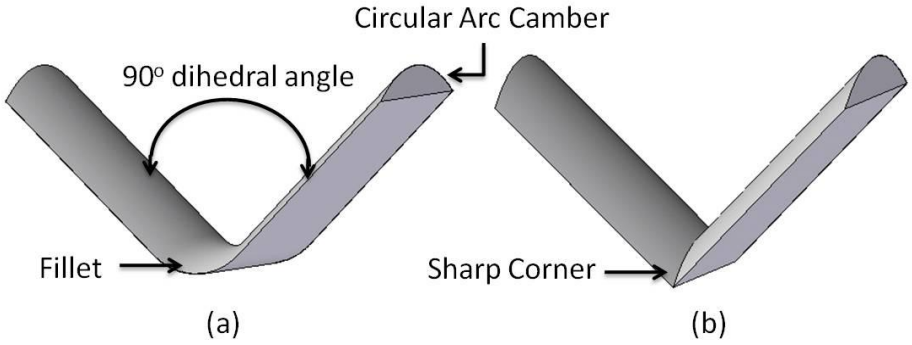

Figure 4. 4: Supersonic geometries, (a) Fillet profile, (b) Sharp Corner profile

4.2.2 Straight Wing with Varying Fillet Radii

In order to effectively analyze the effect of the fillet radius on the formation of the shock structure as well as the formation of the Mach reflection and shear layer, geometries that utilized a change in the fillet radius were created. The 90 degree dihedral angle was chosen as the standard dihedral angle for this analysis. The fillet radii were calculated as a percentage of the chord length. The radii are 20%, 30%, 40%, 50%, and 60% of the chord length. Table 4.4 summarizes the geometric parameters utilized for this part of the research. Figure 4.5 shows examples of the changing fillet radii for the geometries.

Table 4. 4: Geometric parameters for the varying fillet radii geometries

Camber Profile	Dihedral Angle	Chord Length (m)	Thickness/Chord ratio (%)	Fillet Radius %chord	Wing semi span (m)
Circular Arc	90°	0.035	10	20, 30, 40, 50, 60	0.075



Figure 4. 5: **Varying fillet radii geometries**

4.2.3 Straight Wing with Varying Camber

The camber profile chosen for the study was a circular arc camber. To effectively explore the effect of the camber on the formation of the relevant shock structures, a comparison had to be made with that of an existing geometry. The early geometries used for research into supersonic corner flows had a plane wedge profile (Section 3.2). Accordingly a numerical analysis was conducted on wedge geometries which had the same wedge angle to that seen at the leading edge of the circular arc cambered geometries (10% thickness/chord ratio geometry). The 90 degree dihedral angle was the standard dihedral angle chosen for the geometries. Table 4.5 summarizes the geometric parameters and Figure 4.6 illustrates the wedge and circular arc camber profiles with the same leading edge angles.

Table 4. 5: Wedge camber profile geometric parameters

Wedge Angle (α)	Dihedral Angle	Chord Length (m)	Corner Profile	Wing semi span (m)
22.5^{o}	90°	0.035	Sharp Corner	0.075

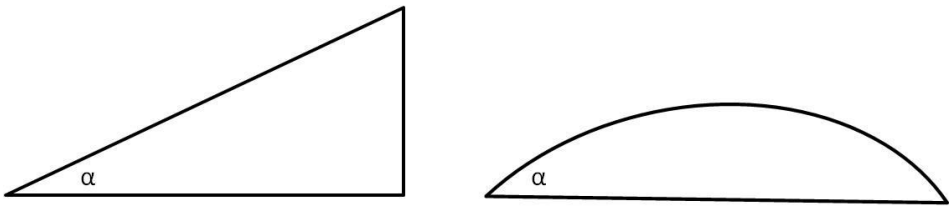

Figure 4. 6: Wedge and Circular arc geometries with the same leading edge angle

4.3 Experimental Supersonic Test Specimens

Section 4.2 describes all the computational supersonic geometries analyzed. It was not feasible and practical to manufacture all these geometries. As a result only four geometries were selected for experimental testing. The geometries chosen are shown in Table 4.6.

Table 4. 6: Classification of experimental test specimens

Camber Profile	Dihedral Angle	Corner Profile	Fillet Radius (m)	Thickness/Chord ratio (%)
Circular Arc	90°	Fillet	0.01	10
Circular Arc	120°	Fillet	0.01	10
Circular Arc	90°	Sharp Corner	N/A	10
Circular Arc	120°	Sharp Corner	N/A	10

The design of the test specimens was a complicated task to accomplish as many factors had to be taken into account such as the maximum allowable frontal area of the test pieces and the maximum allowable dimensions for the wind tunnel test section. This factor was important due to the fact that if the frontal area of the geometry was too large, the wind tunnel will choke during the experiments. The sting support also had to be blended to avoid a strong bow shock wave reflecting of it which could cause disturbances in the flow field. Figures 4.7 and 4.8 illustrate the computational drawings (created in Solid Edge V 19) and the final manufactured test pieces respectively.

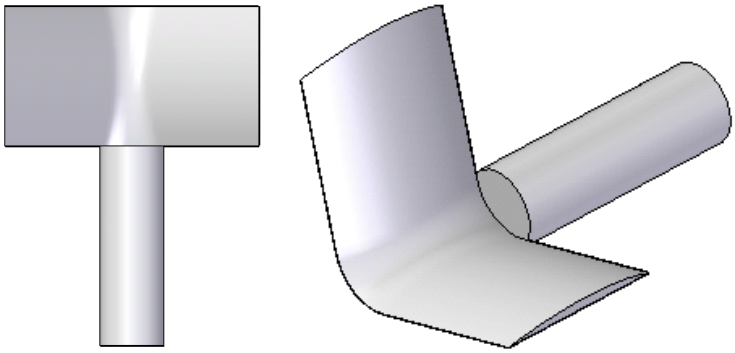

Figure 4. 7: Solid edge drawings of test specimens

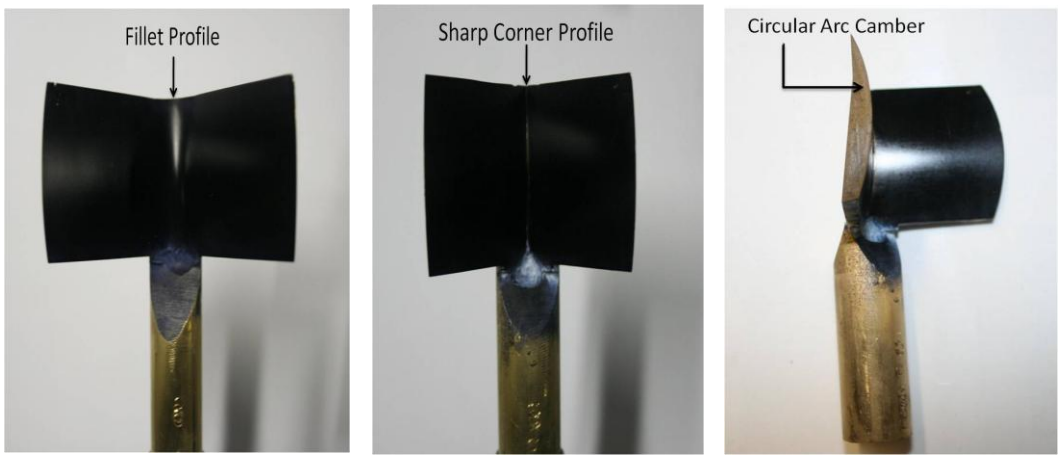

Figure 4. 8: Manufactured experimental test specimens

5. Experimentation

The following section describes the experimental facilities used to conduct the research. This section also describes the experimental setup for the surface flow visualization techniques utilized. It should be noted that experiments were only conducted for the supersonic aspect of the research as there are currently no transonic experimental facilities available at the University of the Witwatersrand.

5.1 Experimental Facilities

5.1.1 Supersonic Wind Tunnel and Components

The primary experimental apparatus employed in the research project is the supersonic wind tunnel situated in the North West Engineering Laboratory at the University of the Witwatersrand. The supersonic wind tunnel was designed and manufactured by Aerolab and is a dry-air, blow down wind tunnel. The Mach numbers obtained from the wind tunnel range from Mach 2.5 to 3.2. A schematic of the supersonic wind tunnel is shown in Figure 5.1.

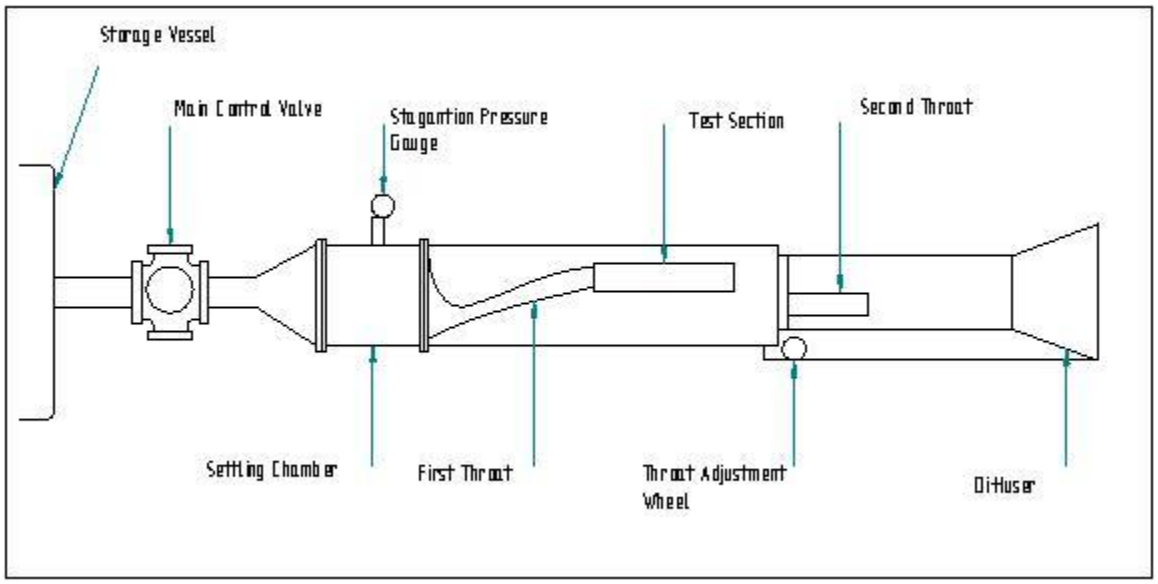

Figure 5. 1: Schematic representation of the supersonic wind tunnel and internal components

The supersonic wind tunnel has many other components associated with it. These components are necessary in order to ensure the proper operation of the wind tunnel. These components include the:

- Test Section;
- Compressor;
- Storage Vessel;
- Dryer;
- Tunnel Pressure Control;
- First and Second Throat; and
- Settling Chamber

A detailed description of all the above mentioned components together with the basic technical specifications and images can be found in Appendix A. The experimental procedure which includes the basic operation of the supersonic wind tunnel during a test and the experimental precautions can also be found in Appendix A.

5.2 Surface Flow Visualization

5.2.1 Oil Film Technique

The preferred method of surface flow visualization was the oil film technique (Section 3.4.3). The oil flow technique aids in the visualization of boundary layer transition, shock wave location as well as regions of separation and reattachment which are all significant to the investigation.

In order for the oil flow technique to be effective the required oil mixture had to be a precise mixture of a certain carrier fluid and a fine pigment. Transformer oil and titanium dioxide were the chosen as the respective carrier fluid and pigment. The oil flow mixture showed the best results by utilizing a 5:4 carrier fluid to pigment ratio while simultaneously adding a few drops of oleic acid to thin the mixture and prevent agglomeration.

The mixture was then applied on the test piece using a sponge. The use of the sponge ensured the even distribution of the mixture across the test piece and eliminated any build up of mixture around the edges and in the centre of the test specimens.

5.3 Summary of Experimental Analysis

A total of 12 experiments were completed and these are summarized in Table 5.1.

Table 5. 1: Summary of experimental analysis

Camber Profile	Dihedral Angle	Corner Profile	Fillet Radius (m)	Thickness/Chord ratio (%)	Mach No.
Circular Arc	90°	Fillet	0.01	10	2.5, 3.0 3.2
Circular Arc	120°	Fillet	0.01	10	2.5, 3.0 3.2
Circular Arc	90°	Sharp Corner	N/A	10	2.5, 3.0 3.2
Circular Arc	120°	Sharp Corner	N/A	10	2.5, 3.0 3.2

6. Numerical Simulation

Computational Fluid Dynamic (CFD) simulations were performed on the various transonic and supersonic geometries. Certain aspects of the analysis were common to both the transonic and supersonic simulations. The following section discusses the setup of the computational problem and includes all the necessary steps for the numerical analysis. The numerical investigation performed was divided into three distinct steps, namely pre-processing, processing and post processing. This was done in order to have a logical and methodical process of obtaining the most correct and precise results.

The software used for the analysis is described briefly below. All the software used for the flow simulations; mesh generations and processing are commercially available.

Gambit

The meshes that were used were generated using Gambit Version 2.4.6. Gambit supports unstructured and structured meshes. User input is accomplished through an intuitive user interface.

Fluent

The solutions obtained were computed through Fluent 12.3.26. Fluent is a general purpose, finite volume solver. Options are available for different discretization schemes, and turbulence models. Mesh adaptation is available to refine or coarsen the mesh.

Tecplot

Tecplot 360 2010 was also used to post process all the data obtained from Fluent

6.1 Pre - Processing

6.1.1 Supersonic and Transonic Geometries

Sections 4.1 and 4.2 describe the geometries for the transonic and supersonic numerical simulations respectively. The geometries were created in Solid Edge version 19 and imported as parasolids into Gambit. Sufficient spacing was provided all around the geometry in order to effectively visualize all shock formations and flow features.

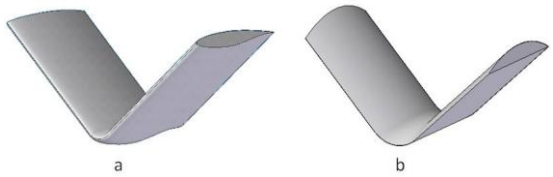

Figure 6. 1: Illustrations of (a) transonic and (b) supersonic geometries

6.1.2 Domain Boundaries

The domain boundary created consisted of the geometric surface and the surrounding boundaries. The boundaries of the domain were set at 8 chord lengths with respect to the leading and trailing edge of the airfoil and sufficient spacing was provided above and below the geometry to allow for adequate modeling of the flow field. In order to further minimize computational time, symmetry was used on all the geometries. Figure 6.2 illustrates the domain boundaries for the geometries being simulated.

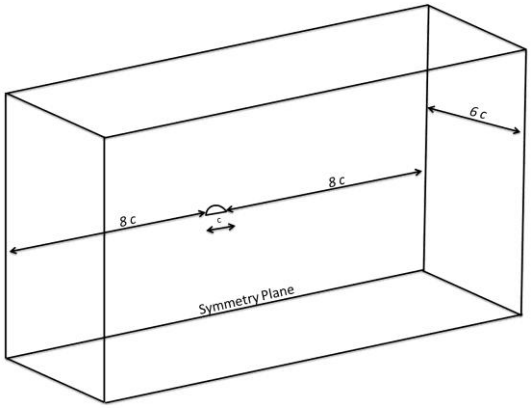

Figure 6. 2: Computational domain boundaries

6.1.3 Boundary Layer and Volume Mesh Generation

One of the main aspects of the investigation is the shock wave boundary layer interaction. The boundary layer mesh has to be adequately refined so that the data related to the flow properties within the boundary layer can be obtained for the analysis. The boundary layer and meshing tools available in Gambit were used to produce the respective meshes for both the supersonic and transonic geometries.

The mesh generation is extremely important as the results obtained can be greatly affected by the type and quality of the mesh. The curvature size function tool was used to account for the respective curvature associated with each circular arc camber and fillet profile. Each face on the geometry was meshed using this size function and the respective boundary layers were applied to these meshed faces. A final volume mesh was created using the volume mesh function and a second size function that enabled the mesh to grow from the already meshed faces to the outer volume. Table 6.1 shows the specifications used in creating the size functions and the boundary layer meshes. The volume meshes taken along the symmetry plane for both the supersonic and transonic simulations are shown in Figure 6.3.

The boundary layer mesh was monitored by plotting the surface y^+ values. The surface y^+ value plot is a method used to monitor the refinement of the mesh in the near wall layer. The y^+ value is a non-dimensional distance and is given by the following equation [21]:

$$y^+ = \frac{(u^*)(y)}{\upsilon}$$

Where:

u* is the velocity at the nearest wall

y is the distance to the nearest wall

υ is the kinematic viscosity

The y^+ value is an important parameter when dealing with cells close to walls in turbulent flows. Turbulence models and the wall laws have some restrictions between which y^+ values they are valid. In general the mesh is refined enough to produce adequate detail in the boundary layer if the y^+ value is ≤ 1 or ≥ 30. Figure 6.4 is a plot of the y^+ value taken along the centre of the geometry for the supersonic meshes. The y^+ value is approximately 35 and was maintained for both the supersonic and transonic meshes.

Table 6. 1: Size functions and boundary layer mesh specifications

Size Function 1	
Size Function Type	Curvature
Source and Attachment Faces	All fillet and sharp corner faces
Angle	18°
Growth Rate	1.1
Max size	0.05 m
Min Size	0.001 m
Boundary Layer Mesh	
Boundary layer type	Uniform
First Row Height	1 E -05 m
Growth Rate	1.05
Number of Layers	20
Total Number of Elements in BL	≥100 000 (Supersonic) ≥ 400 000 (Transonic)
Internal Continuity	Yes
Size Function 2	
Size Function Type	Meshed
Source Faces	Pre-meshed fillet and sharp corner faces
Attachments	Volume domain
Growth Rate	1.2
Max Size	0.250 m
Elements	Hexahedral/Tetrahedral
Initial Cell Count with Boundary Layer Mesh	
Supersonic	≥ 600 000 cells
Transonic	≥ 3.0 million cells

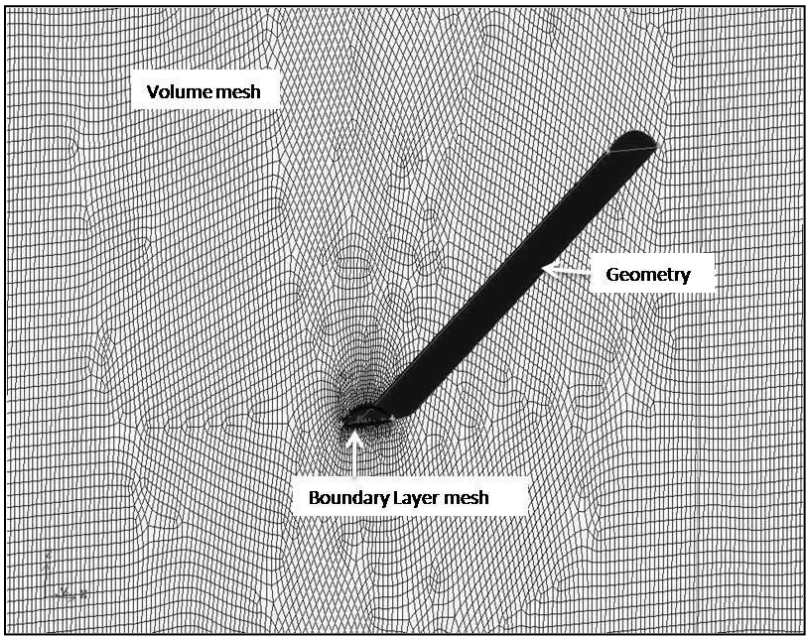

(a)

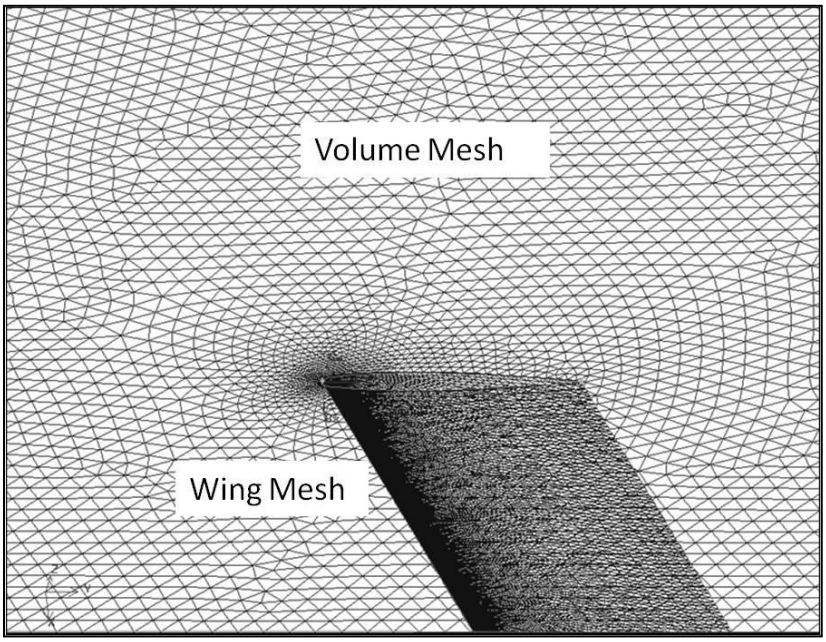

(b)

Figure 6. 3: Volume meshes taken along symmetry plane, (a) Supersonic mesh, (b) Transonic mesh

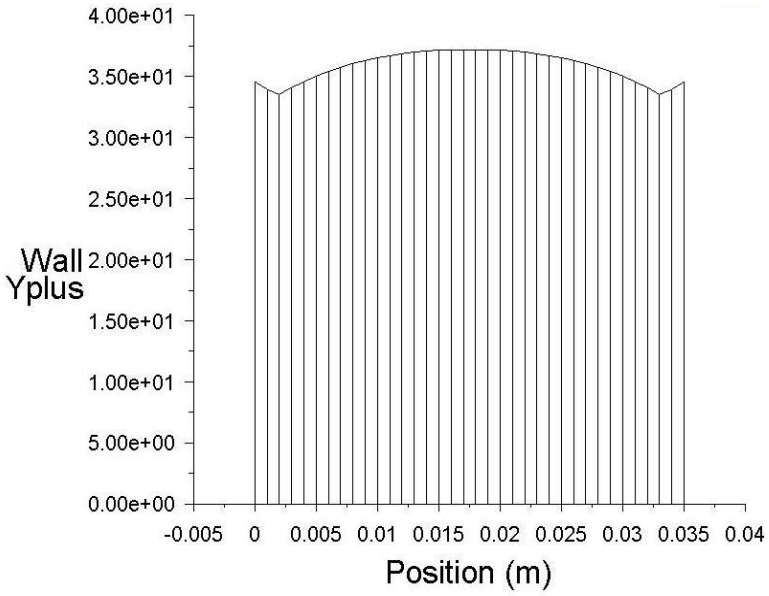

Figure 6. 4: Graph of Wall y^+ vs. position on geometry

6.2 Processing

After the meshes were completed in Gambit, it was exported as a mesh file. The mesh file was read directly into Fluent. The grid was then checked to ensure that there were no errors. The procedures described below were similar for both the supersonic and transonic analysis.

6.2.1 Solver Options and Boundary Conditions

The solver options chosen were selected so as to obtain the most accurate solution for the numerical analysis. Table 6.2 describes the basic solver options selected and Table 6.3 describes the boundary conditions utilized.

Table 6. 2: Solver options selected for the numerical analysis

Solver	Density Based
Formulation	Explicit
Space	3D
Time	Steady State
Velocity Formulation	Absolute
Density	Ideal Gas
Viscous Model	Spalart Allmaras/ κ-ε / κ –ω SST

Table 6. 3: Boundary conditions selected for the numerical analysis

Boundary Conditions	Pressure Farfield
Reference Pressure Location	Dependant on Geometry
Gauge Pressure	101 325 Pa
Temperature	300 K
Mach Number (transonic/supersonic)	0.75-0.90/2.5-5.0
Component of Flow Direction (x,y,z)	Dependant on Geometry
Courant Number	1
Discretization: Gradient	Green Gauss Cell Based
Discretization: Flow	Second Order Upwind
Discretization: Turbulent Viscosity	First Order Upwind
Initialization	Computed from Farfield
Convergence Monitors	Residuals, Drag
Convergence Criterion	0.0001

6.2.2 Convergence

The convergence criterion was the same for both the supersonic and transonic numerical analysis. As each simulation was being computed the residuals were monitored to check for convergence. The residuals are effectively the change in the flow field properties between each iteration. The convergence criterion was set at 0.0001 i.e. it is defined as being the point at which all residuals were reduced by four orders of magnitude.

Convergence was also determined by monitoring an integrated quality such as the drag coefficient. This was done for all the numerical cases that were analyzed and the solution was judged to be converged when the drag coefficient remained relatively constant over a certain time period. Figure 6.5 is the plot of the residuals and Figure 6.6 is the plot of the drag coefficient. These plots also indicate convergence and adaptation. The adaptation is indicated by the peaks on the respective plots.

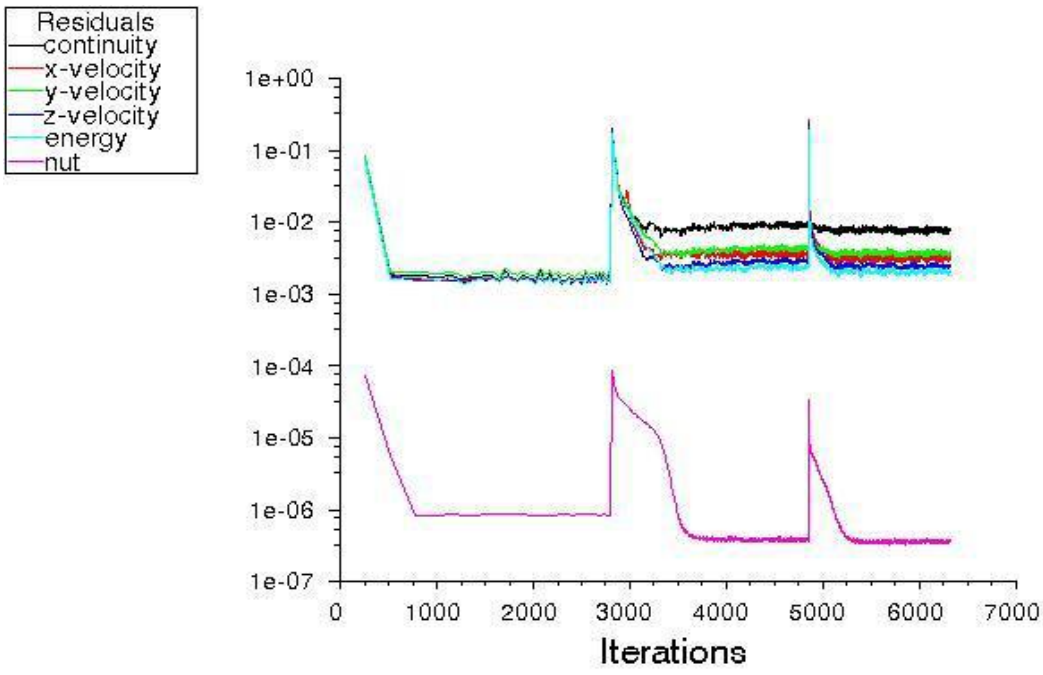

Figure 6. 5: Plot of residuals showing convergence and adaptation

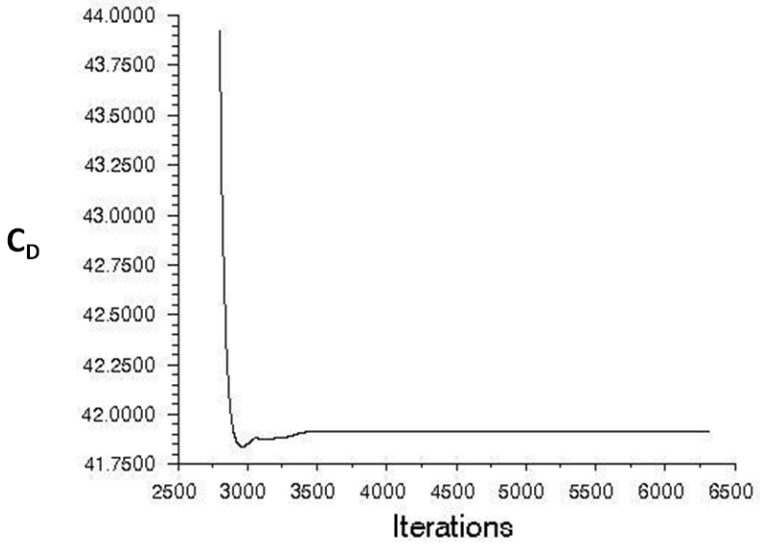

Figure 6. 6: Plot of drag coefficient showing convergence

6.2.3 Mesh Adaptation

Once the initial solution had converged, the respective meshes were adapted to obtain more accurate results. A similar mesh adaptation method was used for both the supersonic and transonic meshes. The general purpose of mesh adaptation is to reduce the solution error and since most errors occur in areas of large gradients, the meshes were adapted with respect to gradients. Mesh adaptation was performed twice on each initial mesh. The Fluent adaptation technique involves increasing the number of nodes for each cell with a gradient above a certain threshold value. Once this value was set, the iterative process was started again until convergence was reached for the second time. Thereafter the maximum levels of refinement were changed and the process was started again until a final solution was attained. Table 6.4 describes the general mesh adaptation parameters. Figures 6.7 and 6.8 show the initial and adapted meshes for the supersonic and transonic simulations respectively, once convergence was reached. The supersonic mesh images are cross sections taken perpendicular to the flow direction of the complete geometry (including symmetry) at the trailing edge. These meshes are shown for the flowfield surrounding the geometry only and not the entire domain. The transonic mesh images are taken along the symmetry plane. As shown in Figures 6.7 and 6.8, mesh refinement occurs in the regions where the shock waves are present.

Table 6. 4: Mesh adaptation parameters

Grid Adaptation Options		Refine/Coarsen
Adaptation Method		Gradients
Gradients of		Pressure, Density, Mach Number, Temperature
Normalization		Normalize
Thresholds		Refine = 0.3, Coarsen = 0.7
Maximum levels of Refinement		4
Supersonic Cell Count	**Initial Mesh**	≥ 600 000
	1st Adapted Mesh	≥ 1.2 million
	2nd Adapted Mesh	≥ 4.0 million
Transonic Cell Count	**Initial Mesh**	≥ 3.0 million
	1st Adapted Mesh	≥ 4.1 million
	2nd Adapted Mesh	≥ 5.2 million

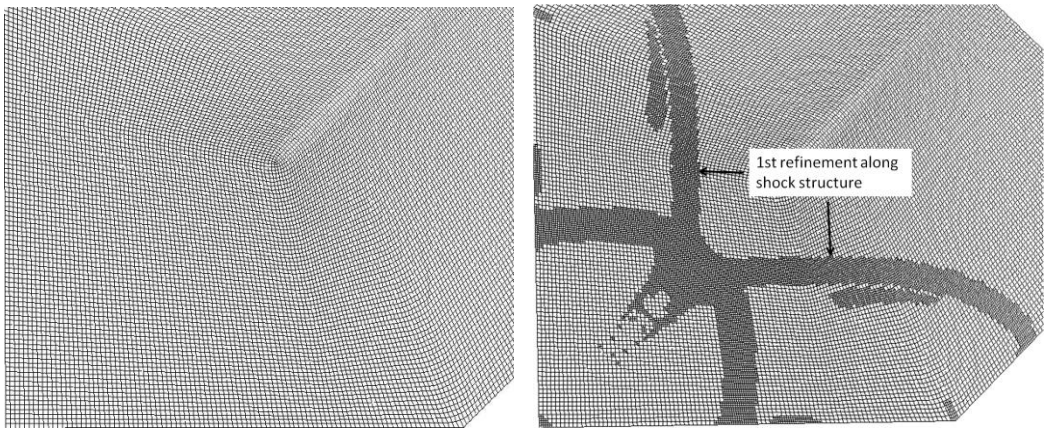

(a) (b)

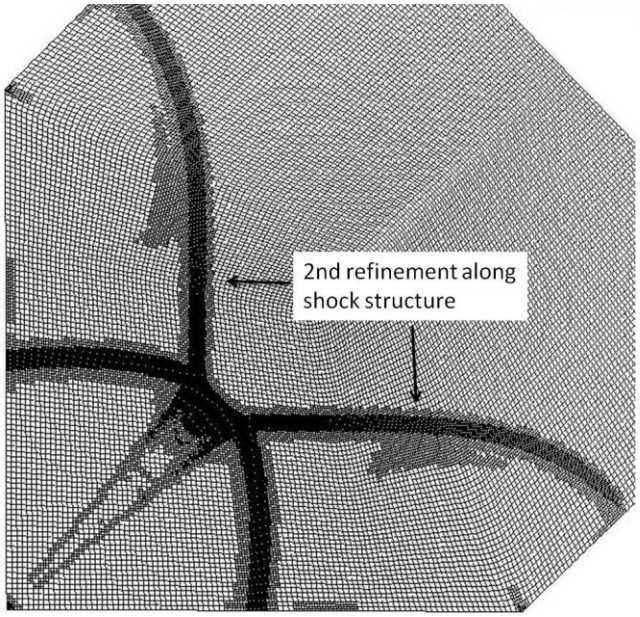

(c)

Figure 6. 7: Supersonic mesh refinement, (a) Initial Mesh (b) 1st Adapted mesh (c) 2nd Adapted mesh

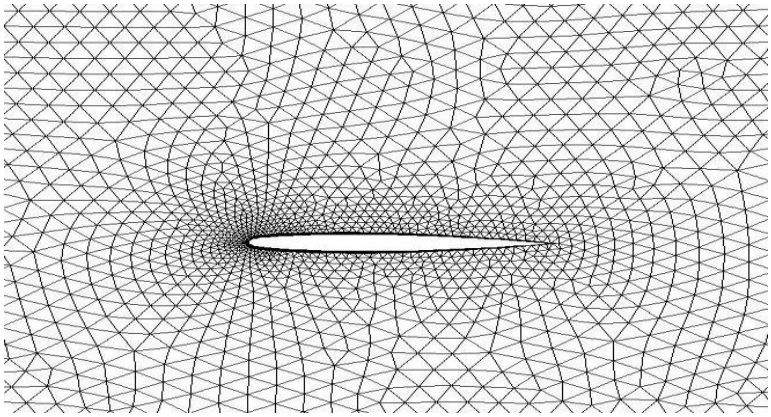

(a)

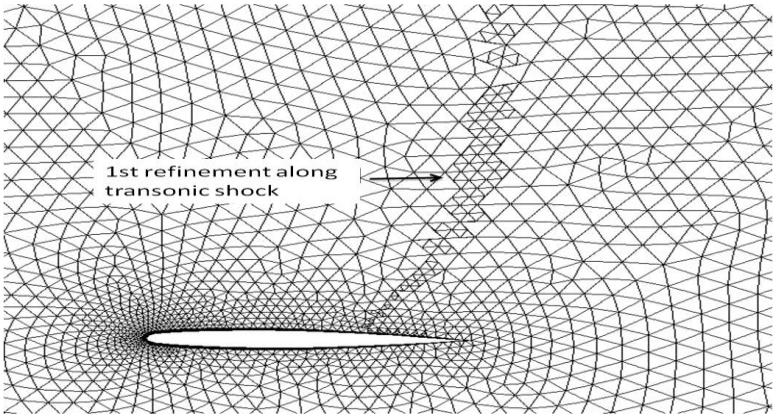

(b)

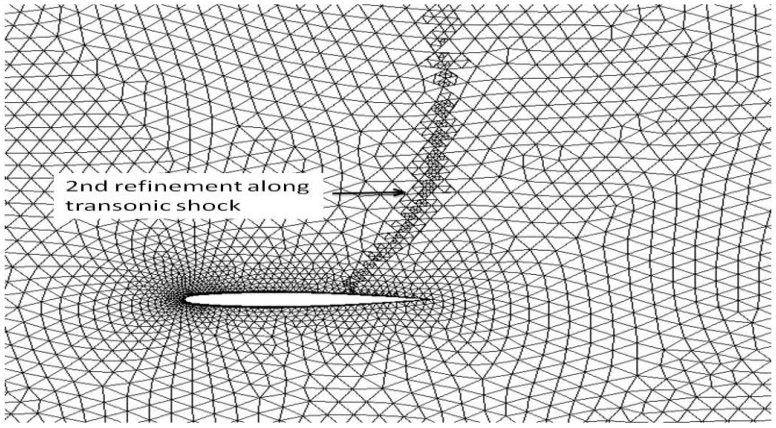

(c)

Figure 6. 8: Transonic mesh refinement, (a) Initial Mesh, (b) 1st adapted mesh, (c) 2nd Adapted mesh

6.2.4 Mesh Independence

Mesh independence tests were performed to ensure that all the results produced were independent of the type of mesh chosen for the numerical simulations. These tests were performed using the mesh refinement/adaptation technique (Section 6.2.3) as a means of checking mesh independence. These meshes were adapted once the prior solution had converged. When each mesh is adapted, it is consequently restructured and can be seen as a new mesh which results in three meshes being available for mesh independence i.e. initial/coarse mesh, first adapted/medium mesh, and the second adapted/fine mesh. Mesh independence tests were performed for both the supersonic and transonic meshes. The 90 degree dihedral angle fillet geometry was used to show mesh independence for the supersonic investigation. These simulations were conducted at Mach 3.2. The Onera M6 sharp corner straight wing geometry was used to show mesh independence for the transonic investigation. These simulations were conducted at Mach 0.9.

A comparison was made by producing line plots of the pressure, Mach number and temperature changes across the respective geometries. These values were taken at a height of 6mm above the surface and along the centre (supersonic corner) of the geometry for the supersonic investigation as it accounts for the various changes in flow properties in the regions surrounding the Mach stem and reflected wave at various stages during the formation of the shock structure. For the transonic investigation, values were taken at a height of 150mm above the surface and along the centre (transonic corner) as this accounted for the change in flow properties due to the transonic shock formation. Figures 6.9 (a-c) and 6.9 (d-f) depict the plots for these thermodynamic properties for the supersonic and transonic cases respectively.

The supersonic mesh independence tests show that the numerical results produced for the coarse, medium and fine meshes all predict the shock formation and changes in flow properties well. The flow properties are in good agreement considering the variation in cell sizes (Table 6.4) for each mesh. The finer mesh does however produce a much sharper image of the shock structure when compared to the medium and coarse meshes.

This is due to the fact that the fine mesh is refined specifically around the shock structure (Figure 6.7) and has a cell count of approximately 6 times more than that of the coarse mesh. The coarse mesh results are slightly unclear as it is calculating average flow properties over a larger cell size when compared to the fine mesh. The variation in flow properties is plotted in Figure 6.9 (a-c).

The transonic mesh independence tests show a similar trend to that of the supersonic mesh independence tests. The flow properties are predicted by each mesh and the results are in good agreement with each other. Again there is a slight discrepancy in the flow properties when comparing the coarse mesh to the medium and fine meshes. This is due to the fact that the fine mesh is refined at the point at which the transonic shock is located. Figure 6.9 (d-f) shows the results for the transonic mesh independence tests. The results obtained are in agreement for all three meshes up until the point of shock formation. This slight change in the flow properties is due to the fact that the calculations for the average flow properties occurs in a larger cell size when compared to the fine mesh, similar to that seen for the supersonic meshes.

The line plots for the supersonic and transonic mesh independence tests show that simulated numerical results produced for each mesh are in good agreement with each other. The finer meshes do however provide a much sharper image of the shock waves and the visualization of flow features is an important consideration in the analysis of supersonic and transonic shock waves. As a result of the mesh independence tests performed, the numerical results for both the supersonic and transonic investigations are mesh independent.

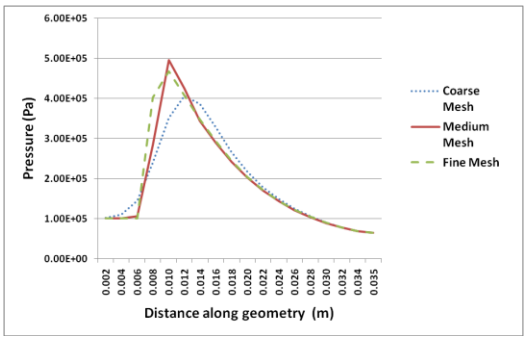

(a) Pressure: Circular Arc Fillet Profile

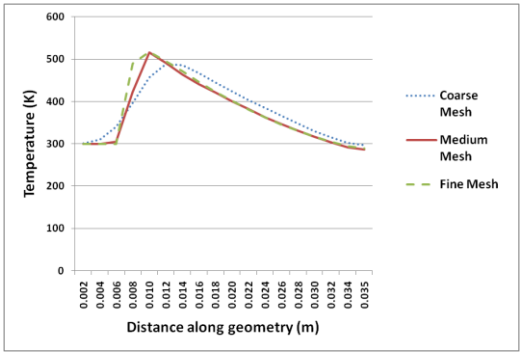

(b) Temperature: Circular Arc Fillet Profile

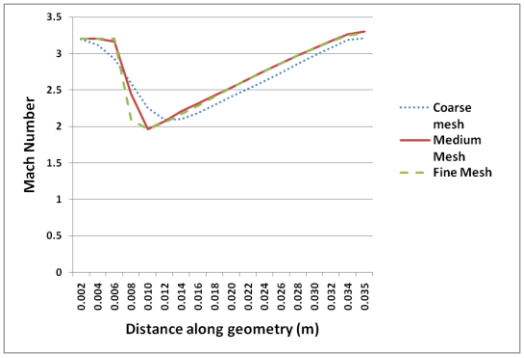

(c) Mach number: Circular Arc Fillet Profile

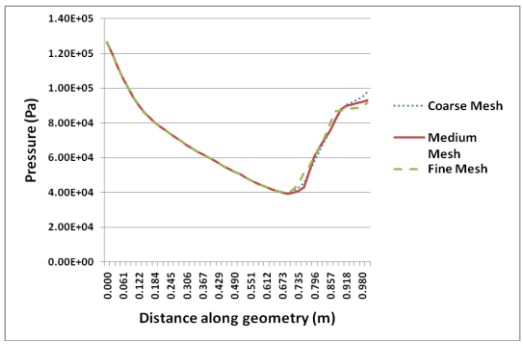

(d) Pressure: Onera Sharp Corner Profile

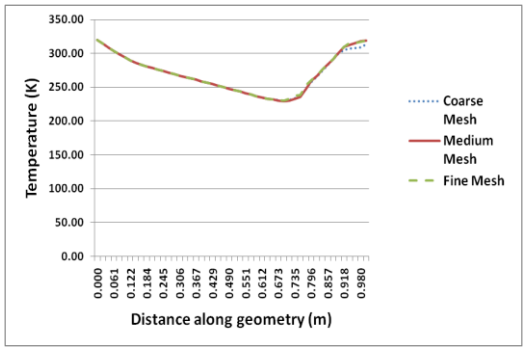

(e) Temperature: Onera Sharp Corner Profile

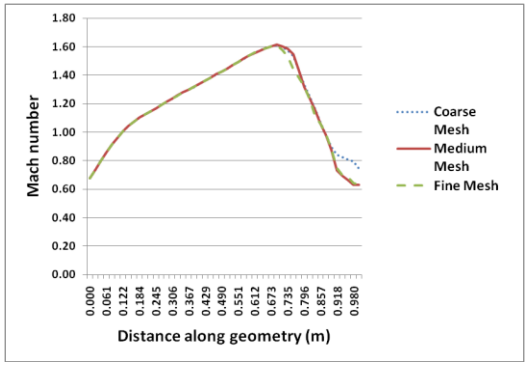

(f) Mach number: Onera Sharp Corner Profile

Figure 6. 9: Graphs of Pressure, Temperature and Mach number showing mesh independence for the 90° circular arc fillet (a-c) at M 3.2 and Onera M6 sharp corner (d-f) geometries at Mach 0.9

6.2.5 Turbulence Modeling

Early numerical research conducted on supersonic corner flow interactions utilized an inviscid solver. The current study involved the comparison of three different viscous models which included the Spalart Allmaras (S-A), k-epsilon (κ-ε) and the k- omega SST (κ-ω SST) variant available in Fluent. These models are well understood and established in literature. Fluent also conducted a validation study to validate which turbulence model was best suited to predict the flow characteristics over airfoils [22]. The Rae 2822 airfoil was selected as the airfoil of choice for the validation study. These results showed that the Spalart Allmaras turbulence model is the most effective turbulence model to use when predicting shock wave location and separation characteristics on transonic airfoils [22]. The choice of the turbulence model was based on its capability to accurately predict the shock structures within the flow field while also being computationally feasible for its use. The study conducted by Fluent was also taken into consideration in deciding the turbulence model to be used for the study of supersonic and transonic corner flows.

For the current study the 90 degree dihedral angle fillet and sharp corner supersonic geometries were used to validate the different turbulence models for the supersonic investigation. These simulations were conducted at Mach 3.0. The comparison of the turbulence models is obtained by comparing line plots of pressure, temperature and Mach number changes along the length of the geometries for each turbulence model. These values were taken at a height of 6mm above the surface of the geometry for the supersonic investigation as it accounts for the various changes in flow properties in the regions surrounding the Mach stem and reflected wave at various stages during the formation of the shock structure. Figure 6.10 shows the comparisons for these properties for the supersonic geometries.

The supersonic results show that the κ-ε, κ-ω SST and the Spalart Allmaras turbulence models predict similar changes in the flow properties. The three turbulence models also predict the formation of the shock structure i.e. Mach reflection, very well. The κ-ε and κ-ω SST turbulence models do however predict a slightly higher Mach number to that seen

by the Spalart Allmaras turbulence model for the sharp corner profile however the results for the fillet profile show that all three turbulence models predict similar changes in the flow properties.

The study conducted on the Rae 2822 airfoil by Fluent showed that the Spalart Allmaras turbulence model was the most effective turbulence model to use when considering shock waves over airfoils for transonic Mach numbers. As a result the Spalart Allmaras turbulence model was used for all the numerical simulations, for both the supersonic and transonic investigations.

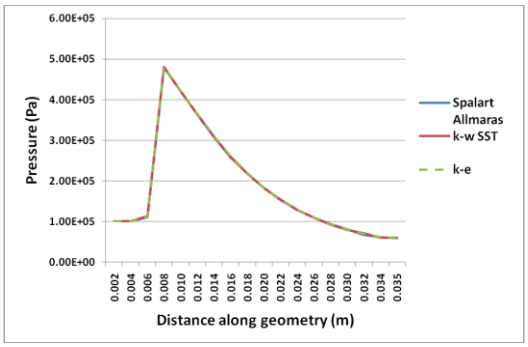

(a) Pressure: Fillet Profile

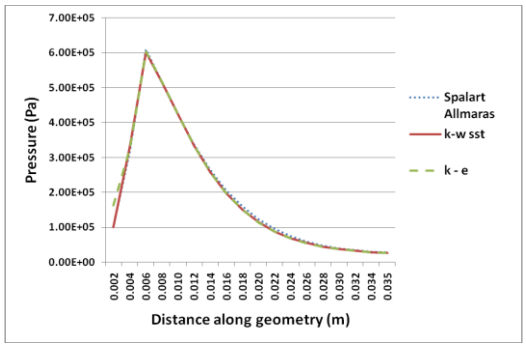

(d) Pressure: Sharp Corner Profile

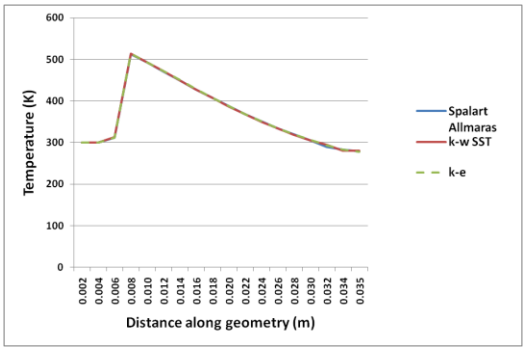

(b) Temperature: Fillet Profile

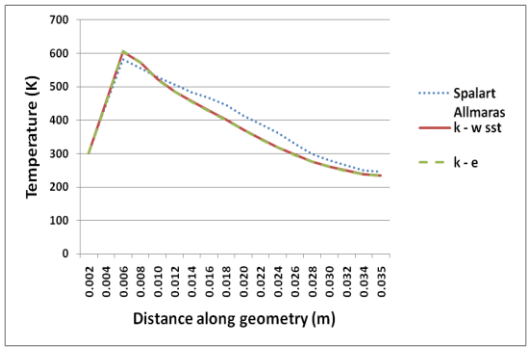

(e) Temperature: Sharp Corner Profile

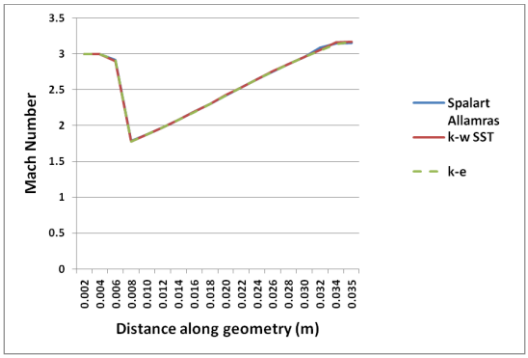

(c) Mach number: Fillet Profile

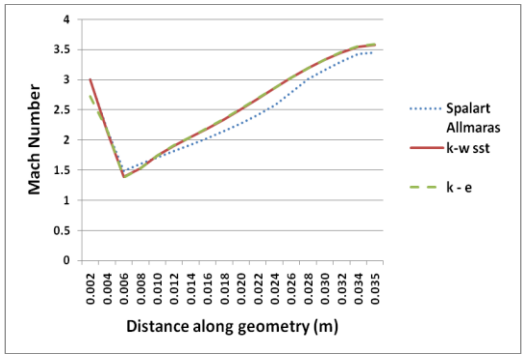

(f) Mach number: Sharp Corner Profile

Figure 6. 10: Graphs of Pressure, Temperature and Mach number for different turbulence models for the 90° fillet and sharp corner geometries at Mach 3.0

6.3 Summary of Numerical Analysis

The following sections summarize all the numerical simulations conducted. A total of 48 supersonic and 32 transonic simulations were completed. All these simulations enabled a broad spectrum of geometries to be analyzed; hence a greater understanding of supersonic and transonic corner flow interaction was obtained.

6.3.1 Supersonic Analysis

Table 6. 5: Summary of turbulence modeling study

Turbulence Modeling							
Camber Profile	**Corner Profile**	**Turbulence Model**			**Mach No.**	**T/C Ratio (%)**	**Dihedral Angle**
Circular Arc	Sharp	k-w	k-e	S-A	3.0	10.0	90 ^{o}
Circular Arc	Fillet	k-w	k-e	S-A	3.0	10.0	90 ^{o}

Table 6. 6: Summary of Mach number variation study

Mach Number Change								
Camber Profile	**Corner Profile**	**Mach No.**			**T/C Ratio (%)**	**Dihedral Angle**	**Leading Edge Angle**	**Turbulence Model**
Circular Arc	Sharp	2.5	3.0	5.0	10.0	90 ^{o}	22.5^{o}	Spalart Allmaras
Circular Arc	Sharp	2.5	3.0	5.0	10.0	90 ^{o}	22.5^{o}	Inviscid
Wedge	Sharp	2.5	3.0	5.0	N/A	90 ^{o}	22.5^{o}	Spalart Allmaras
Wedge	Sharp	2.5	3.0	5.0	N/A	90 ^{o}	22.5^{o}	Inviscid

Table 6. 7: Summary of geometric parameters study

Geometric Parameters					
Corner Profile	**Camber Profile**	**Dihedral Angle**	**T/C Ratio (%)**	**Mach No.**	**Turbulence Model**
Sharp	Circular Arc	90 ^{o}	3.0	3.0	Spalart Allmaras
Sharp	Circular Arc	120 ^{o}	3.0	3.0	Spalart Allmaras
Sharp	Circular Arc	135 ^{o}	3.0	3.0	Spalart Allmaras
Sharp	Circular Arc	90 ^{o}	10.0	3.0	Spalart Allmaras
Sharp	Circular Arc	120 ^{o}	10.0	3.0	Spalart Allmaras
Sharp	Circular Arc	135 ^{o}	10.0	3.0	Spalart Allmaras
Fillet	Circular Arc	90 ^{o}	3.0	3.0	Spalart Allmaras
Fillet	Circular Arc	120 ^{o}	3.0	3.0	Spalart Allmaras
Fillet	Circular Arc	135 ^{o}	3.0	3.0	Spalart Allmaras
Fillet	Circular Arc	90 ^{o}	6.0	3.0	Spalart Allmaras
Fillet	Circular Arc	120 ^{o}	6.0	3.0	Spalart Allmaras
Fillet	Circular Arc	135 ^{o}	6.0	3.0	Spalart Allmaras
Fillet	Circular Arc	90 ^{o}	10.0	3.0	Spalart Allmaras
Fillet	Circular Arc	120 ^{o}	10.0	3.0	Spalart Allmaras
Fillet	Circular Arc	135 ^{o}	10.0	3.0	Spalart Allmaras

Table 6. 8: Summary of fillet radius change study

Fillet Radius Change						
Fillet Radii (% Chord)	**Mach No.**			**T/C Ratio (%)**	**Dihedral Angle**	**Turbulence Model**
20	2.5	3.0	5.0	10.0	90 ^{o}	Spalart Allmaras
30	2.5	3.0	5.0	10.0	90 ^{o}	Spalart Allmaras
40	2.5	3.0	5.0	10.0	90 ^{o}	Spalart Allmaras
50	2.5	3.0	5.0	10.0	90 ^{o}	Spalart Allmaras
60	2.5	3.0	5.0	10.0	90 ^{o}	Spalart Allmaras

6.3.2 Transonic Analysis

Table 6. 9: Summary of straight wing geometries

Airfoil	Corner Profile	Chord (m)	Mach No./Reynolds No.				Angle of Attack	Dihedral Angle
Onera M6	Sharp	1	0.75 / 17.8E06	0.8 / 19E06	0.85 / 20.2E06	0.9 / 21.4E06	2.8^o	90°
Onera M6	Fillet	1	0.75 / 17.8E06	0.8 / 19E06	0.85 / 20.2E06	0.9 / 21.4E06	2.8^o	90°
RAE 2822	Sharp	1	0.75 / 17.8E06	0.8 / 19E06	0.85 / 20.2E06	0.9 / 21.4E06	2.8^o	90°
RAE 2822	Fillet	1	0.75 / 17.8E06	0.8 / 19E06	0.85 / 20.2E06	0.9 / 21.4E06	2.8^o	90°

Table 6. 10: Summary of swept wing geometries

Airfoil	Corner Profile	Chord (m)	Mach No./Reynolds No.				Angle of Attack	Dihedral Angle	Sweep Angle
Onera M6	Sharp	2	0.75 / 35.7 E 06	0.8 / 38.1 E 06	0.85 / 40.4 E 06	0.9 / 42.8 E 06	2.8^o	90°	25°
Onera M6	Fillet	2	0.75 / 35.7 E 06	0.8 / 38.1 E 06	0.85 / 40.4 E 06	0.9 / 42.8 E 06	2.8^o	90°	25°
RAE 2822	Sharp	2	0.75 / 35.7 E 06	0.8 / 38.1 E 06	0.85 / 40.4 E 06	0.9 / 42.8 E 06	2.8^o	90°	25°
RAE 2822	Fillet	2	0.75 / 35.7 E 06	0.8 / 38.1 E 06	0.85 / 40.4 E 06	0.9 / 42.8 E 06	2.8^o	90°	25°

7. Supersonic Numerical Results and Discussions

Shock wave reflections and interactions can have a profound effect on the flow within a supersonic corner. Minimizing the impact of these reflections which produce varying pressure and temperature changes on supersonic vehicles is seen as a primary objective in the design phase of supersonic vehicles. The results presented are an insight into the flow field within a supersonic corner and illustrates how the various geometric characteristics of a simplified supersonic corner impacts the flow field.

The following section presents the supersonic numerical results obtained during the research undertaken. Numerical simulations were conducted on geometries that varied in dihedral angles, thickness/chord ratios, corner profiles i.e. fillet or sharp corner and Mach numbers. All these characteristics enabled a variety of geometries to be analyzed, hence a complete range of results were produced and more data was available for the analysis on supersonic viscous corner flow interactions.

A review of Section 6.3 will confirm that a total of 48 supersonic simulations were completed. Due to the large number of geometries that were simulated, only the results for selected geometries are presented in each section. The following sets of results along with the respective discussions are presented:

- Cross sectional contour plots showing the general formation and development of the shock structures within a supersonic corner;
- Iso surfaces showing the formation and development of the shock structures within a supersonic corner;
- Contour plots of Pressure, Mach number and Shear stress;
- Influence of varying dihedral angles and thickness/chord ratios on the shock formation;
- Influence of varying fillet radii and Mach numbers on the shock formation;
- Influence of varying camber profiles on the shock formation;

- Shock wave boundary layer interaction; and
- Turbulence Modeling: Viscous vs. Inviscid

For each of the above sections, the detailed discussions are first presented and are followed by the related images and graphs. The results presented in certain sections make reference to two directions, a chordwise direction and a spanwise direction. These directions are shown in Figure 7.1.



Figure 7. 1: Illustration of chordwise and spanwise directions

**A copy of this thesis (in pdf format) is available in the electronic appendix. This copy may be referred to if any of the images presented in the following sections remain unclear after printing.*

7.1 General formation and development of the shock structure within a supersonic corner

The presence or absence of the fillet profile together with the combined effect of the camber profile, dihedral angle and thickness/chord ratio all play a significant role in the development of the shock structure across the respective supersonic geometries.

The results to be discussed in the current section are chosen from Table 6.7. These results include the 90 degree dihedral angle fillet and sharp corner geometries, both of which had a 10 percent thickness/chord ratio. This was done to distinguish the effect of including a fillet profile between two aerodynamic surfaces rather than a sharp corner profile. The third set of results to be discussed is the 135 degree dihedral angle geometry with a 3 percent thickness/chord ratio. The results are shown for this geometry as it has the largest dihedral angle and the smallest thickness/chord ratio. These three geometries enable the flow field and shock structures within a simplified supersonic corner to be analyzed in terms of varying dihedral angles and thickness/chord ratios. These simulations were conducted at Mach 3.0. It should be noted that the term transition used in this section and all further sections refers to the transition of a smooth curved oblique incident shock wave to a wave with discontinuities in slope and not the transition from regular reflection to irregular reflection as mentioned in Section 3.2.

The formation of the shock structure in a simplified supersonic corner is described in Section 3.2. These shock structures are presented in the form of line contour plots of Mach number and are further validated by numerical schlieren images. The numerical schlieren images are plotted by calculating the first derivative of density resulting in these images showing regions of high density gradients. The contour plots and numerical schlieren images are cross sectional views taken perpendicular to the flow direction (in the chordwise direction) at four distinct points, namely at 10, 20, 30 and 35mm from the leading edge. The contour plots are used specifically to track the changes in the shock structure along the chord of the geometry and not the changes in Mach number. The

incident wave (I), reflected wave (R), Mach Stem (M) and Shear layer (S) are shown on each figure.

Figure 7.2 shows the shock structure for the 90 degree fillet geometry. The oblique incident shock wave is initially a smooth curved wave. The incident shock wave corresponds in shape to that of the leading edge of the geometry but as transition occurs it becomes a wave with discontinuities in slope i.e. the formation of the Mach reflection is evident. As a result, it is established that the existence of a fillet profile delays the formation of the Mach reflection as well as the shear layer.

Neglecting the effect of the fillet profile (sharp corner) shows a distinct change in the formation of the shock structure and the Mach reflection as can be seen in Figure 7.3. The results indicate that the Mach reflection and shear layer formation starts at the leading edge of the geometry. More importantly, the shear layer initially propagates onto the surface. As the shock structure evolves, the shear layer grows with the Mach reflection but gradually pulls away from the surface. This initial propagation of the shear layer onto the surface leads to an increase in pressure and shear stress at the leading edge of the geometry.

Figure 7.4 shows the development of the shock structure for the 135 degree dihedral angle geometry which includes a fillet profile and a 3 percent thickness/chord ratio. By increasing the dihedral angle while simultaneously decreasing the thickness/chord ratio the oblique shock wave that forms remains a continuous smooth curved wave all along the geometry i.e. the incident shock wave corresponds in shape to the leading edge of the geometry and remains this way across the chord of the geometry. As a result the formation of the Mach reflection is not seen. The delay in the formation of the Mach reflection is established for all the geometries that included a fillet profile between two aerodynamic surfaces. The incident shock wave corresponds in shape to the leading edge of the geometry for all the geometries that included a fillet profile irrespective of the thickness\chord ratios or dihedral angles utilized. The Mach reflection is seen to form at the leading edge for all the sharp corner geometries.

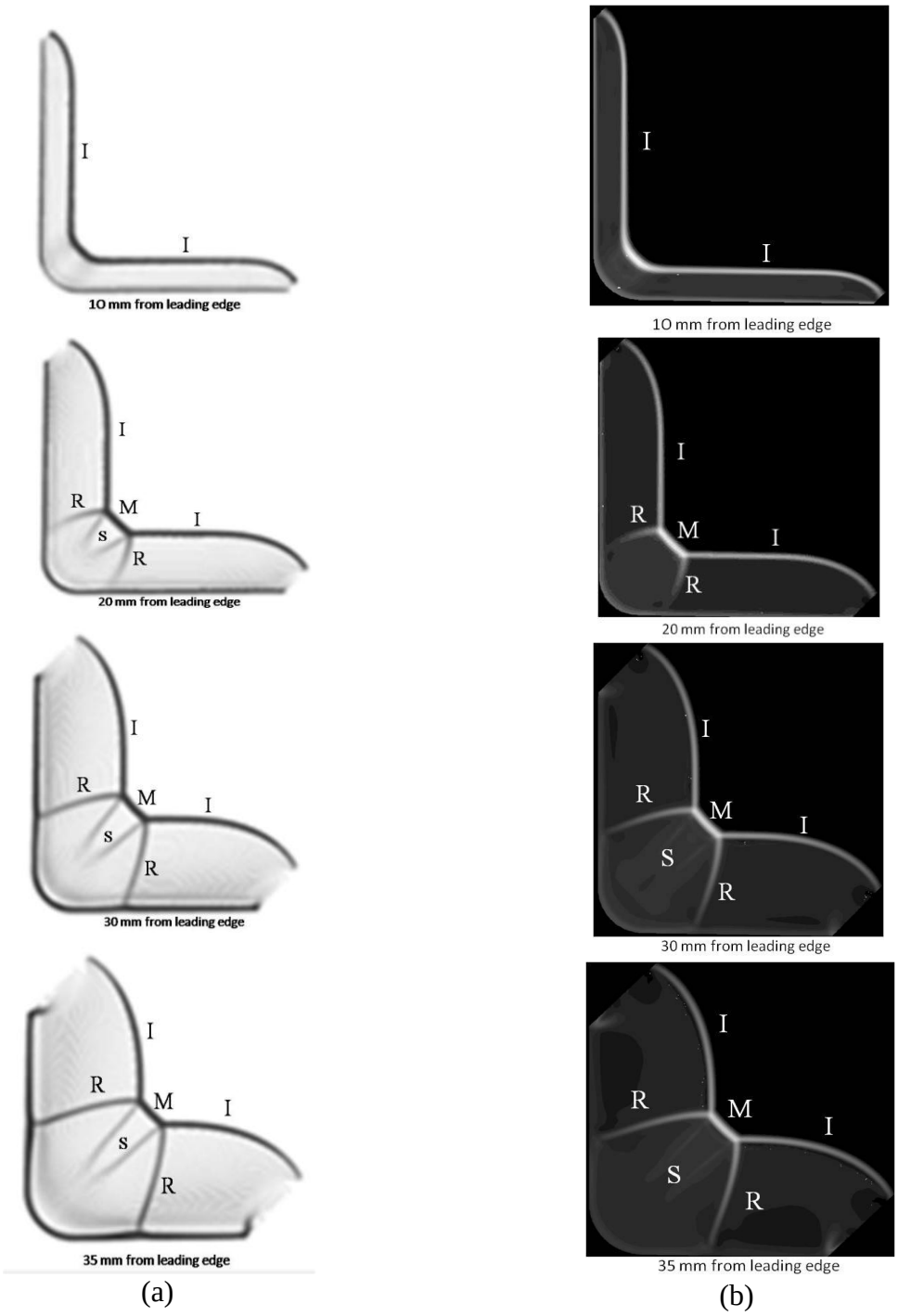

Figure 7. 2: Shock structure cross sections for the 90° fillet geometry, (a) Mach number line contour plots, (b) Numerical schlieren

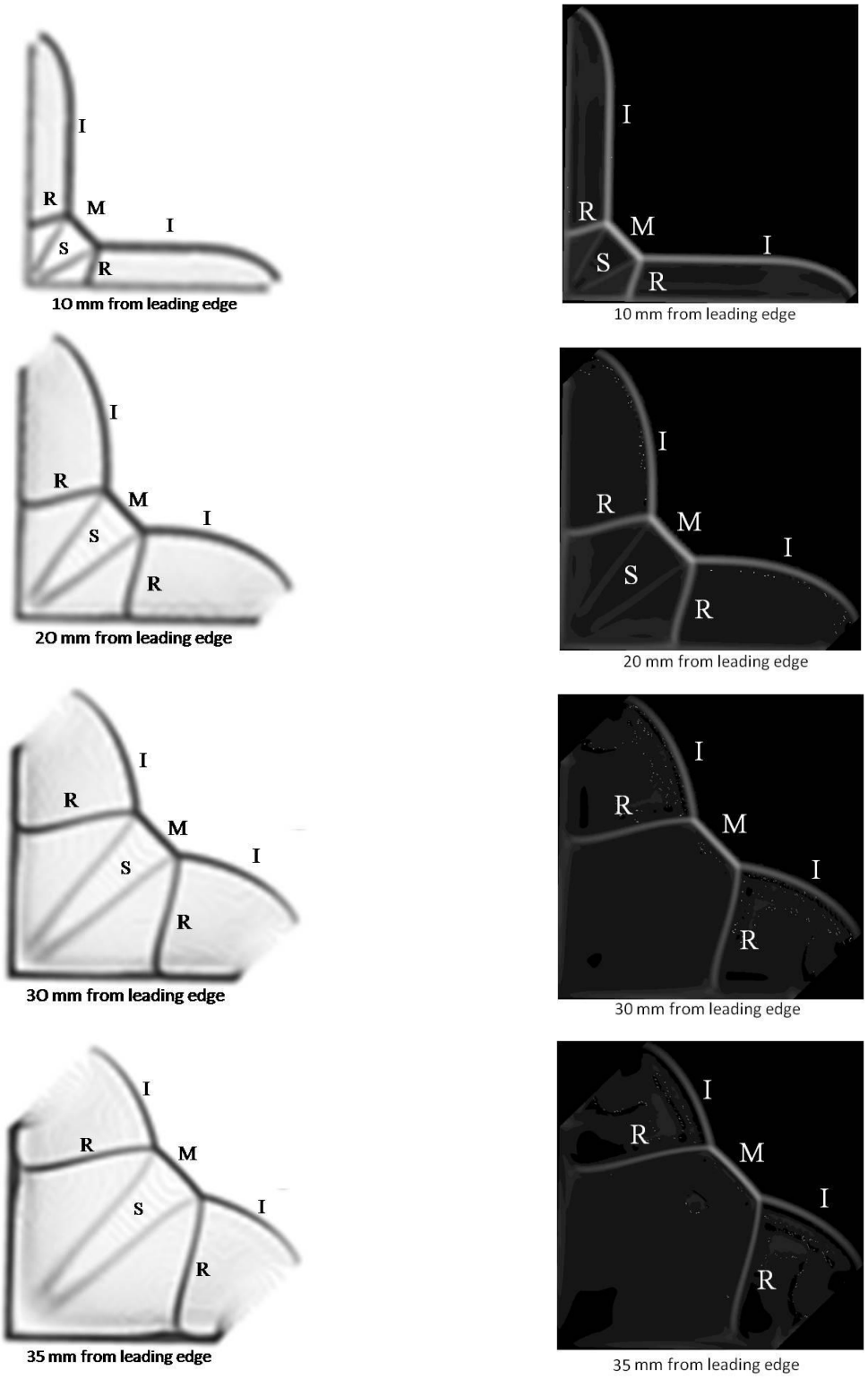

Figure 7. 3: Shock structure cross sections for the 90° sharp corner geometry, (a) Mach number line contour plots, (b) Numerical schlieren

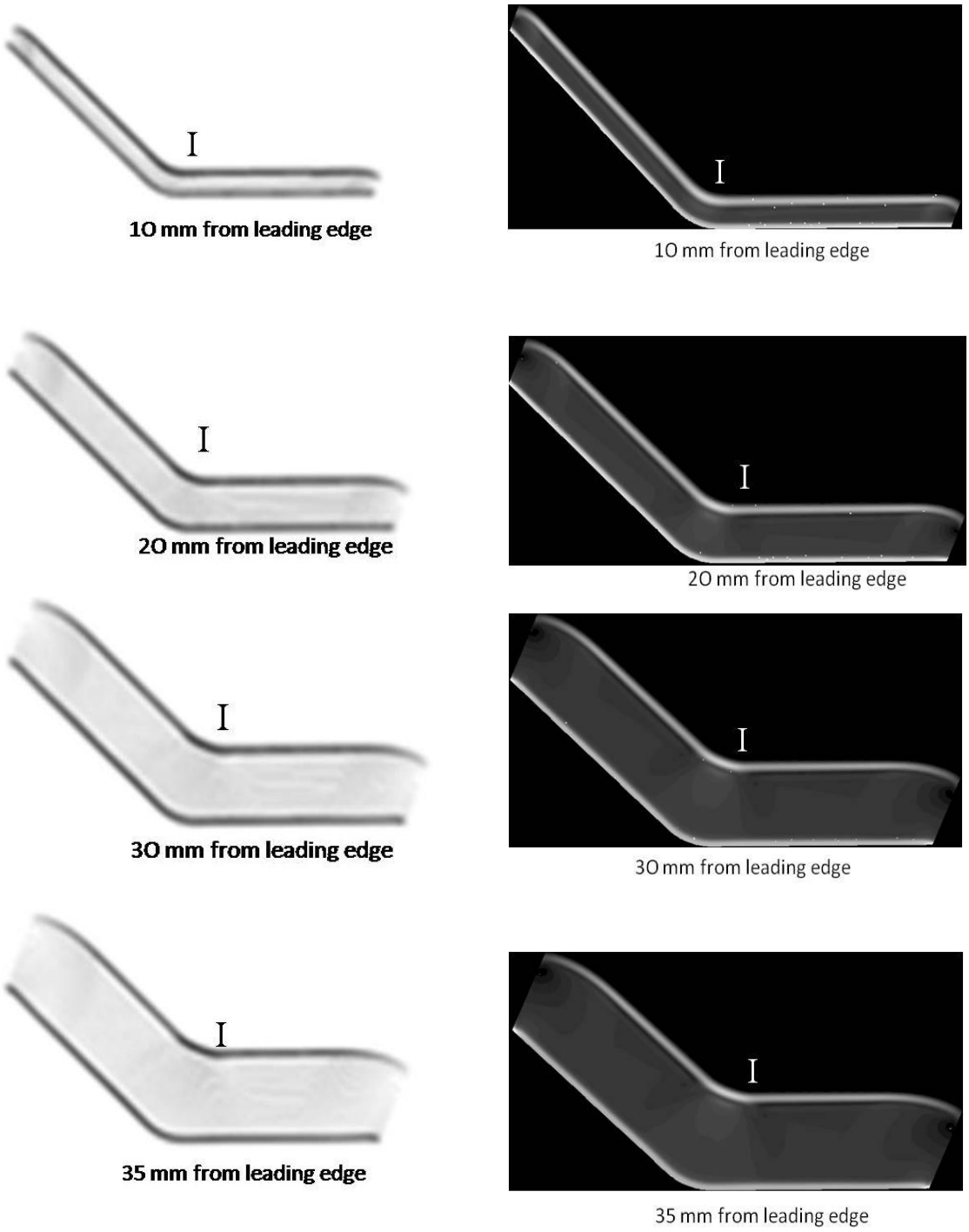

Figure 7. 4: Shock structure cross sections for the 135° fillet geometry, (a) Mach number line contour plots, (b) Numerical schlieren

**Videos showing the transition of the oblique shock waves for these three geometries can be found in the electronic appendix.*

7.2 Iso surfaces showing the formation and development of the shock structure within a supersonic corner

The interaction of shock waves within a simplified supersonic corner produces a complicated three dimensional shock structure. Figures 7.2 to 7.4 are two dimensional cross sections that enable the shock structure to be visualized. Iso surfaces show the formation of the shock structure in both the chordwise and spanwise directions of the respective geometries i.e. iso surfaces aid in the three dimensional visual interpretation of the shock structure.

The iso surfaces presented in the current section are iso surfaces of Mach number. These surfaces are shown from two directions, a front view which shows the formation of the shock structure in the flow direction (labeled *a* on all the images) and a rear view which shows the shock structure from behind (labeled *b* on all the images). These two views illustrate the important flow features associated with the shock formation within a simplified supersonic corner. The important flow features are identified on each figure. These flow features include the incident and reflected waves, the Mach stem, the shear layers and the shock wave boundary layer interaction (SWBLI). Figures 7.5 to 7.7 shows the iso surfaces for the three geometries mentioned in Section 7.1. These geometries are the 90 degree dihedral angle fillet and sharp corner profiles both of which had a 10 percent thickness/chord ratio and the 135 degree dihedral angle geometry with a 3 percent thickness/chord ratio. The complete set of iso surfaces for the geometries listed in Table 6.7 can be found in Appendix B.

The iso surfaces in Figures 7.5 to 7.7 emphasize the formation of the shock structures for the above mentioned geometries i.e.:

- The shock structure for the 135 degree fillet geometry remains a smooth curved wave ;
- The shock structure for the 90 degree fillet geometry transitions from a smooth curved wave to a wave with discontinuities in slope; and
- The shock structure for the 90 degree sharp corner geometry occurs at the leading edge of the geometry.

The important flow features established from the iso surfaces are as follows:

90° Fillet profile

- The oblique incident wave goes from a smooth curved wave to a wave with discontinuities in slope irrespective of the thickness/chord ratio;
- The shock intensity increases with increasing thickness/chord ratio; and
- The formation of the reflected wave is evident for the 3% thickness/chord ratio geometry but these waves do not propagate onto the surface.

120° Fillet profile

Similar features to that mentioned for the 90° fillet profile.

135° Fillet profile

- The 3% thickness/chord ratio geometry shows no Mach reflection. (Also seen in Figure 7.4);
- Transition is established for the 6% and 10% thickness/chord ratio geometries; and
- The shock intensity increases with increasing thickness/chord ratio;

90°, 120° and 135° Sharp Corner profiles

- The formation of the Mach reflections occur at the leading edge of the sharp corner profiles irrespective of the dihedral angles and thickness/chord ratios utilized;
- The shock intensity increases with increasing thickness/chord ratio; and
- The reflected waves always propagate onto the surface irrespective of the thickness/chord ratios and dihedral angles.

135° dihedral angle fillet profile, 3% thickness/chord ratio

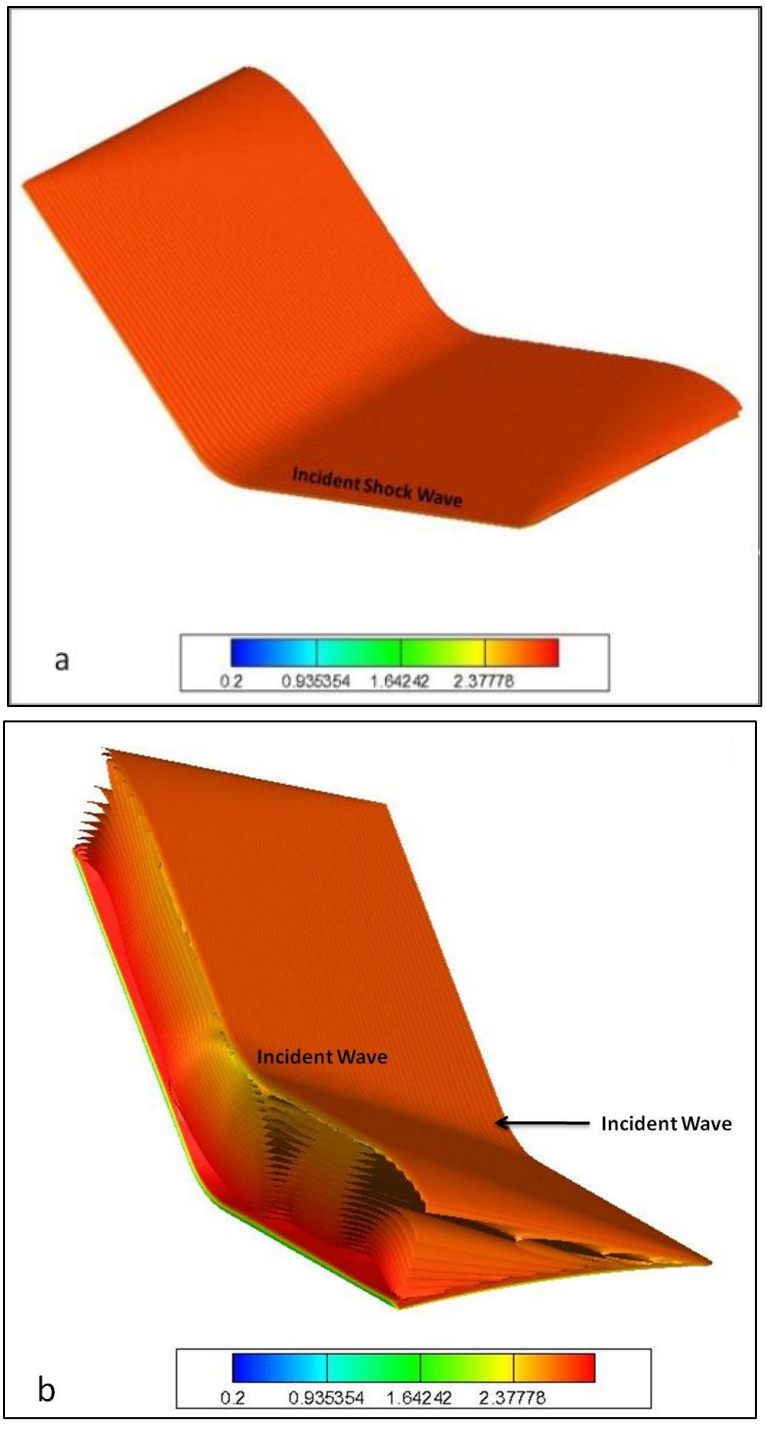

Figure 7. 5: Iso surfaces of Mach number for the 135° dihedral angle 3% thickness/chord ratio fillet geometry, Isometric views, (a) Front, (b) Rear

90° dihedral angle fillet profile, 10% thickness/chord ratio

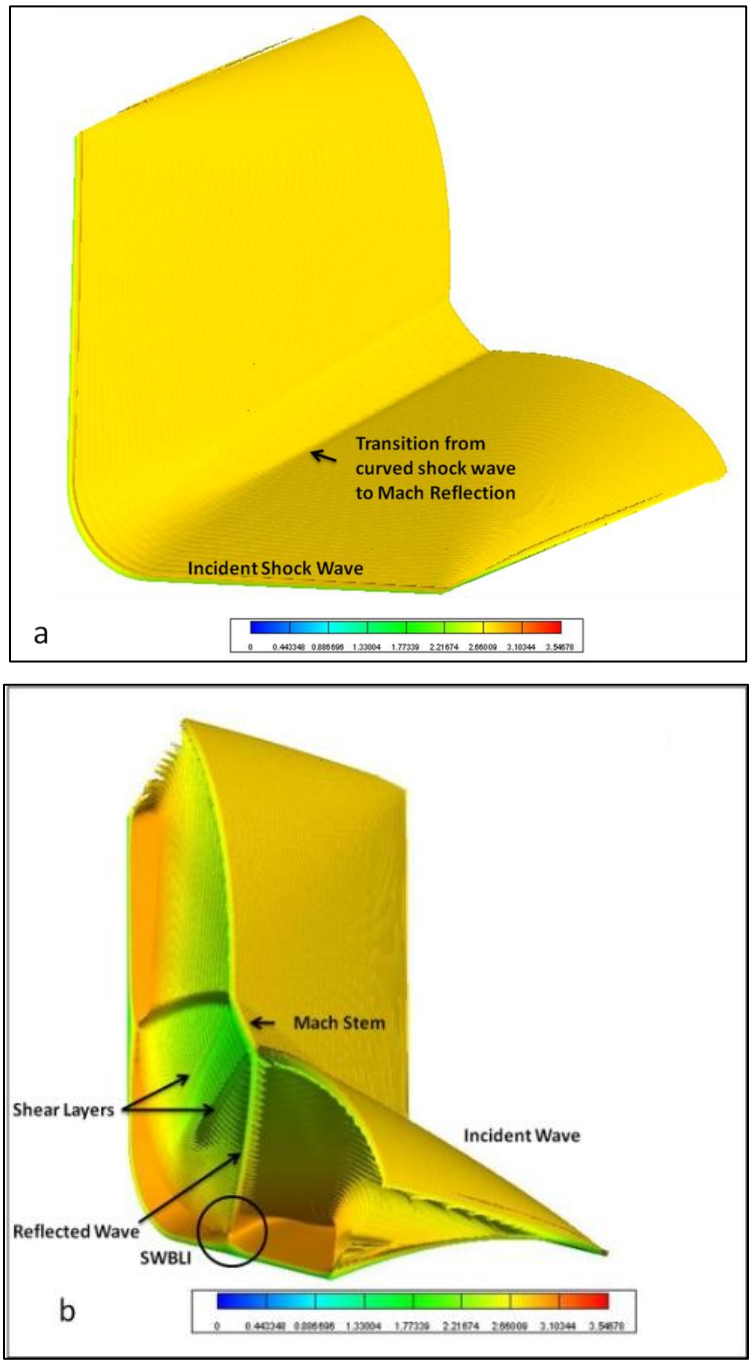

Figure 7. 6: Iso surfaces of Mach number for the 90° dihedral angle 10% thickness/chord ratio fillet geometry, Isometric views, (a) Front, (b) Rear

90° dihedral angle sharp corner profile, 10% thickness/chord ratio

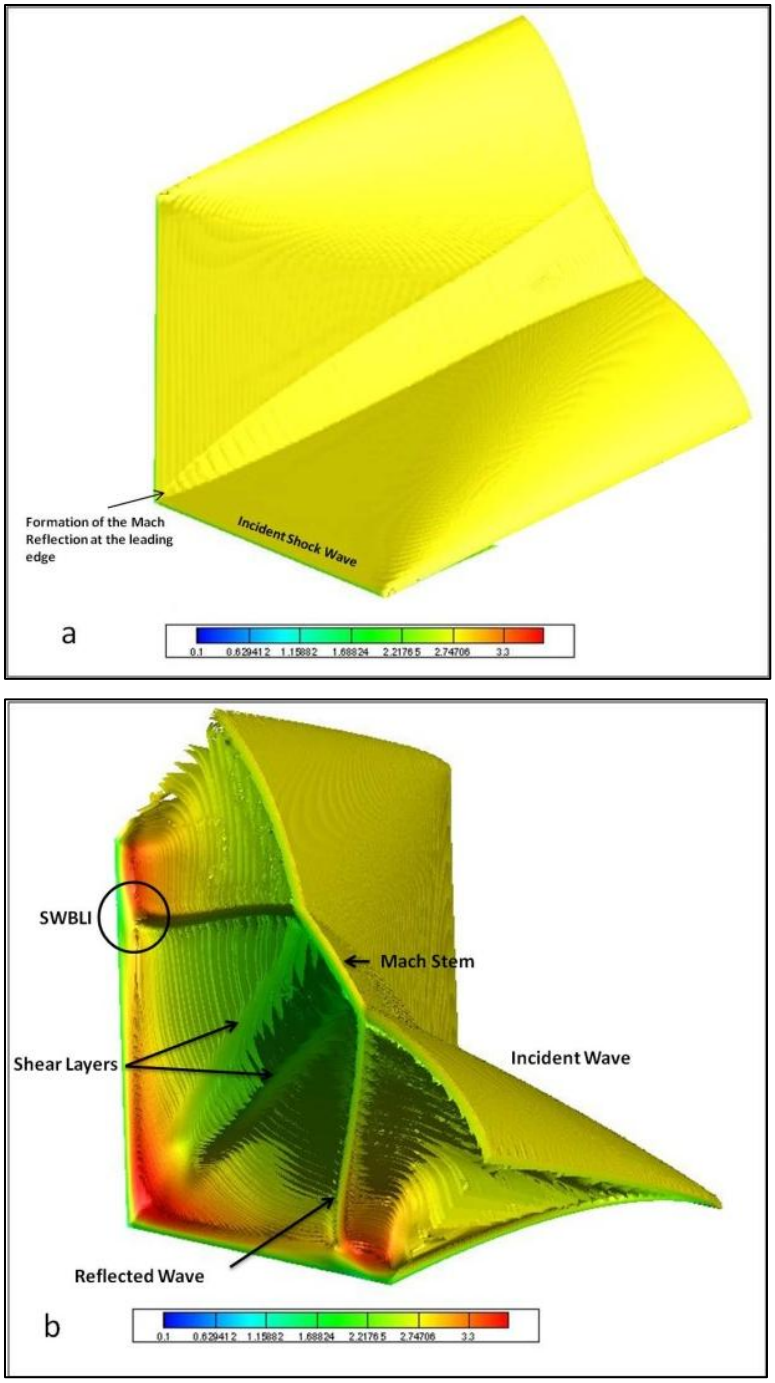

Figure 7. 7: Iso surfaces of Mach number for the 90° dihedral angle 10% thickness/chord ratio sharp corner geometry, Isometric views, (a) Front, (b) Rear

The length of the Mach stem and transition point is also established from the iso surfaces. Figure 7.8 plots the length of the Mach stem surface against the thickness/chord ratios for each dihedral angle for both the fillet and sharp corner geometries (Figure 7.8*a* and 7.8*b*). The length of the Mach stem is seen to increase with an increase in the t/c ratio for each dihedral angle i.e. the larger the dihedral angle, the longer the length of the Mach stem surface. The position of the marker for the 135 degree dihedral angle, 3 percent t/c ratio geometry is on the zero axis as it has been established that the formation of the Mach reflection does not occur. With the exception of this geometry, all the other 135 degree dihedral angle geometries produce the longest Mach stem surfaces. Figure 7.9 plots the transition point against the thickness chord ratio for the fillet geometries. The point of transition of the oblique incident shock wave from a smooth curved wave to a wave with discontinuities in slope moves further forward (closer to the leading edge) with an increase in the t/c ratio. This change in transition point is very slight for the 90 degree dihedral angle geometries when compared to the larger dihedral angle geometries which show that the point of transition varies substantially along the chord with an increase in the t/c ratio.

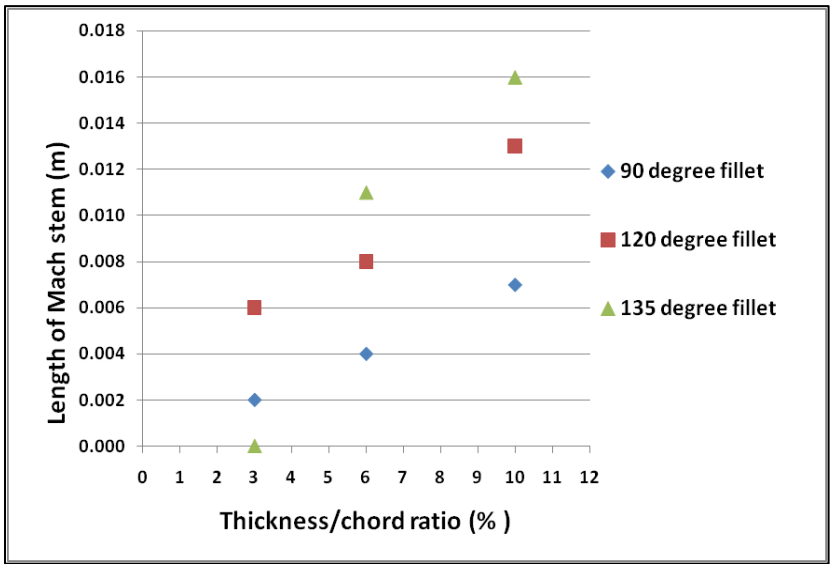

(a)

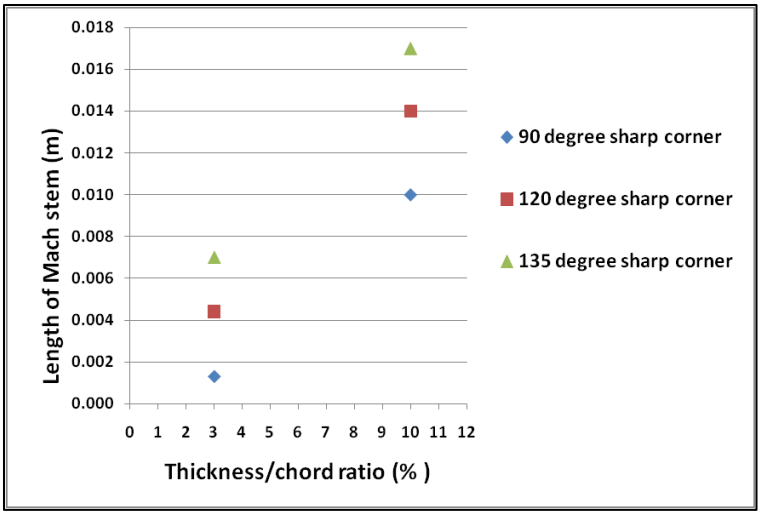

(b)

Figure 7. 8: Graphs of Mach stem length for varying t/c ratios and dihedral angles, (a) fillet profile, (b) sharp corner profile

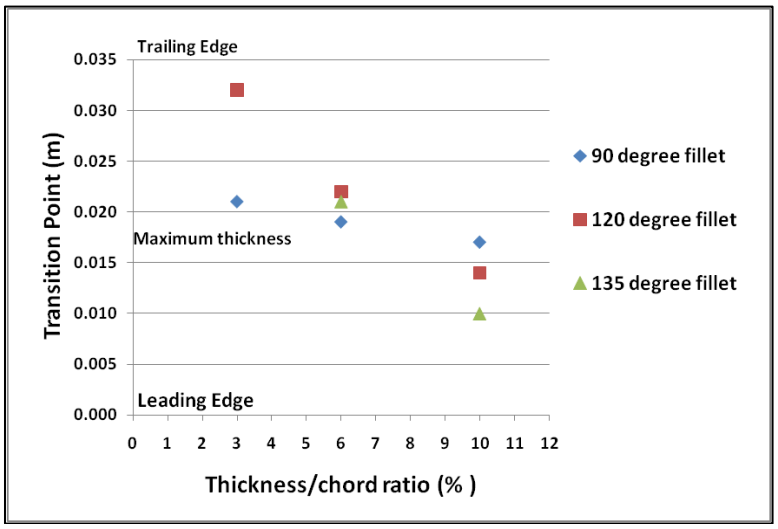

Figure 7. 9: Graphs of variation in transition point for varying t/c ratios and dihedral angles

7.3 Pressure, shear stress and Mach number distributions

The changes in the pressure, shear stress and Mach number are dependent on the geometric characteristics i.e. the presence or absence of a fillet profile, the dihedral angle and the thickness/chord ratio. Figures 7.10, 7.11 and 7.12 depict the numerical results for the above mentioned thermodynamic properties for the 90 degree fillet and sharp corner profiles, both of which have a 10 percent thickness/chord ratio as well as the 135 degree fillet profile which has a 3 percent thickness/chord ratio (these three geometries are the same geometries presented in Sections 7.1 and 7.2). These values are taken at a height of 1 E -04 m above the surface of the geometry. The freestream Mach number is Mach 3.0.

Figure 7.10 shows the pressure, shear stress and Mach number contour plots for the 90 degree fillet geometry, from which it is seen that the formation of the Mach reflection occurs at approximately 50% chord. Before this point the oblique shock wave is a continuous curved wave and the resultant effect on the thermodynamic properties is evident. The change in the pressure, shear stress and Mach number is gradual up until the point of maximum thickness and are a result of the incident shock wave only. Thereafter the impact of the reflected wave back onto the surface affects these properties. Although the formation of the shear layer is evident and can be seen in Figure 7.2, the direct impact of the shear layer on the surface pressure is negligible as the shear layer is away from the surface. The reflected shock wave has a greater influence on the surface pressure and shear stress profiles than the shear layer. This effect is seen for all the geometries that illustrate transition i.e. transition of a smooth curved incident oblique wave to a wave with discontinuities in slope.

Figure 7.3 showed the development of the shock structure for the 90 degree sharp corner geometry, from which it is seen that the formation of the Mach reflection and shear layer start at the leading edge of the geometry. The variation for this case is that the shear layer initially propagates onto the surface. This has a direct impact on the surface pressure, shear stress and Mach number distributions. The shear layer causes an increase in the shear stress and pressure at the leading edge of the geometry. Figure 7.11 shows the surface pressure, shear stress and Mach number distributions for the 90 degree sharp corner geometry. As the shock structure evolves the

shear layer grows with the Mach reflection and gradually pulls away from the surface. The effect of the shear layer is thus only evident at the leading edge of the geometries; thereafter the reflected wave affects the pressure, shear stress and Mach number distributions. This effect is seen for all the sharp corner geometries.

By varying the dihedral angle and the thickness/chord ratio, the changes in the flow properties are clearly evident. Increasing the dihedral angle results in a decrease in the strength of the Mach stem surface; this had a direct impact on the formation of the Mach reflection and the shear layer. The same effect is seen when decreasing the thickness/chord ratio. Figure 7.12 shows the numerical results for the surface pressure, shear stress and Mach number distributions for the 135 degree dihedral angle geometry which has 3 percent thickness/chord ratio. Due to the delay in the formation of the Mach reflection, the changes in the pressure, shear stress and Mach number result from the incident oblique shock wave only.

The changes in the aforementioned thermodynamic properties are dependent on the formation of the shock structures. The transition of the shock structure results in the pressures, shear stresses and Mach numbers initially being affected by the oblique incident wave but once transition occurs, these changes are affected by the reflected waves. The formation of the Mach reflection at the leading edge, results in these thermodynamic properties being initially affected by the shear layer and the reflected waves.

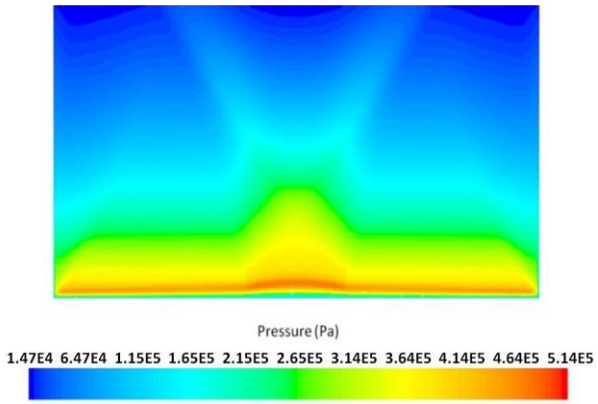

(a)

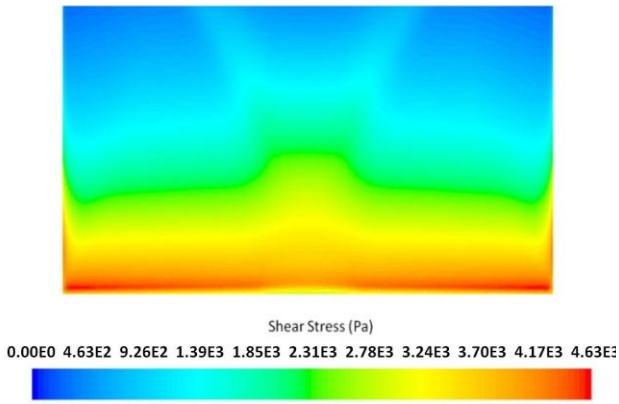

(b)

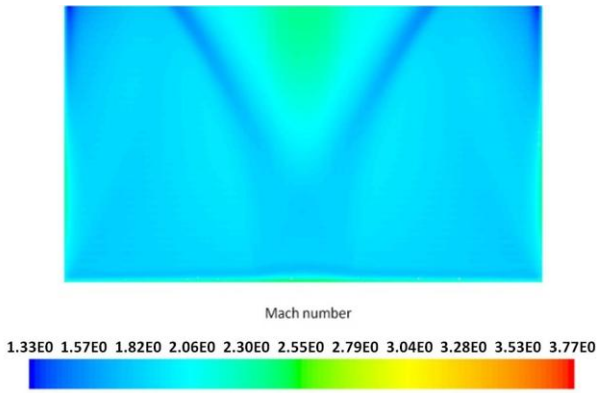

(c)

Figure 7. 10: Surface properties for the 90° fillet geometry, (a) Pressure (Pa), (b) Shear stress (Pa), (c) Mach number

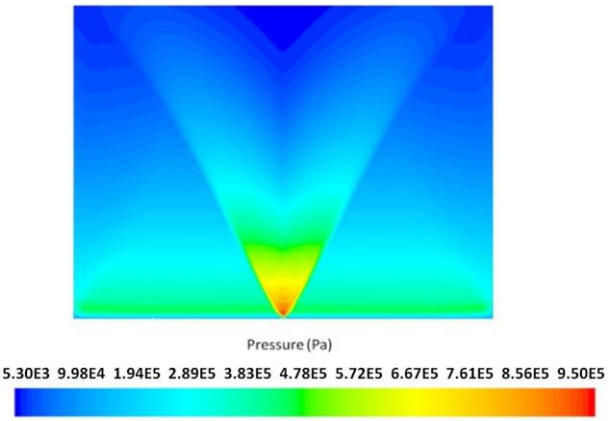

(a)

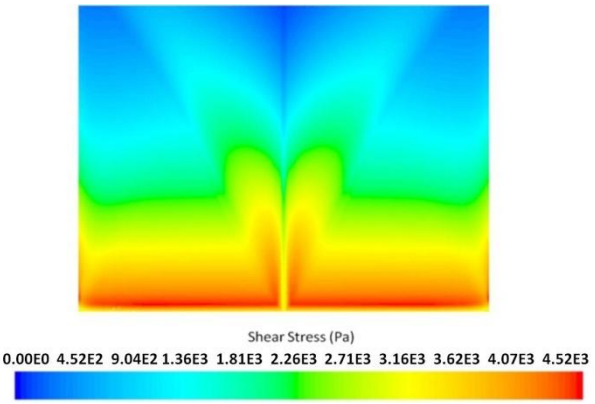

(b)

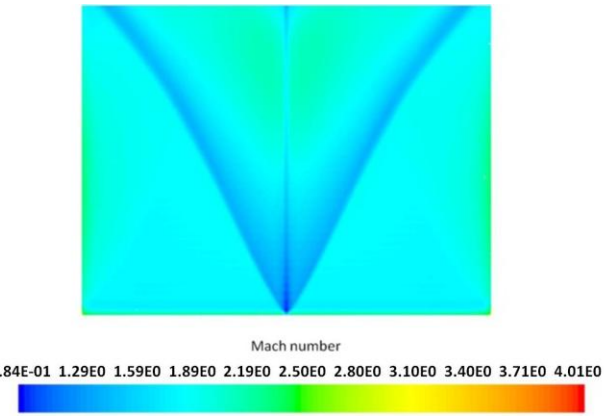

(c)

Figure 7. 11: Surface properties for the 90° sharp corner geometry, (a) Pressure (Pa), (b) Shear stress (Pa), (c) Mach number

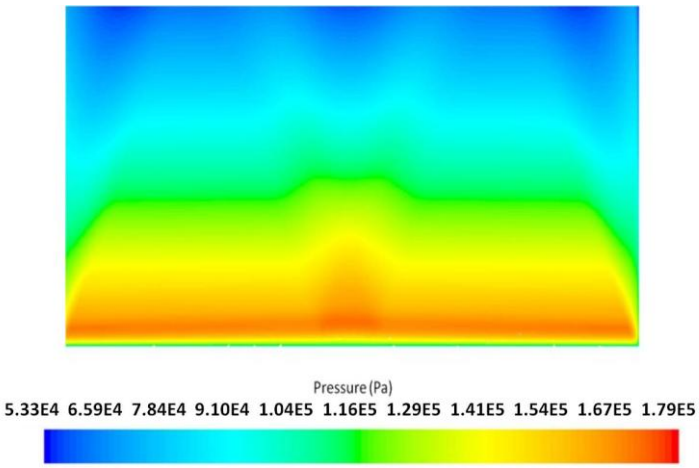

(a)

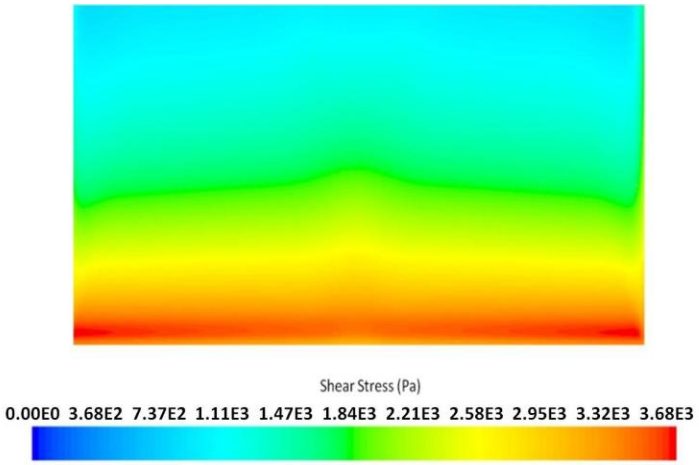

(b)

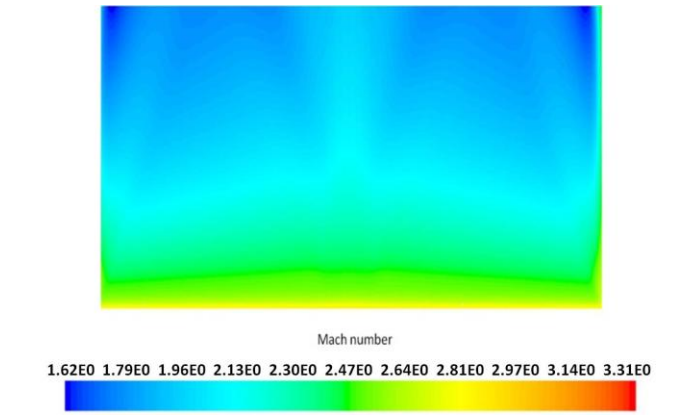

(c)

Figure 7. 12: Surface properties for 135° fillet geometry, (a) Pressure (Pa), (b) Shear stress (Pa), (c) Mach number

7.4 Influence of varying dihedral angles and thickness/chord ratios

The effect of varying the dihedral angles and thickness/chord (t/c) ratios on the shock formation was seen in Section 7.2. The iso surfaces showed the changes in formation of the shock structure with varying geometric parameters. The following section presents line plots of pressure for the geometries presented in Table 6.7. These pressure plots compare the variation in pressure by keeping the t/c ratio constant and varying the dihedral angle or vice versa. A comparison of the variation in pressure between the fillet and sharp corner profiles for a specific t/c ratio is also presented. These pressure values are taken at a height of 1mm above the surface of the geometry and track the changes along the centre of the geometry (supersonic fillet or sharp corner) in the chordwise direction.

Figure 7.13 shows the line plots of pressure for the fillet (a-c) and sharp corner (d-f) geometries respectively. These pressure plots are computed for each dihedral angle while varying the t/c ratios. The results show that a larger t/c ratio induces a higher pressure along the supersonic corner irrespective of the dihedral angle of the geometry. However the decrease in pressure in the chordwise direction is more significant for the geometries with the higher t/c ratios, with the pressure at the trailing edge being the lowest for the geometries that had a 10 percent t/c ratio when compared to the 3 and 6 percent t/c ratio geometries i.e. the larger the t/c ratio, the greater the decrease in pressure along the supersonic fillet and sharp corner.

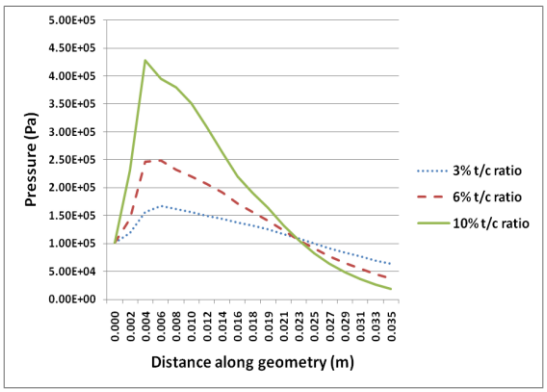

(a) 90° Fillet profile

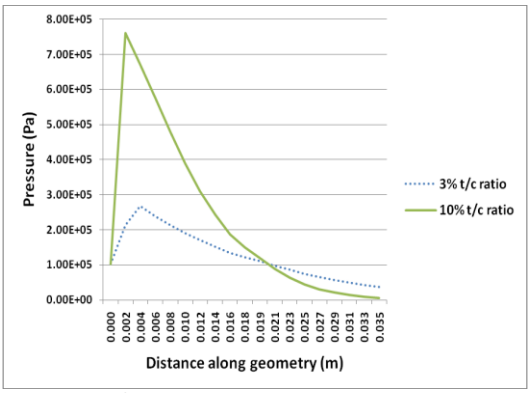

(d) 90° Sharp Corner Profile

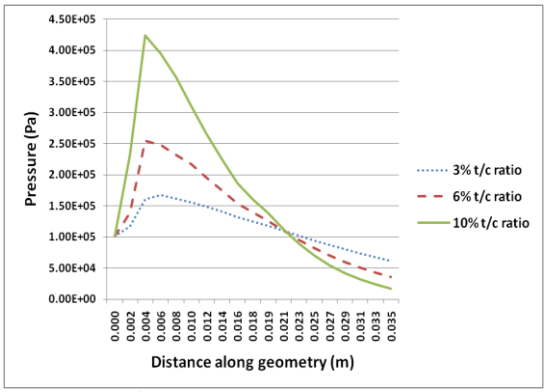

(b) 120° Fillet profile

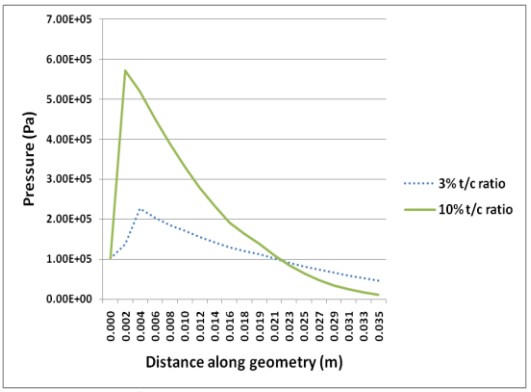

(e) 120° Sharp Corner Profile

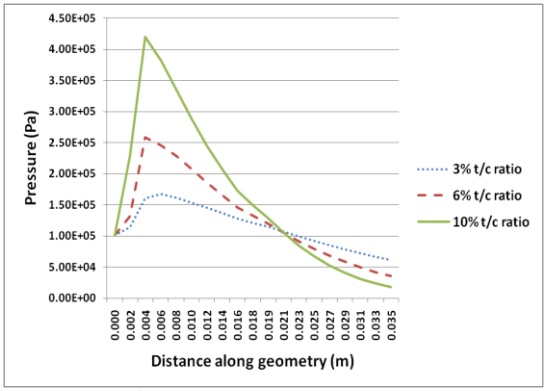

(c) 135° Fillet profile

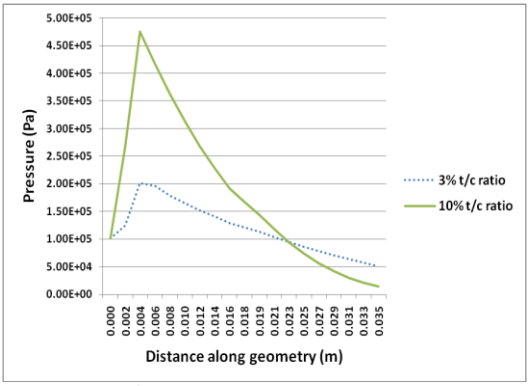

(f) 135° Sharp Corner Profile

Figure 7. 13: Graphs of pressure variation for different thickness/chord ratios for the fillet (a-c) and sharp corner (d-f) geometries

The pressure plots computed in Figure 7.14 are for each t/c ratio while varying the dihedral angles. These results show that for each t/c ratio the pressure variation along the supersonic fillet corner is similar irrespective of the dihedral angle. A slightly higher pressure is seen for the 90 degree dihedral angle geometries resulting in a more clearly defined formation of the Mach reflection (as seen in Section 7.2) when compared to the 120 and 135 degree dihedral angle geometries. The pressure variation for the supersonic sharp corner differs from the pressure variation for the fillet profile. The difference in pressure between each dihedral angle for the same t/c ratio is more pronounced.

Figure 7.15 shows pressure plots that draw a comparison between the fillet and sharp corner geometries for each t/c ratio and dihedral angle. These results show that the sharp corner geometries always produce a higher peak pressure irrespective of the t/c ratio or dihedral angle when compared to the fillet geometries. The sharp corner profiles also show a greater decrease in pressure within the supersonic corner, with the pressure at the trailing edge always lower than that of the fillet profile. The pressure difference between the fillet and sharp corner profiles for the same t/c ratio and dihedral angle is also seen to decrease as the dihedral angle of the geometries increases i.e. the pressure difference between the fillet and sharp corner geometries which have a 135 degree dihedral angle is much smaller when compared to the difference in pressure for the 90 and 120 degree dihedral angle geometries.

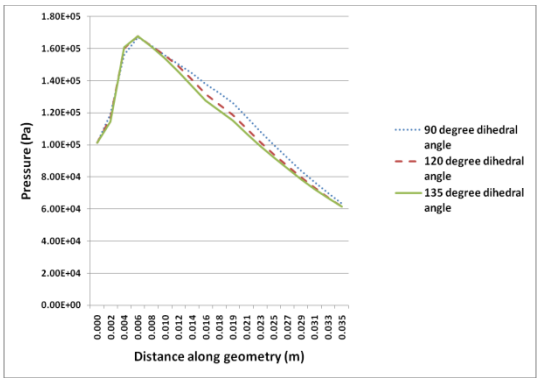

(a) 3 percent t/c ratio, Fillet profile

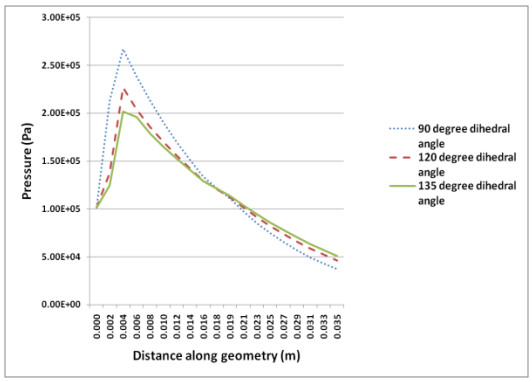

(d) 3 percent t/c ratio Sharp Corner profile

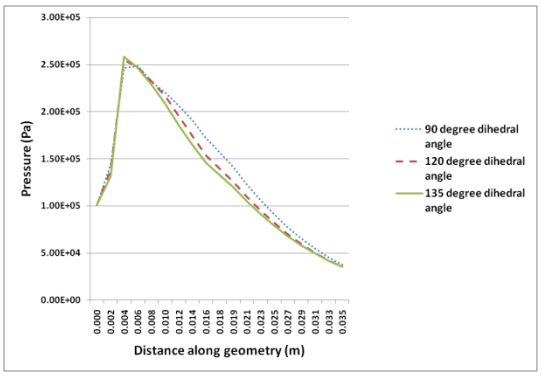

(b) 6 percent t/c ratio, Fillet profile

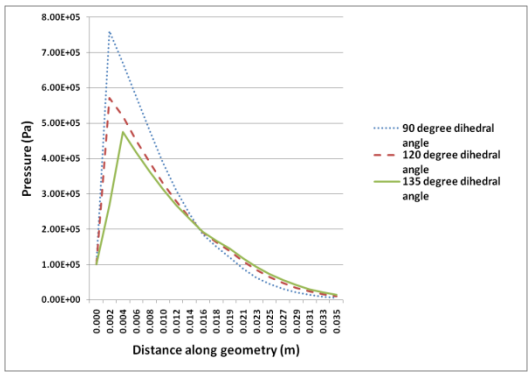

(e) 10 percent t/c ratio Sharp Corner profile

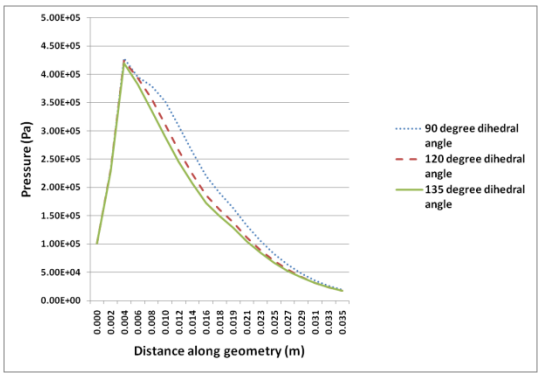

(c) 10 percent t/c ratio, Fillet profile

Figure 7. 14: Graphs of pressure variation for different dihedral angles for the fillet (a-c) and sharp corner (d, e,) geometries

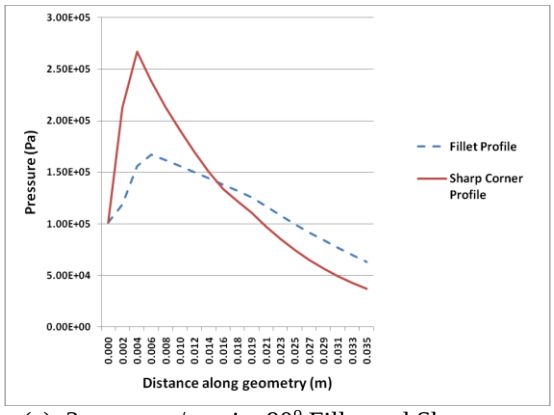

(a) 3 percent t/c ratio, 90° Fillet and Sharp corner profiles

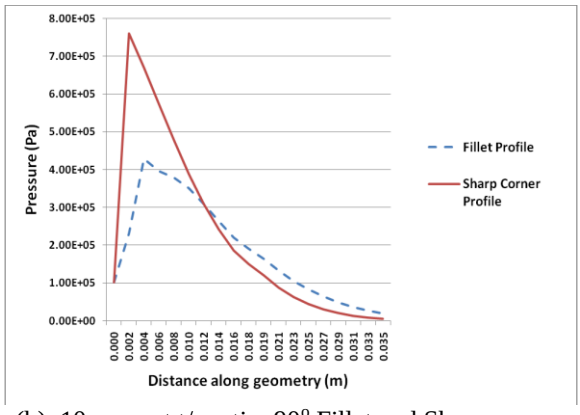

(b) 10 percent t/c ratio, 90° Fillet and Sharp corner profiles

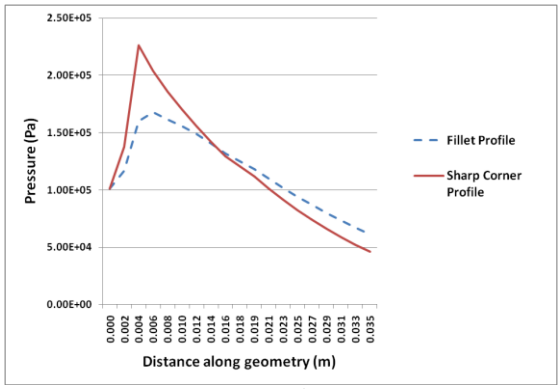

(c) 3 percent t/c ratio, 120° Fillet and Sharp corner profiles

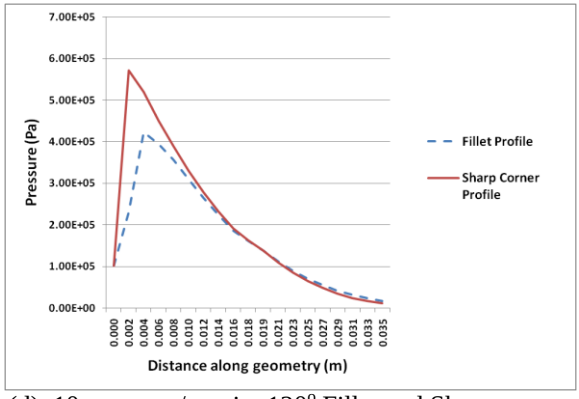

(d) 10 percent t/c ratio, 120° Fillet and Sharp corner profiles

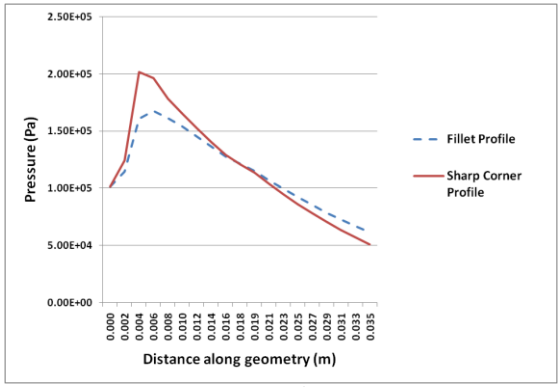

(e) 3 percent t/c ratio, 135° Fillet and Sharp corner profiles

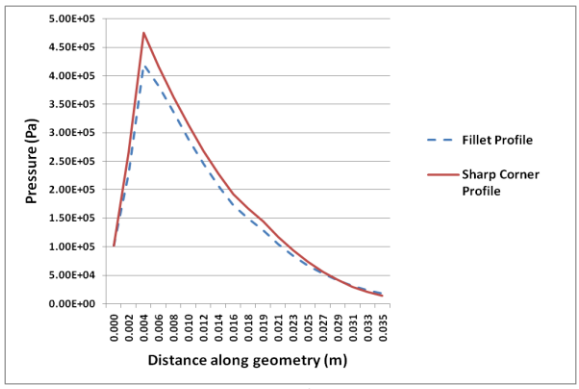

(f) 10 percent t/c ratio, 135° Fillet and Sharp corner profiles

Figure 7. 15 : Graphs comparing pressure variation for the 90,120 and 135 degree fillet and sharp corner geometries for the 3 percent (a, c, e) and the 10% percent (b, d, f) t/c ratios

7.5 Influence of varying fillet radii and Mach numbers on the shock formation

The effect of varying the dihedral angles and thickness/chord (t/c) ratios on the shock formation was seen in Section 7.2 and 7.4. A study was conducted to explore the effect of varying the fillet radii and Mach numbers on the shock formation within a supersonic fillet and sharp corner. Numerical simulations were conducted on the geometries presented in Table 6.6 and Table 6.8. These geometries had varying fillet radii which were calculated as a percentage of the chord length. The fillet radii were 20%, 30%, 40%, 50%, and 60% of the chord length. These fillet radii were simulated with different Mach numbers (M 2.5, M 3.0, and M 5.0). A comparison is also drawn with the sharp corner geometry as this geometry is ultimately a fillet profile with a 0% fillet radius. All these geometries had a 10 percent thickness/chord ratio and a 90 degree dihedral angle. The results presented make use of terms such as Fillet20, Fillet30 etc. These terms refer to the fillet geometries which have a 20% or 30% fillet radius. The effect of varying the Mach number on the shock formation is also presented for the sharp corner geometries.

7.5.1 Variation of pressure associated with different fillet radii and Mach numbers

A comparison is made between the varying fillet radii and sharp corner geometries by comparing line plots of pressure. These pressure values are taken at a height of 1mm above the surface of the geometry in the spanwise direction starting at the centre of the supersonic corner and moving outward along the wing semi span at the trailing edge. These values were taken at the trailing edge as it was established in Sections 7.1 and 7.2 that the shock structure is fully developed at the trailing edge. The pressure plots are shown for each free stream Mach number. The variation in pressure for each freestream Mach number is shown in Figure 7.16.

The pressure plots are an insight into the variation of pressure within the supersonic corner and along the wing semi span for an increase in the fillet radius and freestream Mach number. The initial increase in pressure for each fillet radius line plot results from the initial pressure increase at the trailing edge within the supersonic corner. The subsequent decrease in pressure is a result of the flow across the reflected shock wave. Thereafter all the line plots plateau to the 2D pressure value on the wing semi span i.e. the pressure value that doesn't include the effect of the supersonic fillet or sharp corner.

The general trend shown for all the freestream Mach numbers is that the sharp corner profiles always produce a lower pressure at the centre of the supersonic corner at the trailing edge when compared to the fillet profiles. An increase in the fillet radii i.e. 0% to 60% results in an increase in pressure in the centre of the supersonic corner at the trailing edge for all the simulated freestream Mach numbers. The shock intensity for the sharp corner profiles was established to be much higher when compared to the fillet profiles; this effect is again evident in Figure 7.16. As the fillet radius decreases (60% to 0%) the shock intensity increases, resulting in a well formed Mach reflection for the smaller radius geometries. This is seen by the rapid increase in pressure for the smaller fillet radius geometries.

The results also show that for the lower freestream Mach number (M 2.5) the pressure variation for the smallest fillet radii (Fillet20) is similar to that of the sharp corner geometry even though the formation of the Mach reflection is slightly delayed for the Fillet20 geometry. As the fillet radius decreases (60% to 0%) the pressure variation at the trailing edge becomes similar which results in the formation of the Mach reflection being similar for the smaller fillet radii geometries at lower Mach numbers. The increase in pressure for each fillet radius line plot also indicates the strength of each reflected wave. A higher increase in pressure indicates a stronger reflected wave. The line plots for the simulation conducted at Mach 2.5 show that irrespective of the fillet radius there is always an increase in pressure which indicates that the formation of the Mach relfection is established for all the geometries that were simulated at Mach 2.5.

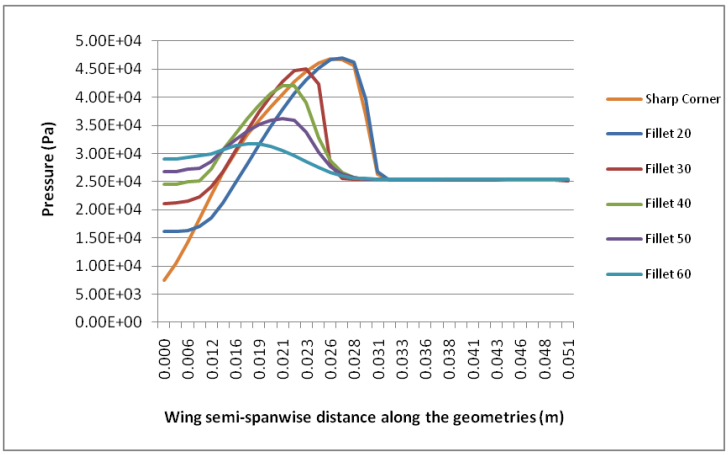

(a) Mach 2.5

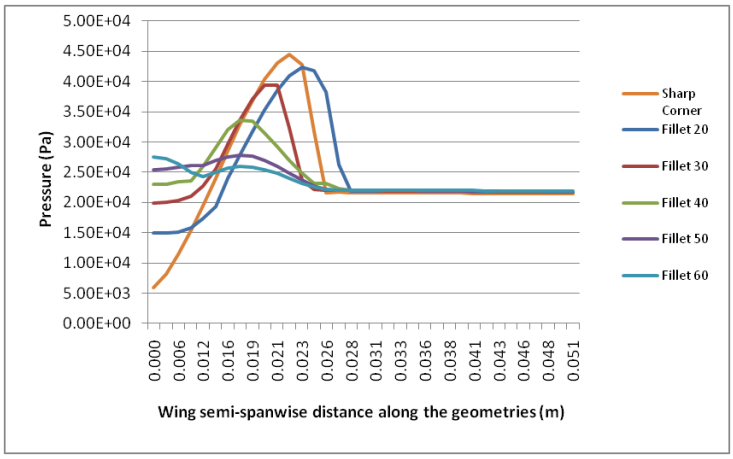

(b) Mach 3.0

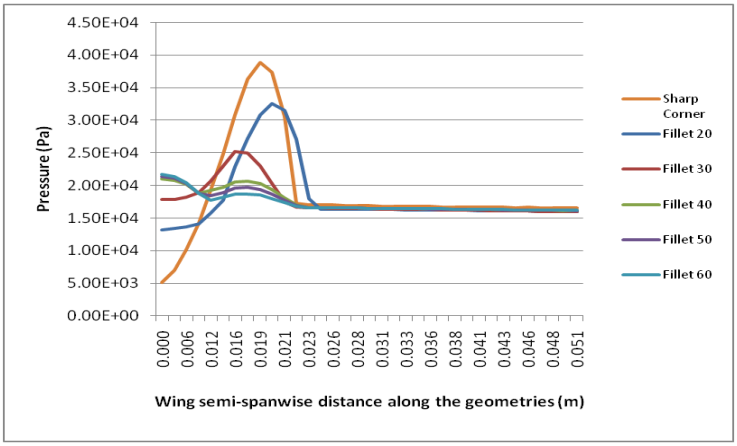

(c) Mach 5.0

Figure 7. 16: Graphs comparing pressure variation for the sharp corner and varying fillet radii geometries for varying freestream Mach numbers, (a) Mach 2.5, (b) Mach 3.0 and (c) Mach 5.0

7.5.2 Influence of varying fillet radii and Mach number on the transition point

It was established in Section 7.1 and 7.2 that the inclusion of a fillet profile delays the formation of the Mach reflection for the 90 degree dihedral angle geometries i.e. the transition from a smooth curved wave to a wave with discontinuities in slope occurs at a certain distance away from the leading edge of the geometry. By varying the fillet radius and Mach number, this transition point varies along the chord of the geometry.

These transition points are shown in Figure 7.17. Figure 7.17 plots the fillet radius against the transition point for the three simulated Mach numbers. For each Mach number the transition point moves further aft of the leading edge as the fillet radius increases (the leading edge is shown at the origin of the y axis on Figure 7.17). As the fillet radius increases the shock intensity decreases which causes the transition point to move further aft of the leading edge.

When comparing the transition point for each fillet radius with increasing Mach number i.e. comparing the point of transition for the 20% fillet radius geometries with increasing Mach number, it is seen that an increase in the Mach number results in the transition point moving further aft of the leading edge for the same fillet radius. This is due to the fact the higher Mach number (M 5.0) produces a lower incident shock angle resulting in the transition point of the oblique shock wave occurring further aft of the leading edge when compared to the higher shock angles produced by Mach 2.5 and Mach 3.0

The ∞ symbol seen on the Mach 5.0 transition points for the 60% fillet radius is used to show that transition does not occur because the oblique shock wave remains a smooth curved wave. The low shock angle and the low shock intensity resulting from the 60% fillet radius both delay the formation of the Mach reflection.

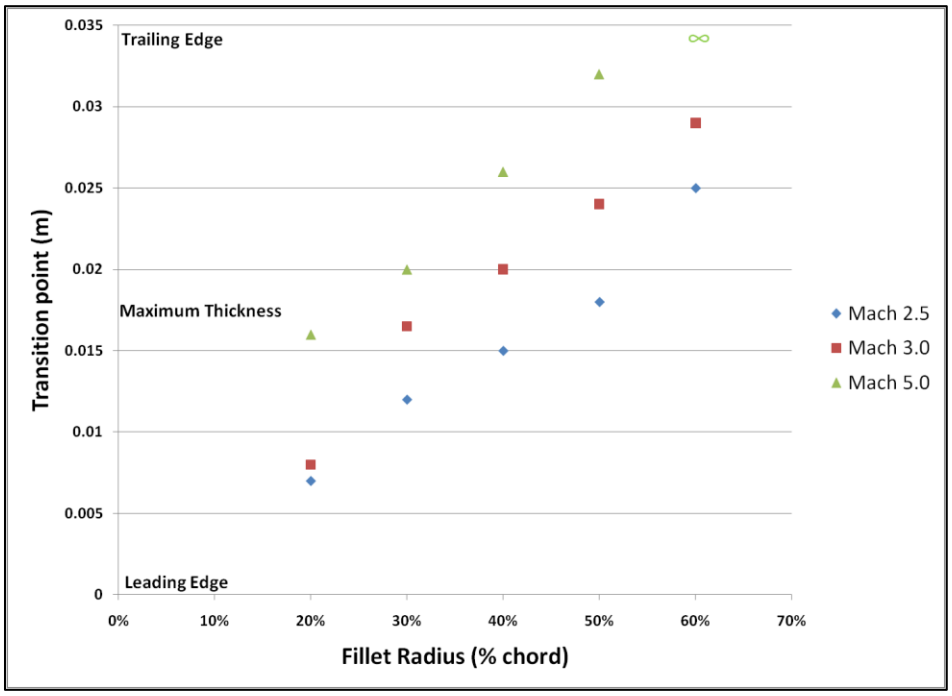

Figure 7. 17: Graph of fillet radius vs. transition point for varying Mach numbers

7.6 Influence of varying camber profiles on the shock formation

All previous research, both experimental and numerical, conducted on supersonic corner flows utilized plane wedge geometries as its camber profile (Section 3.2). The current study utilized a circular arc camber profile. The effect of varying the camber profile on the shock formation is presented in the current section. Wedge geometries with the same leading edge angle (22°) as the circular arc geometries were created. The circular arc geometry has both an increase and decrease (from the point of maximum thickness) in gradient along the geometry in the chordwise direction. However the wedge geometry only has an increase in gradient along the geometry in the chordwise direction. The effect of this change in gradient, for the circular arc and wedge geometries, on the shock formation is compared and presented in the form of numerical schlieren images.

Goonko *et al.* [16] completed a study on a geometry that had a 15 degree wedge angle which was simulated at Mach 6. The results produced showed that a complicated double Mach reflection is established for high wedge angles and Mach numbers. The results presented in this section will compare the wedge and circular arc geometries that were simulated at Mach 5.0.

Figure 7.18 shows the numerical schlieren images for the wedge and circular arc geometries. These images are taken at the trailing edge of the respective geometries. The change in gradient for the circular arc geometries has a significant impact on the formation of the shock structure when compared to the wedge geometries. The shock structure for the circular arc geometry is seen in Figure 7.18*a*. This shock structure is similar to that seen in Section 7.1 for the sharp corner geometries that were simulated at Mach 3.0. The formation of the Mach reflection is again evident. The incident (1) and reflected (2) shock waves as well as the Mach stem (3) and shear layers (4) are all clearly defined.

Figure 7.18*b* shows the numerical schlieren image for the geometry that utilizes the wedge camber profile. The shock structure established is that of the aforementioned double Mach reflection (similar to that seen by Goonko *et al*). The double Mach reflection has two triple points. The first triple point has the incident (1) and reflected (2) shock waves as well as the Mach stem (3) and shear layers (4). The second triple point consists of the secondary reflected shock wave (6), the near wall Mach stem (7) and a secondary shear layer. This secondary shear layer is not visually evident on the numerical schlieren image. The secondary reflected shock (6) is formed due to the fact that flow behind the initial reflected shock (2) is supersonic. Another important feature associated to this shock structure is the spiral vortex (5). As the shear layers approach the wedge surface, it turns upward and rolls up into this spiral vortex. The curvature and change in gradient associated with the circular arc camber profile is seen to produce a significantly lower pressure along the geometries when compared to the wedge cambered profiles, resulting in a change in the shock formation for the wedge geometries.

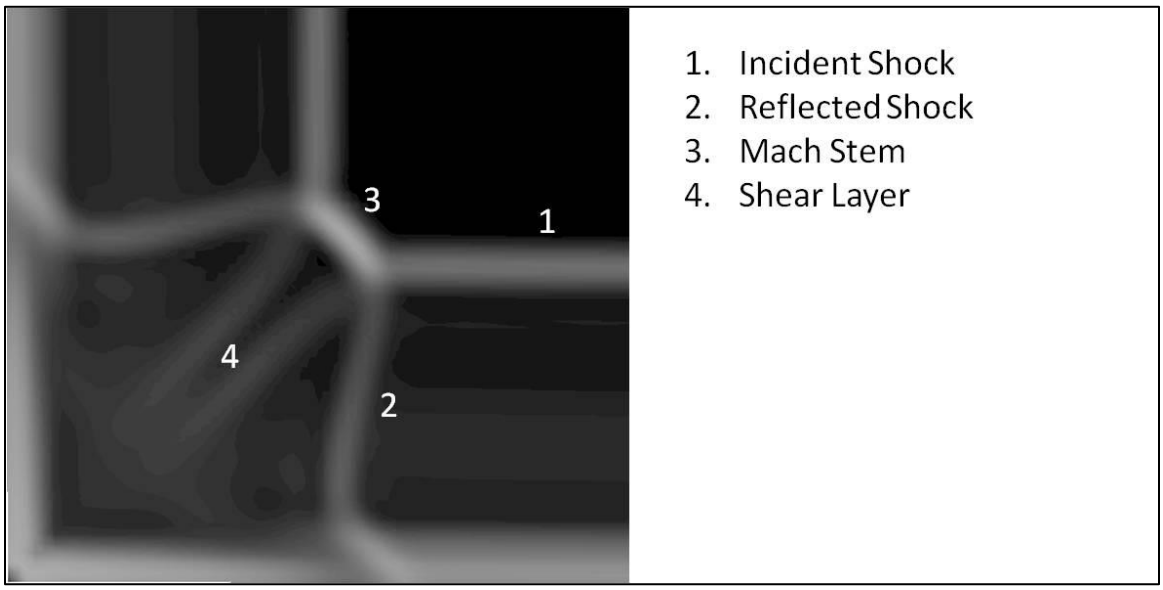

(a)

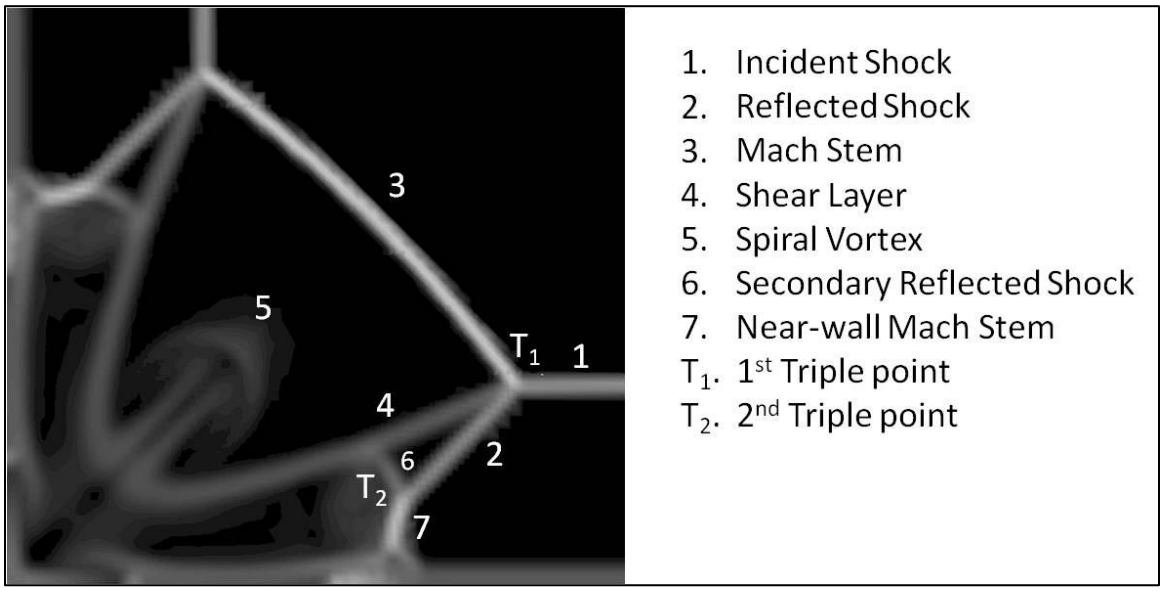

(b)

Figure 7. 18: Numerical schlieren images showing the shock structure for the (a) Circular arc and (b) Wedge geometries

7.7 Shock Wave-Boundary Layer Interaction

The current investigation of the SWBLI is fully three dimensional. The reflected wave impinges on the boundary layer and this impingement is inclined to the flow direction. The numerical and experimental results produced verified that the reflected wave impinges on the surface of the respective geometries. As a result the interaction between the reflected wave and the boundary layer on the surface forms the basis for the shock wave boundary layer investigation.

With the exception of the 135 degree dihedral angle, 3 percent thickness/chord ratio geometry, all the other numerical results produced yielded the three shock structure i.e. the incident and reflected waves as well as the Mach stem were present. The use of the circular arc camber profile resulted in a decrease in gradient of the geometry from the point of maximum thickness (50 percent chord). This decrease in gradient resulted in the pressure gradients, associated with the shock wave boundary layer interaction, not being strong enough to cause reversed flow and a fully separated region for the geometries analyzed i.e. the shock intensity was not high enough to produce flow separations. The boundary layer velocity vectors of Mach number (M_∞=3.0) are shown in Figure 7.19. These vectors are taken at three points within the boundary layer, at the leading edge, midpoint and the trailing edge of the geometry. These velocity vectors do not indicate any reversed flow within the flow field.

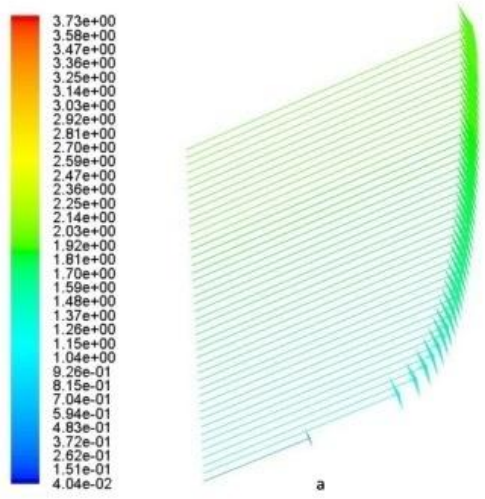

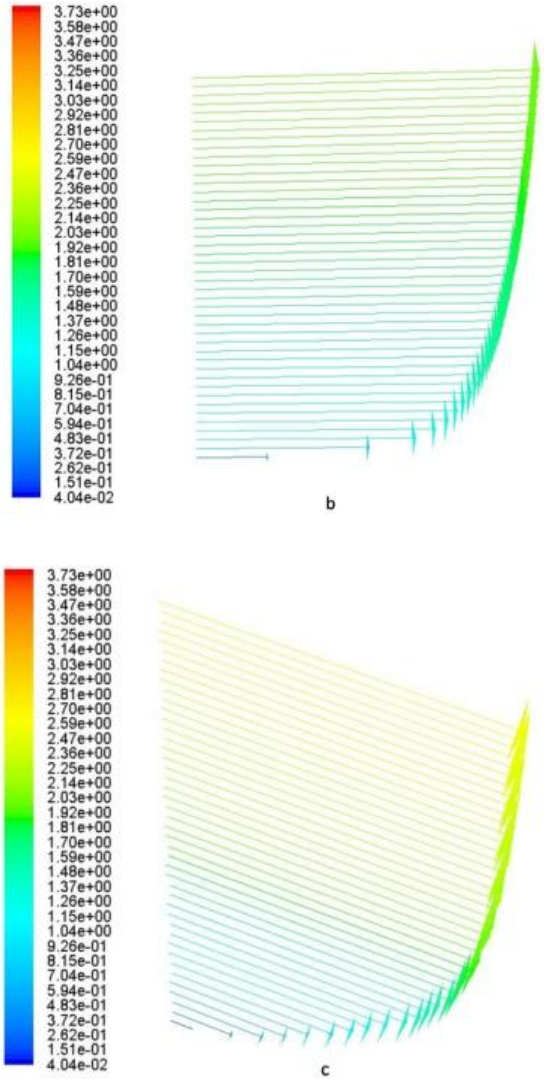

Figure 7. 19: Boundary Layer Velocity Vectors (a) leading edge, (b) midpoint, (c) trailing edge

A further analysis of the numerical results showed that the smaller the dihedral angles of the geometries, the higher the strength of the Mach stem surfaces. These smaller dihedral angles coupled with a larger thickness/chord ratio produced the highest strength shock waves. This had a direct impact on the shock wave boundary layer interaction in that the interaction of the reflected wave and the boundary layer was more pronounced for the 90 degree dihedral angle 10 percent thickness/chord ratio geometries.

As a result of the higher shock intensity for the 90 degree dihedral angle cases, emphasis was placed on the shock wave boundary layer interaction that involved a comparison between the fillet and sharp corner profiles for the 90 degree geometries, both of which had a 10 percent thickness/chord ratio. The freestream Mach number was M 3.0.

This analysis revealed that the impingement of the reflected wave on the boundary layer results in an increase of the boundary layer thickness at this point. The greatest increase or deviation in the boundary layer thickness is seen for the sharp corner profiles. Figure 7.20 shows the thickening of the boundary layer for the 90 degree fillet and sharp corner geometries respectively. The deviation in the boundary layer is shown in the form of Mach number contours. The Mach number contours are taken at the trailing edge of the respective geometries and are close up views of the regions labeled SWBLI in Figures 7.6*b* and 7.7*b*.

The larger variation in the boundary layer thickness between the fillet and sharp corner profiles is evident. Although the boundary layer thickness is seen to increase, the pressure gradients associated with the shock wave boundary layer interaction is not strong enough to cause reversed flow and a fully separated region for the geometries analyzed i.e. the shock intensity was not high enough to produce flow separations.

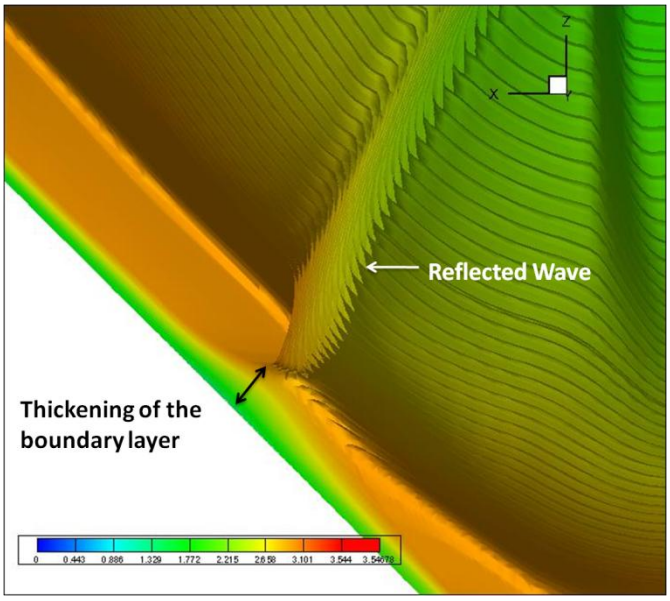

(a)

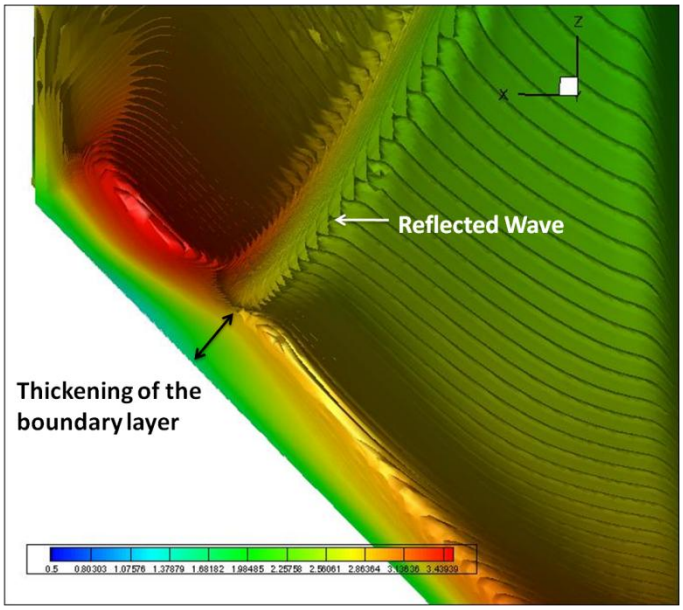

(b)

Figure 7. 20: SWBLI, Mach number contours, thickening of boundary layer for the (a) 90° fillet geometry (b) 90° sharp corner geometry

7.8 Turbulence Modeling: Viscous vs. Inviscid

Previous research conducted on supersonic corner flows utilized an inviscid solver in the flow computations. The current research extended this by including a viscous turbulence model when resolving the numerical solutions for three dimensional supersonic corner flows. The Spalart-Allmaras turbulence model was chosen for the numerical analysis. The current section presents line plots of pressure that draw a comparison between the use of an inviscid solver and the Spalart-Allmaras turbulence model in the flow calculations. The results are presented for the 90 degree dihedral angle sharp corner geometry as it was established in Section 7.7 that this geometry has a higher shock intensity resulting in a greater shock wave boundary layer interaction when compared to the other fillet and sharp corner geometries. The pressure values are taken at a height of 1mm above the surface of the geometry. The results are presented for each simulated Mach number and are shown at the trailing edge at which point the shock structure is fully evolved.

The invisicd and viscous solvers both predict the flow features associated with the shock formation accurately. The absense of the boundary layer for the invisicd solver produces a higher surface pressure as the reflected wave is impinging directly on the surface when compared to the inclusion of the boundary layer in which the reflected wave impinges on the boundary layer. As the height above the surface increases, a greater reduction in pressure is seen for the inviscid solutions i.e. the effect of including a boundary layer results in a lower variation in pressure above the surface of the geometry.

Figure 7.21 plots the pressure variation against the distance along the wing semi span for both the viscous and inviscid solvers. The initial increase and decrease in the pressure values results from the flow within the supersonic sharp corner. The pressure values then subsequently plateau to the 2D pressures values along the wing semi span. The results indicate that the pressure variation between the viscous and inviscid solver is also dependant of the shock formation across the geometry.

Figure 7.21 shows that at the same distance above the surface (1mm) there is a pressure difference between the viscous and inviscid solutions. This is due to the fact that the shock structure is fully evolved at the trailing edge which results in a greater change in the boundary layer thickness for a fully developed reflected shock wave (the reflected shock wave impinges on the boundary layer). A fully developed shock structure results in a larger boundary layer thickness, hence the higher difference in pressure between the inviscid and viscous solvers. The effect of the larger boundary layer thickness results in a lesser reduction in pressure above the surface. The higher freestream Mach number (Mach 5.0) naturally produces a larger boundary layer thickness. This coupled with the formation of the shock structure generates an even greater thickness in the boundary layer resulting in the pressure values showing the greatest difference in pressure between the viscous and inviscid solvers for the Mach 5.0 simulations.

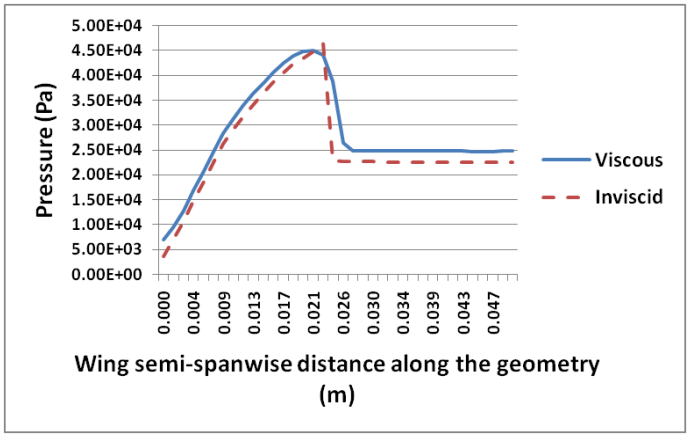

Mach 2.5

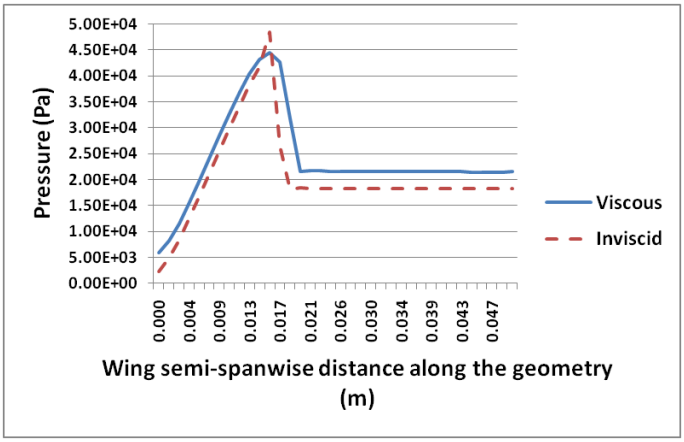

Mach 3.0

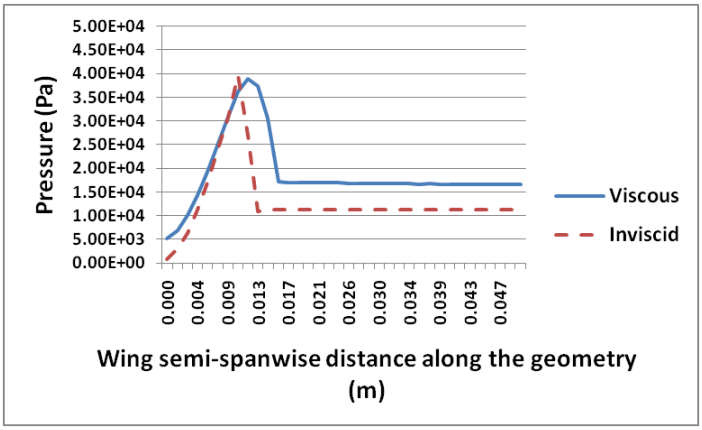

Mach 5.0

Figure 7. 21: Variation of pressure showing a comparison between the inviscid and viscous flow computations

8. Supersonic Experimental Images and Numerical Surface Streamlines, Results and Discussion

The oil film flow visualization technique was used as the preferred method of flow visualization. The experimental images for the 90 and 120 degree fillet and sharp corner geometries are presented. These experimental images are validated by plotting the surface streamlines obtained from the numerical analysis. The nature of the interaction between the oblique shock wave and the supersonic geometry results in the reflected wave impinging on the surface. The use of the oil film flow visualization technique enables the path of the reflected waves to be accurately predicted. The comparison between the experimental images and the surface streamlines are shown in Figures 8.1 to 8.4 for the 90 and 120 degree fillet and sharp corner geometries respectively. Isometric views of the entire geometry are shown for the surface streamlines. Both the experimental images and numerical surface streamlines are shown for the experiments and numerical simulations that were conducted at Mach 3.0. The important flow features are identified on each experimental and numerical image.

The experimental image for the 90 degree sharp corner geometry validates the formation of the shock structure shown in Section 7.1. Figure 8.1 shows the experimental and surface streamline images for this geometry. The path of the reflected wave is seen to start at the leading edge of the test specimen which indicates that both the formation of the shock structure and Mach reflections occur at the leading edge of the geometry. This is also seen on the surface streamlines. The reflected waves are identified by the dark regions on the images.

The experimental image for the 90 degree fillet geometry further validates the premise that there is a delay in the formation of the shock structure for geometries that include a fillet profile (Section 7.1) between two aerodynamic surfaces. The reflected wave which results from the formation of the Mach reflection is seen to occur at approximately 50 percent chord on the experimental image. Before this point the oblique shock wave is a smooth curved wave. This effect is also seen on the surface streamlines in Figure 8.2.

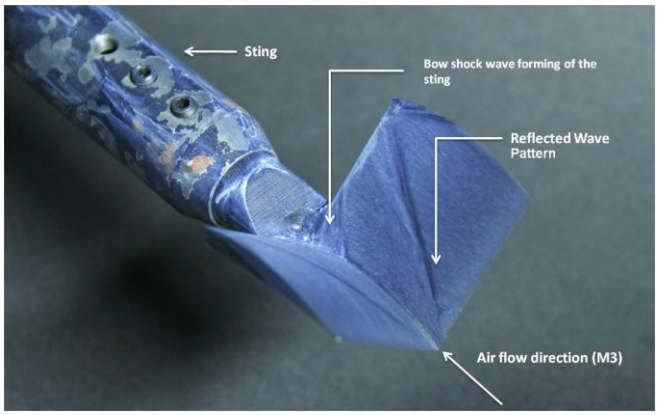

(a)

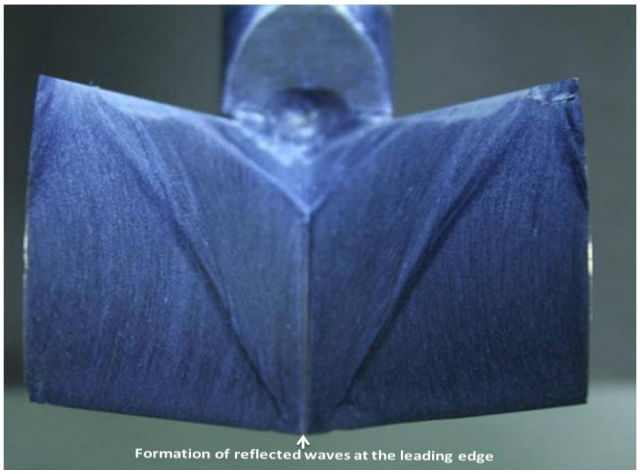

(b)

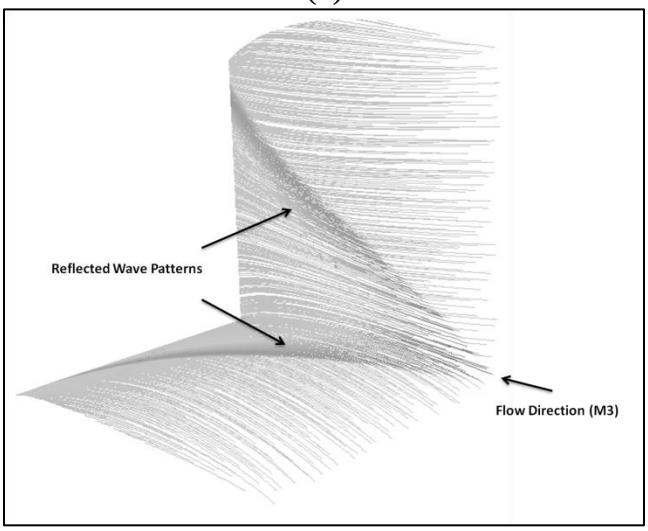

(c)

Figure 8. 1: Experimental and surface streamlines for the 90° sharp corner geometry at M 3.0, (a) Experimental isometric view (b) Experimental top view (c) Isometric view of the surface streamlines

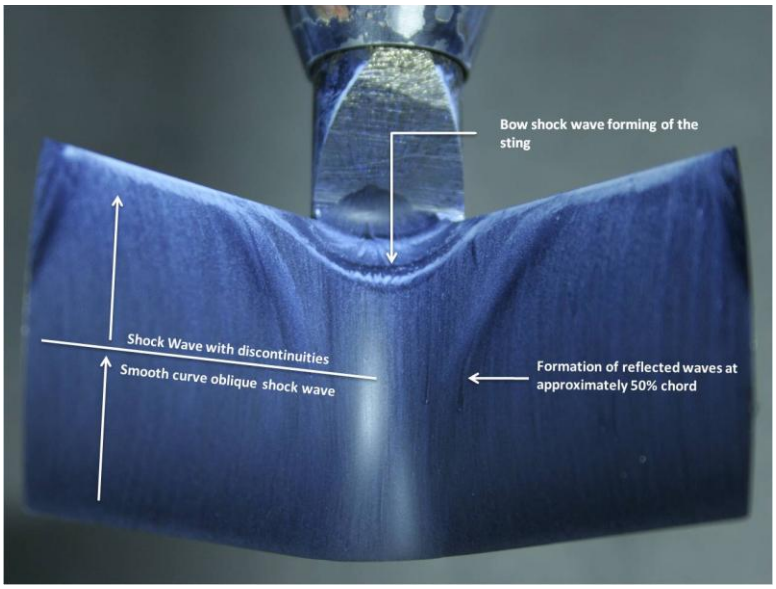

(a)

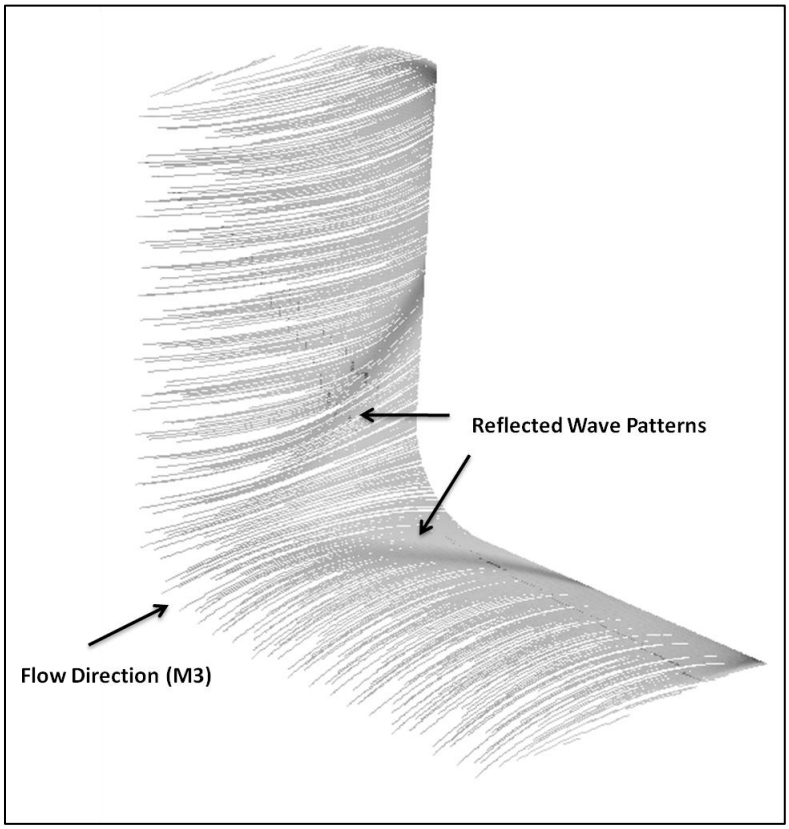

(b)

Figure 8. 2: Experimental and surface streamlines for the 90° fillet geometry at M 3.0, (a) Experimental top view (b) Isometric view of the surface streamlines

Figures 8.3 and 8.4 show the experimental and numerical surface streamline images for the 120 degree fillet and sharp corner geometries. Similar to the 90 degree fillet geometry, there is a delay in the formation of the Mach reflection for the 120 degree fillet case. However the transition from a smooth curved wave to a wave with discontinuities in slope occurs closer to the leading edge of the test specimen for the 120 degree case. This early transition is due to the larger dihedral angle. The surface streamlines shown in Figure 8.3 also shows that the formation of the Mach reflection occurs closer to the leading edge of the geometry when compared to the 90 degree fillet geometry.

Figure 8.4 shows that the formation of the reflected waves occurs at the leading edge of the 120 degree sharp corner geometry similar to that seen for the 90 degree sharp corner geometry. The surface streamlines validate the formation of the reflected waves at the leading edge.

Figures 8.1 to 8.4 all show a bow shock wave that forms near the trailing edge of the test pieces. This bow shock wave formation is a result of the support sting that holds the test piece in place during the experimental testing. This shock wave does not influence the formation of the reflected waves.

The results produced from the experimental and numerical investigations both show the respective formations and developments of the shock structures on the various supersonic geometries that were analyzed. The experimental and numerical comparisons shown in Figures 8.1 to 8.4 are seen to validate one another. The formation of the Mach reflection occurs at the leading edge of the sharp corner geometries and the fillet profiles delay this formation.

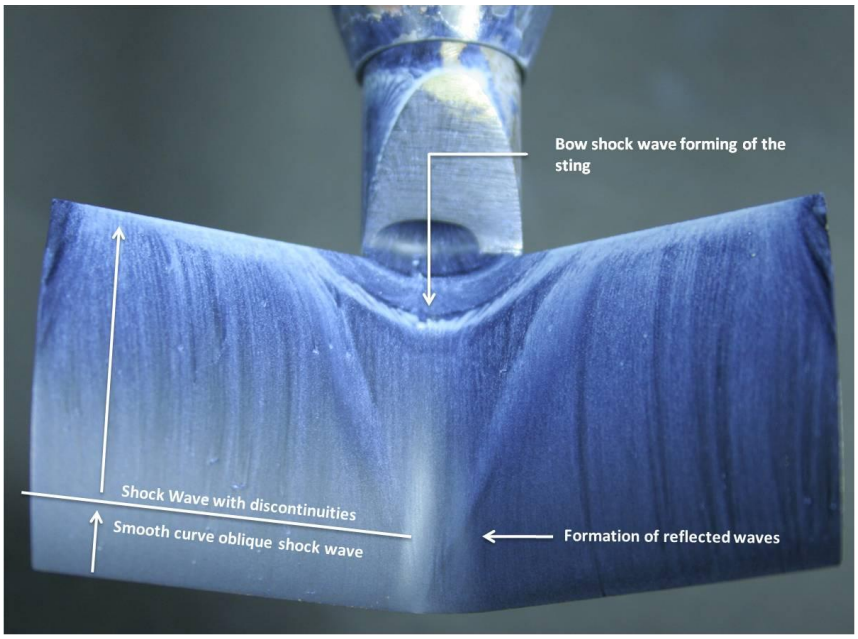

(a)

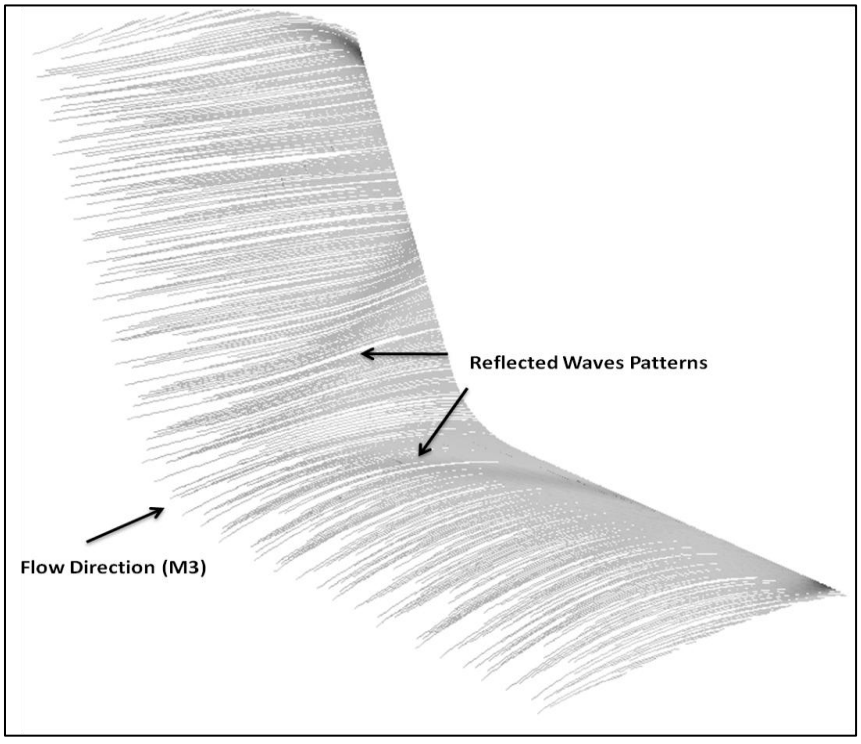

(b)

Figure 8. 3: Experimental and surface streamlines for the 120° fillet geometry at M3.0, (a) Experimental top view (b) Isometric view of the surface streamlines

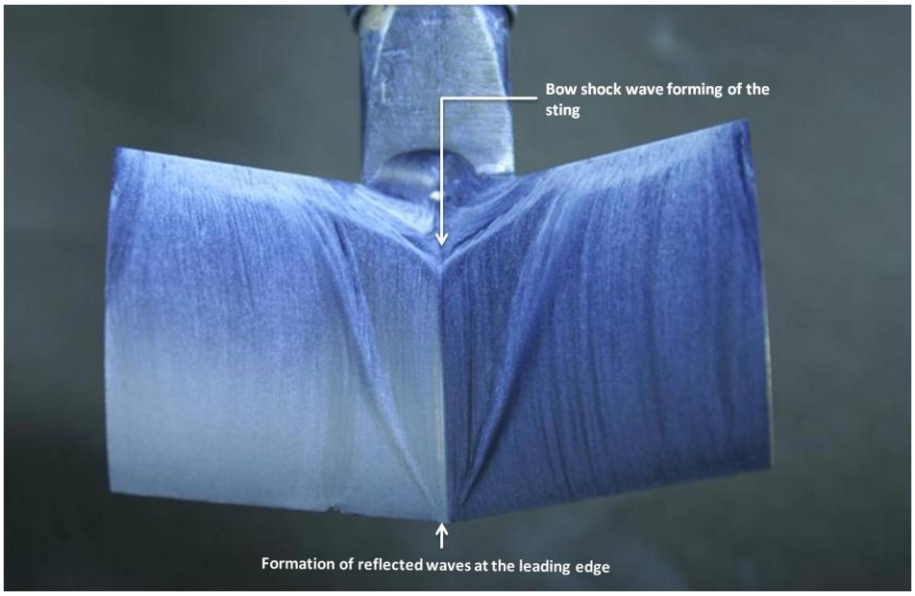

(a)

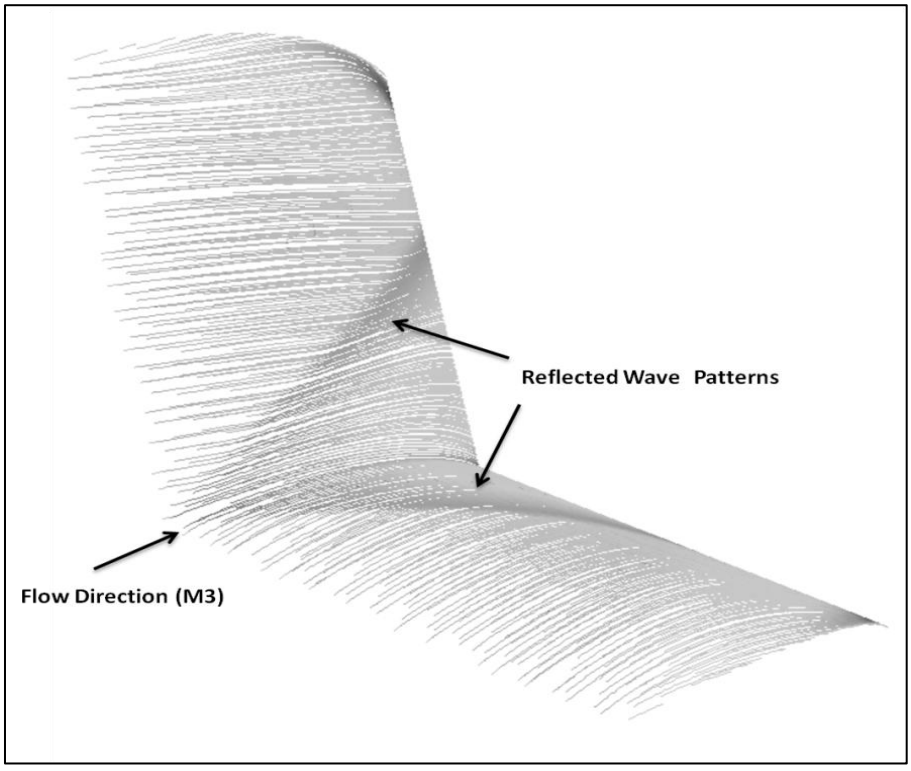

(b)

Figure 8. 4: Experimental and surface streamlines for the 120° sharp corner geometry at M 3.0, (a) Experimental top view (b) Isometric view of the surface streamlines

9. Transonic Numerical Results and Discussion

Minimizing the transonic shock wave formation or the impact of transonic shock waves on wing profiles is an important aspect of transonic airfoil design. The interaction of the shock wave and the boundary layer may cause boundary layer separation and regions of reversed flow. Major aircraft design companies such as Boeing and Airbus have in recent times employed the use of winglets/wingtips to improve the range and performance of their respective aircraft. The intersection of these winglets/wingtips with the main wing forms a corner similar to that seen in the supersonic flow research. Air flow through these corners will be at transonic Mach numbers resulting in these corners being referred to as "transonic corners". The following section presents the numerical results obtained for the preliminary research undertaken into transonic corner flows.

The formation of the transonic shock wave will be dependent on the airfoil geometry and/or corner profile. This research investigation utilized two airfoils and the results obtained are unique to these airfoils geometries. However, the results presented are an insight into the flow field within a transonic corner i.e. the basic flow physics within a transonic corner is established. A review of Section 6.3 will confirm that a total of 32 numerical simulations were conducted. These simulations had varying geometric parameters and freestream Mach numbers.

The following sets of results along with the respective discussions are presented for both the Rae 2822 the Onera M6 airfoil geometries:

- General formation of the transonic shock wave within a corner configuration. This formation will be established by;
    - Surface pressure contours showing regions of high and low pressure on the upper surface of the geometry;
    - Mach number contours taken along the symmetry plane; and
- Numerical surface streamlines and vector plots

Due to the lack of available transonic experimental facilities at the University of the Witwatersrand and the limited published data on transonic corner flows [20], a purely computational analysis was conducted for the research into transonic corner flows. The validity of these numerical results is inferred due to the agreement obtained in the numerical and experimental study of supersonic corner flows.

9.1 General formation of the transonic shock wave within a corner configuration

9.1.1 Rae 2822

The numerical results produced for the study of transonic corner flows all verify the existence of the transonic shock wave in a corner formed by two aerodynamic surfaces for the Rae 2822 airfoil geometries. This formation of the transonic shock wave is not dependant on the corner profile i.e. fillet or sharp corner or the wing profile i.e. straight or swept wing. The formation of the transonic shock wave is evident irrespective of the simulated freestream Mach numbers (M 0.75 to M 0.9) or geometric parameters utilized in the numerical simulations. The strength of the transonic shock wave and the resultant shock wave boundary layer interaction is however dependent on the corner and wing profiles.

The formation of the transonic shock wave is established by producing surface pressure and Mach number contour plots. The surface pressure contour plots are contour plots of the upper surface of the respective geometries. The contour plots of Mach number are taken along the symmetry plane as the symmetry plane is the centre of the transonic corner. These contour plots show the important flow features associated with the shock formation along the transonic corner. These flow features include the transonic shock wave and the regions of separated and reversed flow. The geometries were simulated with four different transonic Mach numbers. The results obtained for all the simulated Mach numbers are presented as it enables the progression and development of the transonic shock wave to be established with an increase in the freestream Mach number.

The surface pressure contours for the Rae 2822 geometries indicate that the shock formation is strongest in the transonic corner and decreases in strength as it moves outward toward the edge of the wing. The formation of the transonic shock wave also results in regions of reversed flow and separation. This is evident for all the geometries analyzed. Figures 9.1 to 9.4 show the surface pressure and Mach number contour plots for the Rae 2822 fillet and sharp corner straight wing geometries. The supersonic results (Section 7) showed that the sharp corner geometries produced a higher shock intenstiy when compared to the fillet profiles. A similar effect is seen for the transonic straight wing Rae 2822 geometries. The straight wing sharp corner surface pressure plots show a region of presure within the transonic corner that is lower when compared to the fillet profiles. This region of low pressure results in a stronger transonic shock wave which produces a stronger shock wave boundary layer interaction, hence a larger region of reversed and separated flow is seen for the sharp corner profiles.

The formation of the transonic shock wave results in the flow in the immediate vicinity of the shock, pushing outwards along a curved path toward the edge of the wing. This results in a *v-shaped* or *triangular shaped* region of reversed flow and separation along the corner. As the freestream Mach number increases the formation of the shock wave moves further aft along the respective corner profiles resulting in the area of the separated region decreasing in size. The triangular shaped separated region is still however evident.

The pressure distribution acrosss the surface of the geometry becomes more significant as the freestream Mach number increases. At the lower freestream Mach number (M 0.75), the pressure distribution is largely in the corner for both the fillet and sharp corner geometries.

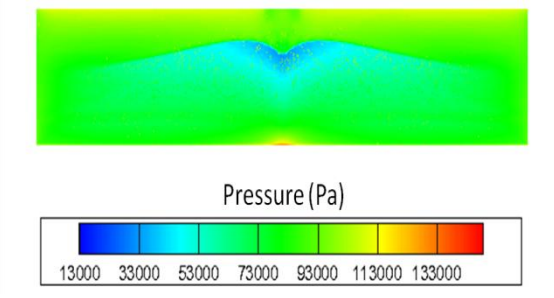

(a)

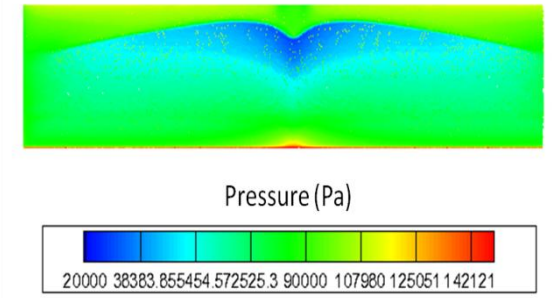

(b)

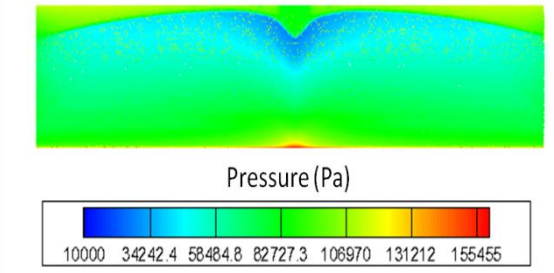

(c)

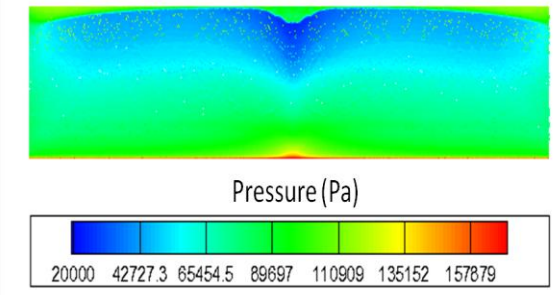

(d)

Figure 9. 1: Pressure contours for the Rae 2822 straight wing fillet geometries, (a) M 0.75, (b) M 0.80, (c) M 0.85, (d) M 0.90

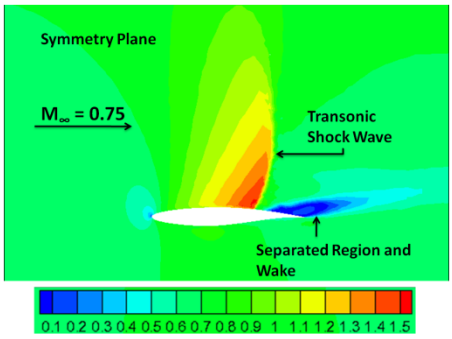

(a)

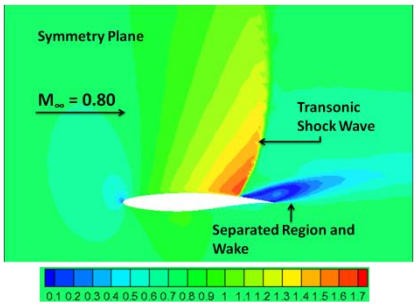

(b)

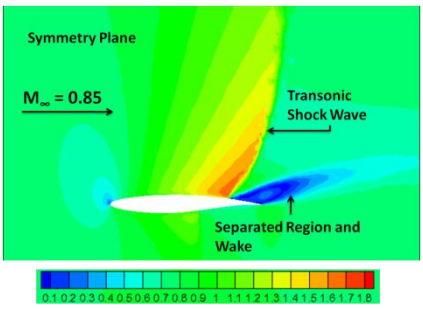

(c)

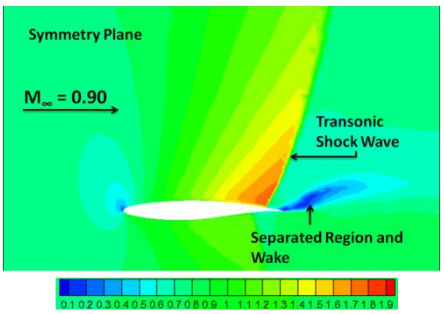

(d)

Figure 9. 2: Mach number contours taken along the symmetry plane for the Rae 2822 straight wing fillet geometries, (a) M 0.75, (b) M 0.80, (c) M 0.85, (d) M 0.90

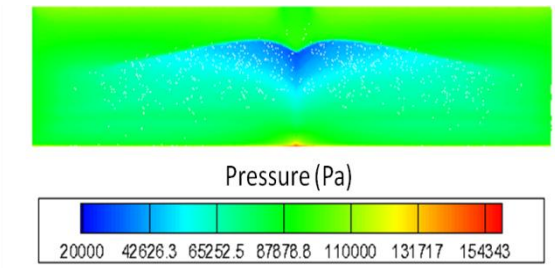

(a)

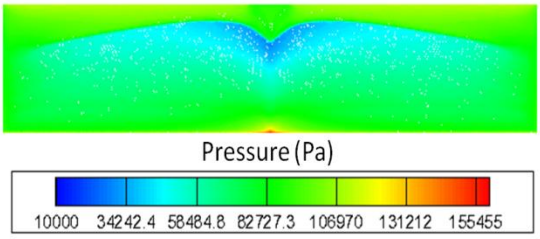

(b)

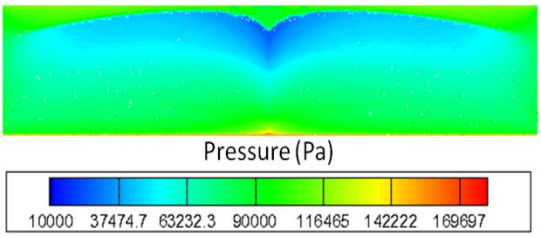

(c)

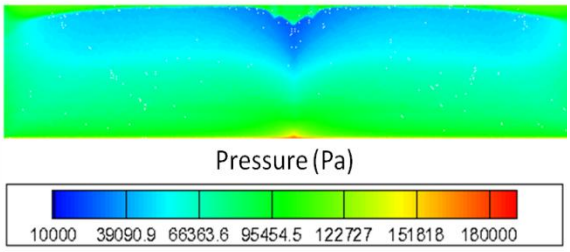

(d)

Figure 9. 3: Pressure contours for the Rae 2822 straight wing sharp corner geometries, (a) M 0.75, (b) M 0.80, (c) M 0.85, (d) M 0.90

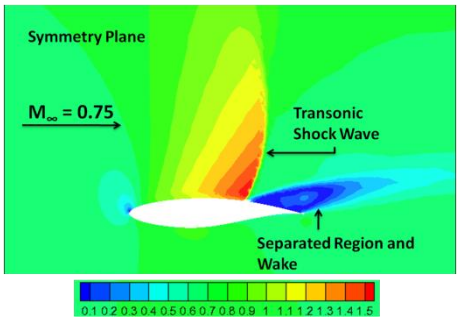

(a)

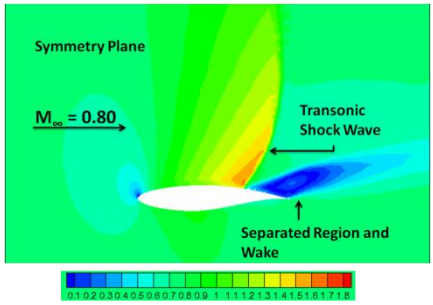

(b)

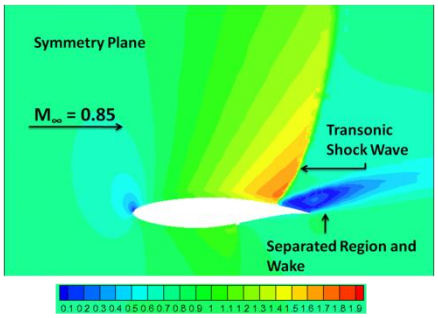

(c)

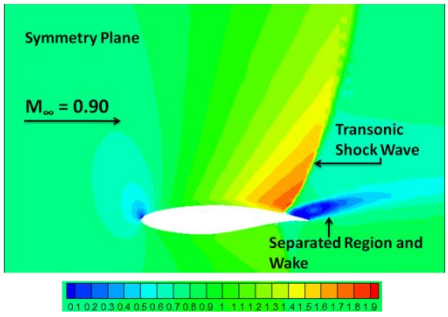

(d)

Figure 9. 4: Mach number contours taken along the symmetry plane for the Rae 2822 straight wing sharp corner geometries, (a) M 0.75, (b) M 0.80, (c) M 0.85, (d) M 0.90

The pressure contours for the Rae 2822 swept fillet geometries show the regions of low pressure within the transonic corner indicating the formation of the transonic shock wave within the swept fillet corner. The effect of the sweep angle and larger fillet radius results in the shock formation occuring further aft along the chord when compared to the swept sharp corner geometry i.e. the inclusion of the fillet profile and larger fillet radius results in formation of the transonic shock wave occuring further aft along the chord. Although the formation of the transonic shock wave is evident, the regions of reversed and separated flow is extremely small. The effect of the sweep angle and fillet radius results in a decrease in the shock intensity and resultant shock wave boundary layer interaction. The triangular shaped regions of flow separation and reversed flow are consequently not seen.

Similar to the straight wing geometries, the swept sharp corner geometry shows the formation of the transonic shock wave and the resultant triangular shaped separated region associated with the transonic corner. The pressure contours for the Rae 2822 swept sharp corner geometry shows that at the lower Mach number (M 0.75), the flow is not constrained to the transonic corner. Although the pressure within the corner is lower, the development of the shock wave over the swept geometry results in a low pressure distribution across the entire surface. This is not seen for the straight wing and swept fillet geometries where the low pressure regions are mainly evident in the transonic corner at M 0.75. The pressure and Mach number contours are shown in Figures 9.5 to 9.8 for both the fillet and sharp corner swept wing Rae 2822 geometries.

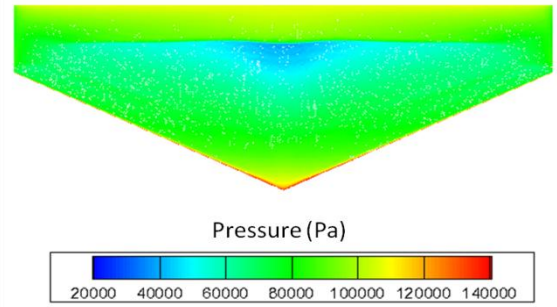

(a)

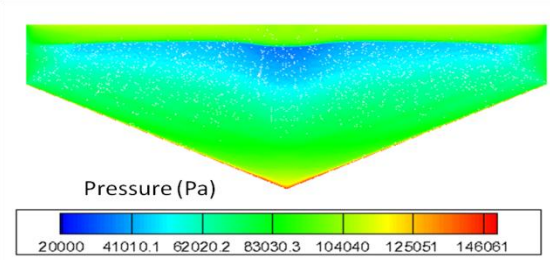

(b)

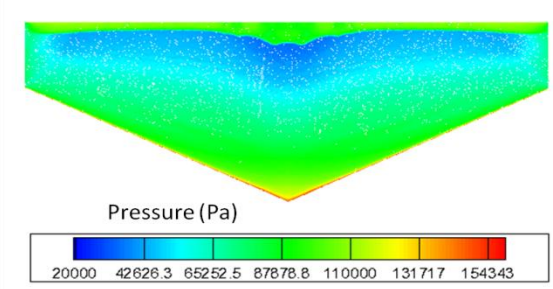

(c)

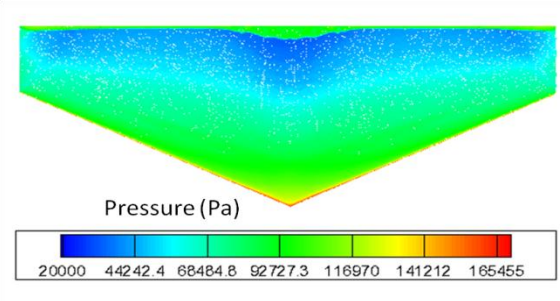

(d)

Figure 9. 5: Pressure contours for the Rae 2822 swept wing fillet geometries, (a) M 0.75, (b) M 0.80, (c) M 0.85, (d) M 0.90

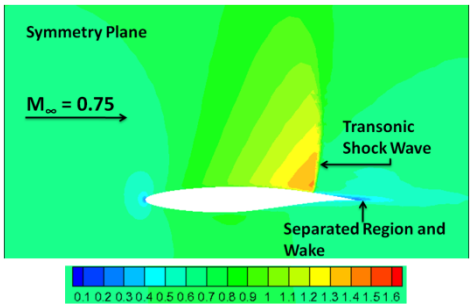

(a)

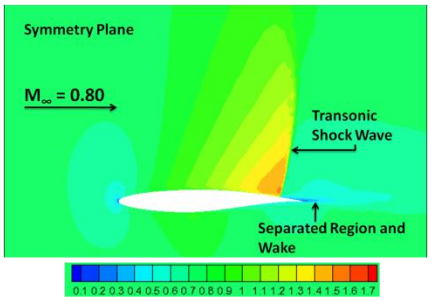

(b)

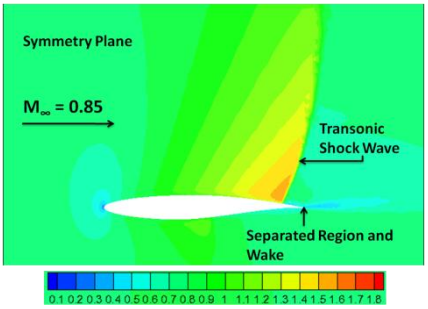

(c)

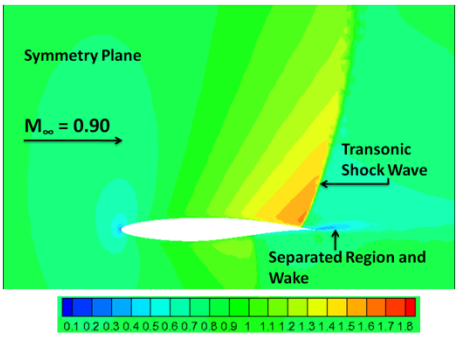

(d)

Figure 9. 6: Mach number contours taken along the symmetry plane for the Rae 2822 swept wing fillet geometries, (a) M 0.75, (b) M 0.80, (c) M 0.85, (d) M 0.90

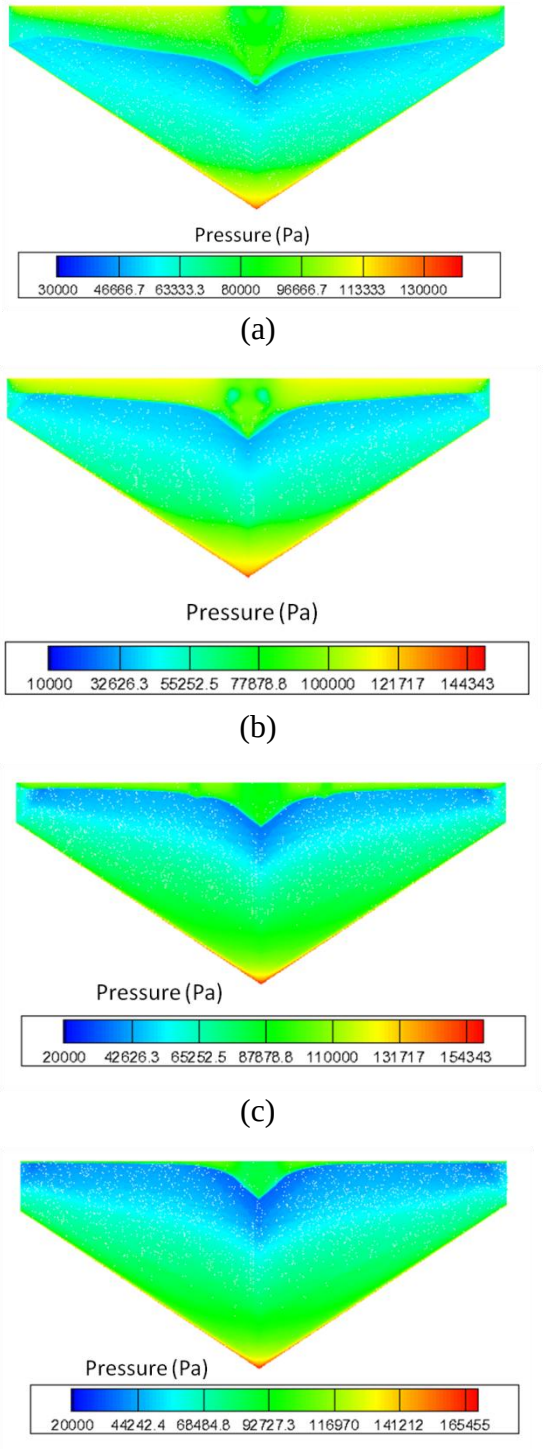

Figure 9. 7: Pressure contours for the Rae 2822 swept wing sharp corner geometries, (a) M 0.75, (b) M 0.80, (c) M 0.85, (d) M 0.90

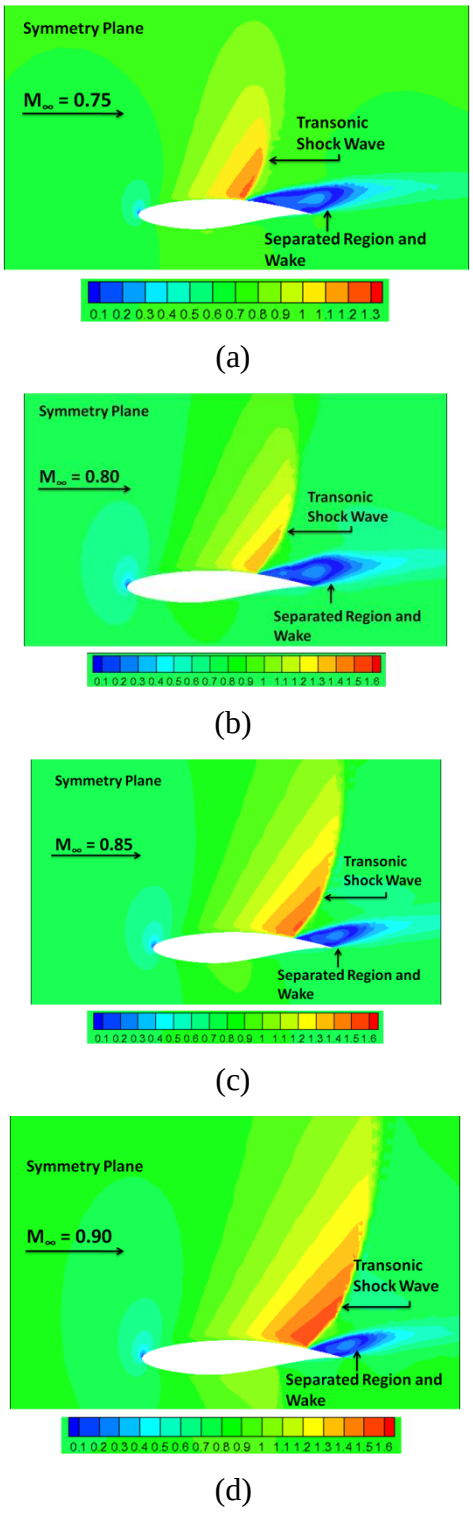

Figure 9. 8: Mach number contours taken along the symmetry plane for the Rae 2822 swept wing sharp corner geometries, (a) M 0.75, (b) M 0.80, (c) M 0.85, (d) M 0.9

9.1.2 Onera M6

The numerical results produced for the Onera M6 airfoil geometries all verify the existence of the transonic shock wave in a corner formed by two aerodynamic surfaces. The general flow features are similar to that established for the Rae 2822 airfoils i.e.:

- The formation of the transonic shock wave is not dependant on the corner or the wing profile;
- The formation of the transonic shock wave is evident irrespective of the simulated freestream Mach number (M 0.75 to M 0.9) or geometric parameters utilized in the numerical simulations;
- The formation of the transonic shock wave also results in regions of reversed flow and separation; and
- The strength of the transonic shock wave and the resultant shock wave boundary layer interaction is dependent on the corner and wing profiles.

The surface pressure and Mach number contour plots are shown in Figures 9.9 to 9.12 for the Onera M6 fillet and sharp corner straight wing geometries. The symmetric nature of the Onera M6 aifoil and the smaller thickness of the airfoil results in the flow over the Onera M6 geometries being slightly different from that established for the Rae 2822 geometries.

At Mach 0.75, the flow over the Onera M6 straight wing geometries produces considerably less separation when compared to the Rae 2822 geometries. A minimal amount of separation is seen for Onera M6 straight wing fillet geometry. At Mach 0.8, the formation of the transonic shock wave results in a larger region of reversed and separated flow which then decreases at Mach 0.85 and Mach 0.9 due to the formation of the transonic shock occurring further aft of the leading edge. The Onera M6 straight wing geometries also produce an edge effect. This edge effect is evident for the freestream Mach numbers $\geq$ M 0.80. This edge effect is coupled with the corner flow; however, the shock strength is still greatest in the corner.

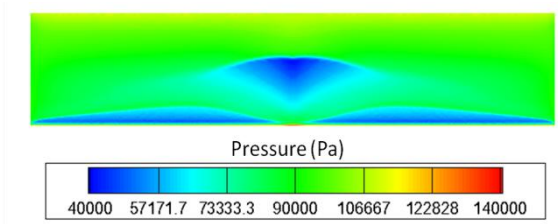

(a)

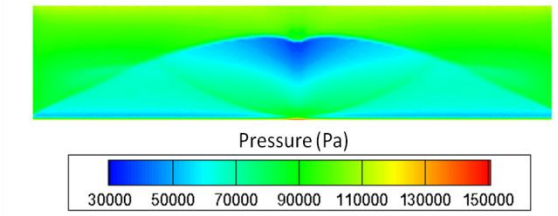

(b)

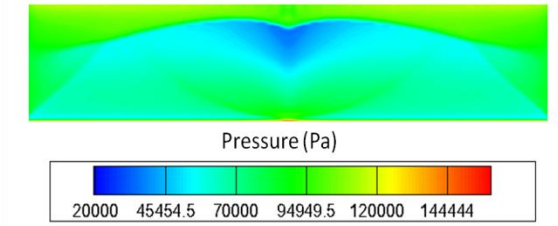

(c)

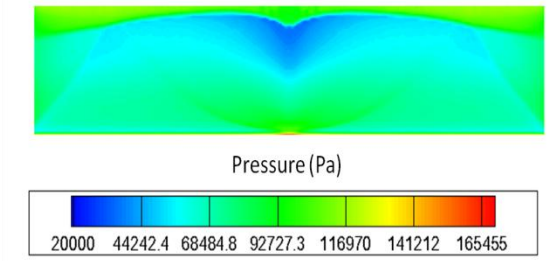

(d)

Figure 9. 9: Pressure contours for the Onera M6 straight wing fillet geometries, (a) M 0.75, (b) M 0.80, (c) M 0.85, (d) M 0.90

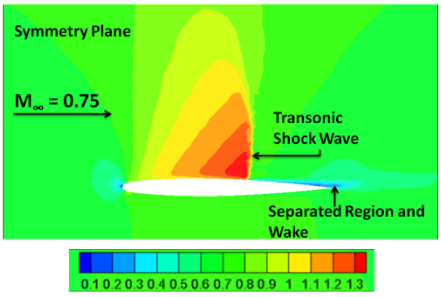

(a)

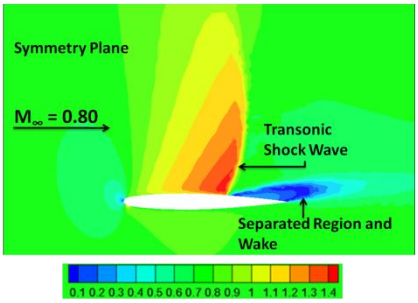

(b)

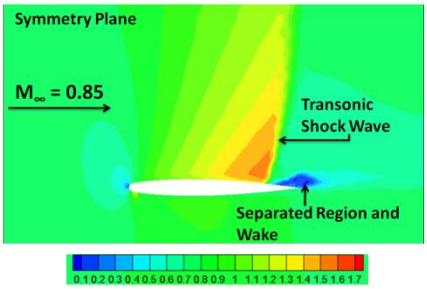

(c)

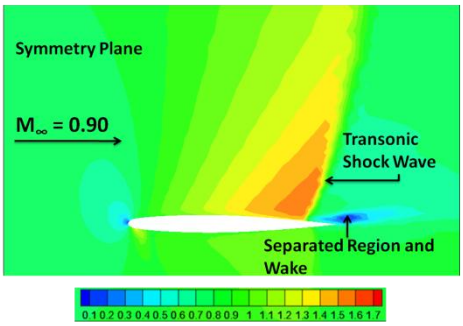

(d)

Figure 9. 10: Mach number contours taken along the symmetry plane for the Onera M6 straight wing fillet geometries, (a) M 0.75, (b) M 0.80, (c) M 0.85, (d) M 0.90

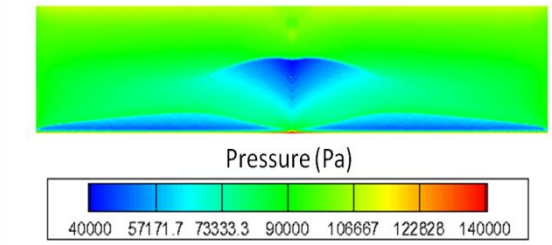

(a)

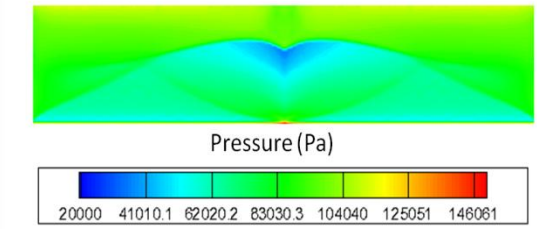

(b)

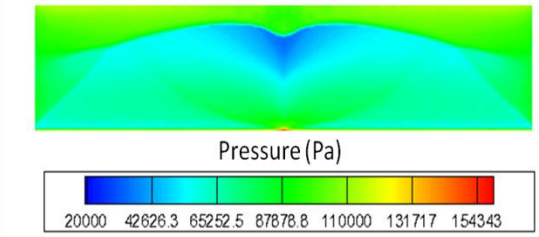

(c)

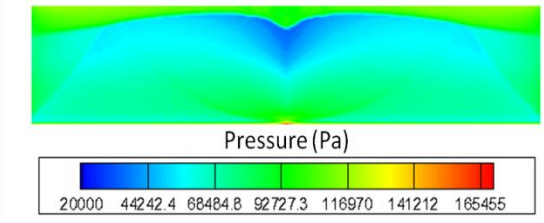

(d)

Figure 9. 11: Pressure contours for the Onera M6 straight wing sharp corner geometries, (a) M 0.75, (b) M 0.80, (c) M 0.85, (d) M 0.90

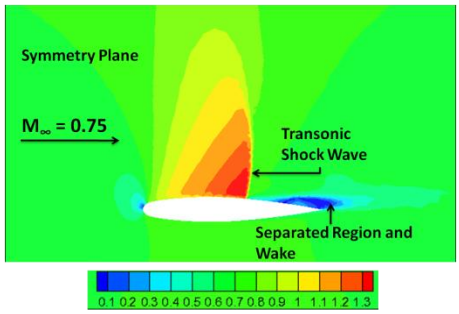

(a)

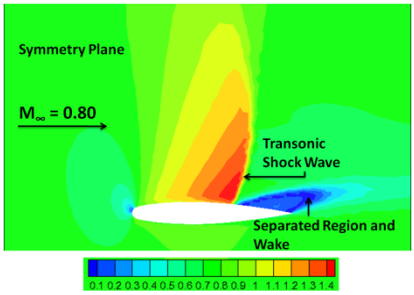

(b)

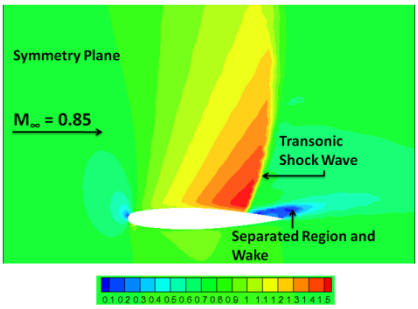

(c)

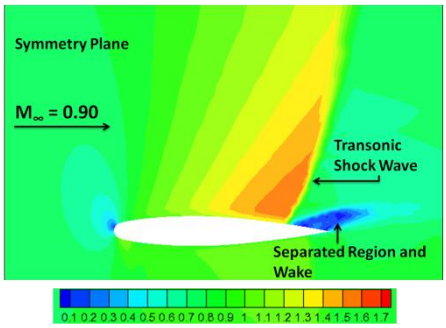

(d)

Figure 9. 12: Mach number contours taken along the symmetry plane for the Onera M6 straight wing sharp corner geometries, (a) M 0.75, (b) M 0.80, (c) M 0.85, (d) M 0.90

The flow over the Onera M6 straight wing fillet geometry resulted in minimal separation. The inclusion of sweep and a larger fillet radius further delays the onset of separation i.e. the inclusion of these geometric parameters results in a significanly lower shock intensity. For the straight wing surface the pressure distribution over the wing surface is governed by the velocity component in the chordwise direction. When the wing is swept, the chordwise velocity component becomes a function of the sweep angle which results in the velocity chordwise component being lower than that on a straight wing. Thus the effect of sweep results in a lower pressure distribution over the top of the wing. This results in a lower shock intensity and delays the onset of separation. The surface pressure contours also show that the region of low pressure within the transonic corner is considerably lower when compared to the Onera M6 straight wing geometries. The progression of the transonic shock wave is similar to that seen for the Rae 2822 airfoil geometries in that the formation of the transonic shock occurs further aft of the leading edge with an increase in the freestream Mach number.

The pressure distribution for the Onera M6 swept sharp corner geometries is confined to the corner at M 0.75. This was not seen for the Rae 2822 swept sharp corner geometries. The regions of reversed flow and separation is also considerably less than that of the Rae 2822 swept sharp corner geometries. This is due to the difference in thickness and shape of the Onera M6 airfoil when compared to the Rae 2822 airfoil.

The formation of the transonic shock within a corner formed by two aerodynamic surfaces has been established. This shock formation results in regions of reversed and separated flow. The shock intenstiy and the resultant shock wave boundary layer interaction is seen to be dependent on the corner and wing profile as well as the thickness and shape of the airfoil.

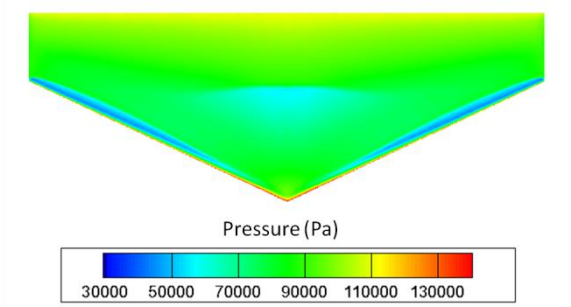

(a)

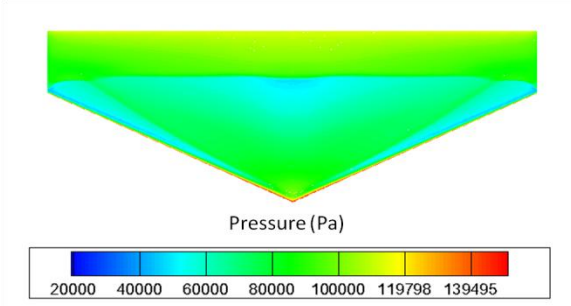

(b)

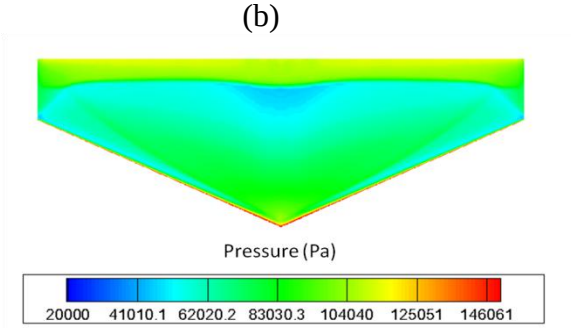

(c)

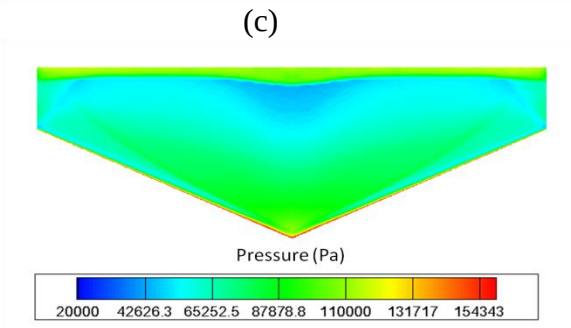

(d)

Figure 9. 13: Pressure contours for the Onera M6 swept wing fillet geometries, (a) M 0.75, (b) M 0.80, (c) M 0.85, (d) M 0.90

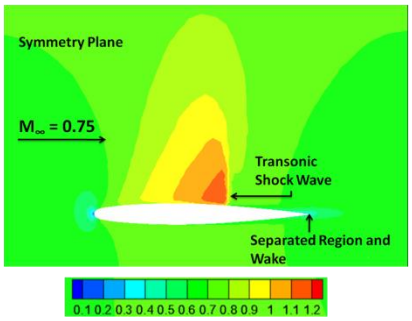

(a)

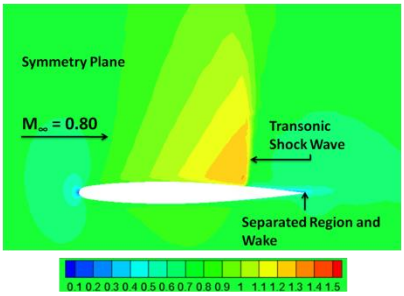

(b)

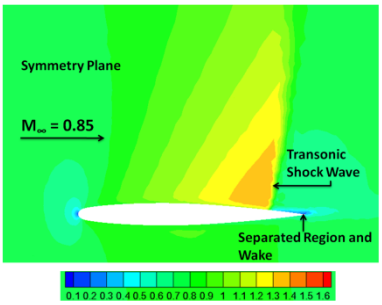

(c)

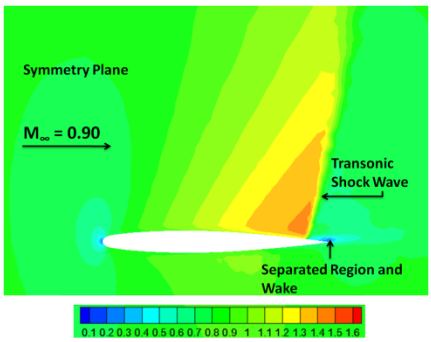

(d)

Figure 9. 14: Mach number contours taken along the symmetry plane for the Onera M6 swept wing fillet geometries, (a) M 0.75, (b) M 0.80, (c) M 0.85, (d) M 0.90

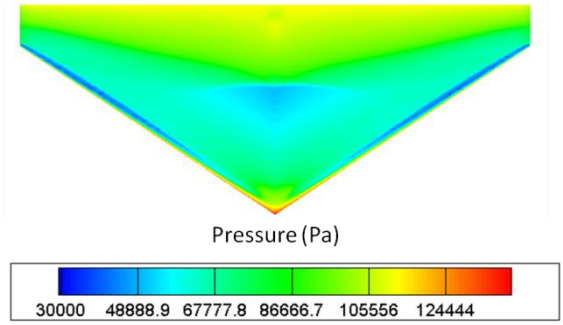

(a)

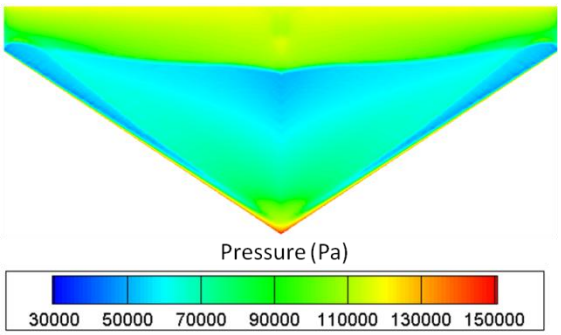

(b)

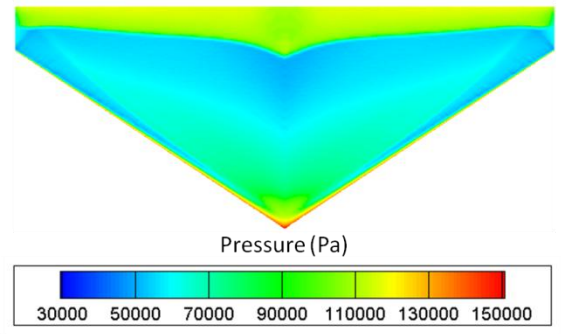

(c)

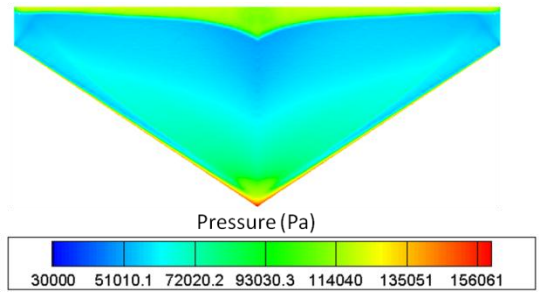

(d)

Figure 9. 15: Pressure contours for the Onera M6 swept wing sharp corner geometries, (a) M 0.75, (b) M 0.80, (c) M 0.85, (d) M 0.90

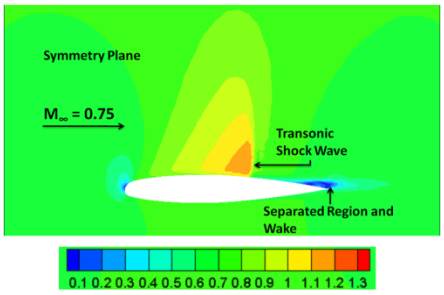

(a)

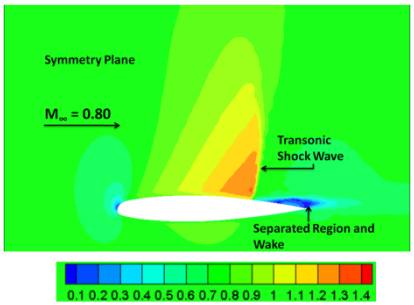

(b)

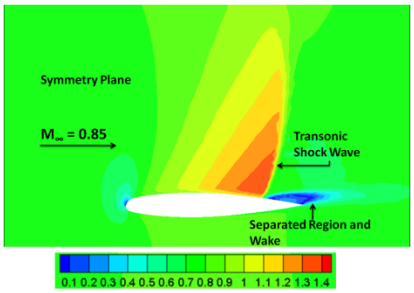

(c)

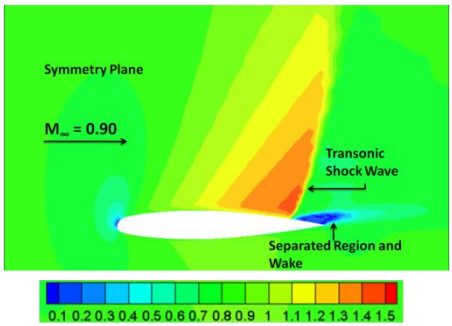

(d)

Figure 9. 16: Mach number contours taken along the symmetry plane for the Onera M6 swept wing sharp corner geometries, (a) M 0.75, (b) M 0.80, (c) M 0.85, (d) M 0.90

9.2 Numerical surface streamlines and vector plots

Section 9.1 confirmed the existence of the transonic shock wave within a corner configuration for both the Rae 2822 and the Onera M6 airfoils. The resultant shock wave boundary layer interaction generates regions of reversed and separated flow over all the simulated geometries. The numerical surface streamlines and vector plots in the current section indicate the changes in the flow direction across the surface of the geometry, specifically the changes in the flow direction related to the regions of reversed flow.

The flow features associated with the formation of the transonic shock wave is similar for both the Rae 2822 and the Onera M6 airfoil geometries. Although separation was established on all the geometries simulated, the surface streamlines and vector plots are shown for the flow over the Rae 2822 straight wing sharp corner geometry (M 0.75). The flow features established from the surface streamlines and vector plots are similar for the other transonic geometries.

Figure 9.17*a* illustrates the surface streamlines on the upper surface of the geometry. The streamlines show that the *v-shaped* or *triangular shaped* region of reversed flow and separation is restricted to the transonic corner. The path of the transonic shock wave along the wing span is also evident. Figure 9.17*b* shows the vector plot taken at the trailing edge of the geometry. The airflow within the separated region flows back up the surface of the geometry at the trailing edge, changes direction and flows away from the surface.

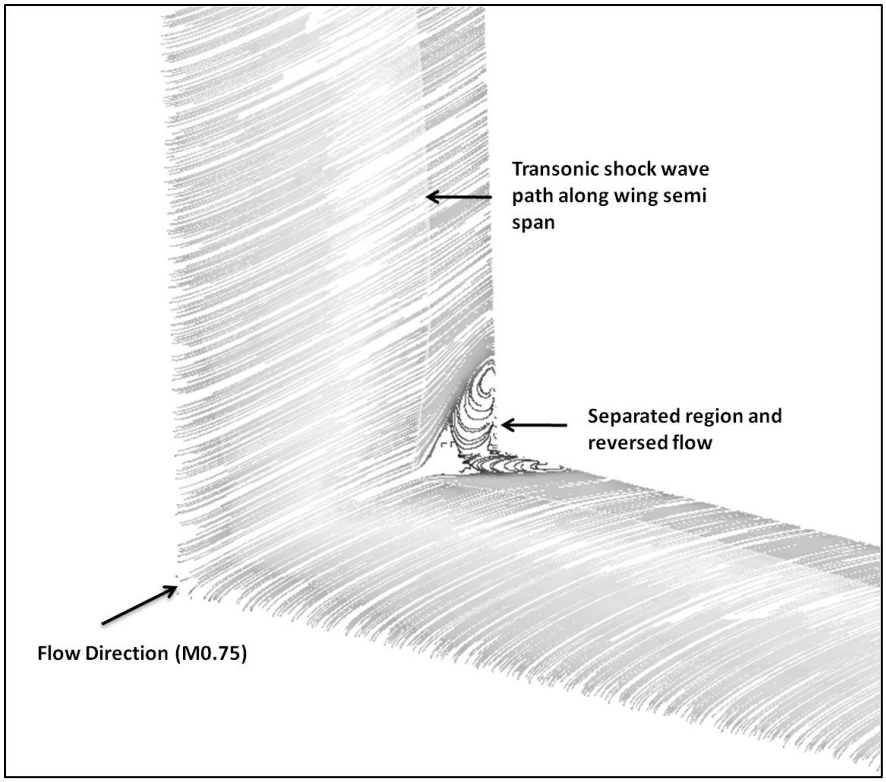

(a)

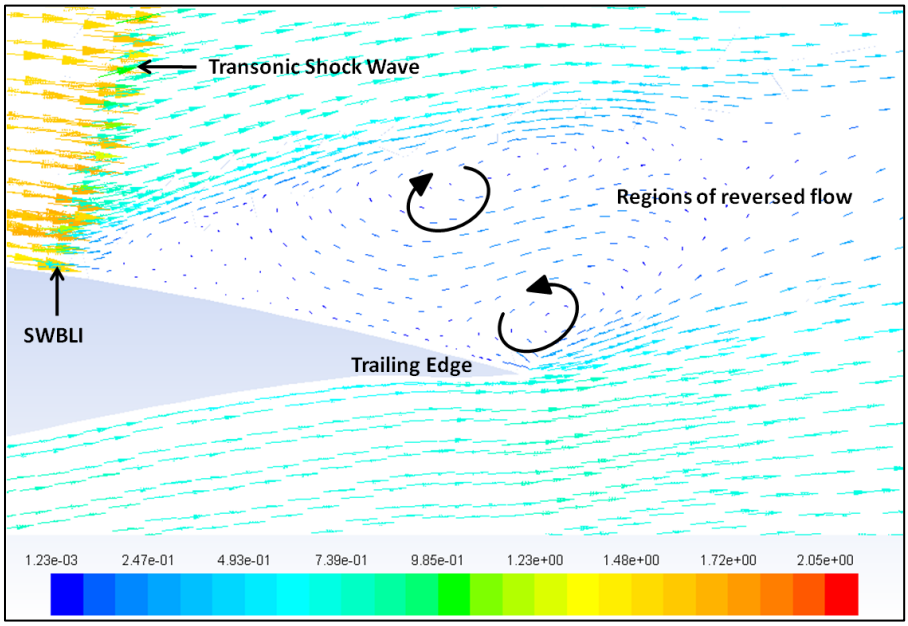

(b)

Figure 9. 17: Flow directions over the Rae 2822 airfoil, (a) Numerical surface streamlines, (b) Vector plot of Mach number

10. Conclusions

A numerical investigation of steady state supersonic and transonic viscous corner flows has been conducted. Geometries that resemble simplified wing body-fuselage intersections or other similar corner configurations that are found in supersonic and transonic aircraft were simulated using the numerical code of Fluent. These geometries varied in dihedral angle, camber profile, thickness/chord ratios and comprised of either a fillet or sharp corner profile. The conclusions for both the supersonic and transonic investigations are as follows:

Supersonic viscous corner flows

The numerical results produced confirm that the formation of the Mach reflection and shear layer are dependent on the geometric characteristics as well as the presence or absence of a fillet profile. The inclusion of a fillet profile results in the delay of the formation of the Mach reflection and shear layer. This also results in lower pressure and shear stress changes across the geometry. The pressure variation across the supersonic geometry is initially affected by the oblique incident shock wave but once transition has occurred, the impingement of the reflected shock wave on the surface of the geometry affects the surface pressure. Although the formation of the shear layer is evident for certain geometries, the shear layer effect on the surface pressure is negligible. Neglecting the effect of the fillet profile (sharp corner) resulted in the formation of the Mach reflection and shear layer starting at the leading edge of the geometry. A much higher pressure and shear stress variation is seen for the sharp corner geometries with the shear layer initially propagating onto the surface of the geometry. The impingement of the reflected shock waves on the boundary layer results in a large variation in the boundary layer thickness for the sharp corner geometries however no separation is observed. The experimental oil film technique validates the numerical results produced by accurately depicting the surface flow patterns.

Transonic viscous corner flows

The numerical results produced all confirm the existence of the transonic shock wave within a corner configuration for the simulated freestream Mach numbers (M 0.75 to M 0.90). The shock intenstiy and the resultant shock wave boundary layer interaction is seen to be dependent on the corner and wing profile as well as the thickness and shape of the airfoil. An increase in the freestream transonic Mach number results in the transonic shock wave moving further aft along the geometry. The transonic shock wave is strongest in the corner and decreases in strength along the wing. The flow over the sharp corner geometries results in a much higher Mach number and stronger SWBLI when compared to the flow over the fillet geometries. The shock wave boundary layer interactions produce regions of reversed and separated flow within the transonic corner.

11. Recommendations

In the event that any future research is conducted on the topic of supersonic and transonic viscous corner flow interactions, the following recommendations are made:

Supersonic viscous corner flows

- Explore the effect of sweep angle on the formation of the shock wave;
- Vary the point of maximum thickness for the circular arc cambered profiles and explore how this change affects the formation of the shock wave; and
- Experimentally verify the cross sectional shock wave profile.

Transonic viscous corner flows

- Experimentally verify the existence of the transonic shock wave within a corner configuration;
- Explore the effect of varying the fillet radii and sweep angles on the formation of the transonic shock wave.

12. References

1. ZEL'DOVICH Yu B. 1953. *Theory of Shock Waves and Gas Dynamics*. [Online] Volume No. AD0669272. Available from: www.dtic.mil/cgibin/GetTRDoc. AD0669272 [Accessed March 2009]
2. SKEWS B.W. 2007.University of the Witwatersrand. Gas Dynamics course notes.
3. BEN DOR G. 1992. Shock Wave Reflection Phenomena, New York: Springer - Verlag
4. WIDEMANN J.K, BROWN J.L, MILE J.B, OZCAN D. 1994. *Surface documentation of a supersonic boundary layer*. [Online]. Report No: NASA-CR-196788. Available from: www.archive.org/details/nasa_techdoc_19950004088 [Accessed March 2009]
5. ANDERSON J.D. 2007. Fundamentals of Aerodynamics. Fourth Edition. McGraw Hill International Edition
6. CHARWAT A.F, REDEKOPP L.G, 1967. *Supersonic Interference Flow along the Corner of Intersecting Wedges*. AIAA Journal 5. Pg 480-488
7. WATSON R.D, WEINSTEIN L.M. 1971. *A Study of Hypersonic Corner Flow Interactions*. AIAA Journal 9. pg 1280-1286
8. WEST J.E, KORKEGI R.H. 1972. *Supersonic Interaction in the Corner of Intersecting Wedges at High Reynolds Numbers*. AIAA Journal 10. pg 652-656
9. KORKEGI R.H. 1971. *Survey of Viscous Interactions Associated with High Mach Number Flight*. AIAA Journal 9. pg 771-784
10. KUTLER P. 1974. *Supersonic Flow in the Corner Formed by Two Intersecting Wedges*. AIAA Journal 5. pg 577-578
11. SHANKAR V, ANDERSON D, KUTLER P. 1975. *Numerical Solutions for Supersonic Corner Flow*, Journal of Computational Physics 17. pg 160-180
12. MARCONI F. 1980. *Supersonic Inviscid Conical Corner Flow Fields*. AIAA Journal 18. pg 78-84
13. MARSILIO R. 1993. *Vortical Solutions in Supersonic Corners*, AIAA Journal 9. pg 1651-1658

14. MARTIN J.A. 1985. *Shock Fitting Solution of the Supersonic Flow Field in a Rounded Internal Corner*. AIAA Journal 2. pg 193-200
15. SKEWS B.W, MILLS J.G, QUINN P, MENON N, MOHAN J. A. 2005. *Supersonic Corner Flow with Fillets, Camber, Sweep and Dihedral*. International Symposium on Shock Waves 25. Bangalore
16. GOONKO Yu P, KUDRYAVSTEV A.N, RAKNIMOV R.D. 2004. *Supersonic Inviscid Corner Flows with Regular and Irregular Shock Interaction*, Journal of Fluid Dynamics. Volume 39. No.2. pg 304-318
17. SHANG J.S, HANKEY W.L, PETTY J.S. 1979. *Three Dimensional Supersonic Interacting Turbulent Flow along a Corner*. AIAA Journal 17. pg 706-713
18. SETTLES G.S, PERKINS J.J, BOGDONOFF S.M. 1980. *Investigation of Three Dimensional Shock/Boundary Layer Interactions at Swept Compression Corners*. AIAA Journal 18. pg 779-785
19. SETTLES G.S, TANG H.Y. 1982. *Flow Visualization Methods for Separated Three Dimensional Shock Wave/Turbulent Boundary Layer Interactions*. AIAA Journal 21. pg 390-396
20. GRENON R, MEHEUT M, CARRIER G, DEFOS M, DUFFAU M. 2009. [online] *Aerodynamic Design of Flying Wing Configurations*. CEAS/KATnetII Conference on Key Aerodynamic Technologies. Bremen. Germany. 2009. Available from: www.onera.publications.fr/exl-doc/DOC376792_s1 [Accessed December 2012]
21. COOK P.H, MCDONALD M.A, FIIRMIN M.C.P. 1979. *Aerofoil Rae 2822 Pressure Distributions, Boundary Layer and Wake Measurements*. Experimental Database for computer program assessment, Report of the Fluid Dynamics Panel Working Group 04. AGARD Report 138.
22. Fluent 6.3 User and Tutorial Guides. 2008. Validation 12: *Transonic flow over an RAE 2822 airfoil*. Section 12: pg 1-6
23. SCHMITT V, CHARPIN F. 1979. *Pressure Distribution on the Onera M6 Wing at Transonic Mach Numbers*. Experimental Database for computer program assessment, Report of the Fluid Dynamics Panel Working Group 04, AGARD Report 138.

24. MERZKICH W. 1987. Flow Visualization. 2nd Edition. Orlando Academic Press
25. SQUIRE. L.C. *The Motion of a Thin Oil Sheet Under the Boundary Layer of a Body*, AGARD Report AG 70, pg 7 -26
26. MENON N. 2004. *Visualization of Three Dimensional Compressible Flow Fields*, MSc. Dissertation. University of the Witwatersrand. Johannesburg, South Africa.
27. MOWATT S. 2011. *Three Dimensional Shock Wave Boundary Layer Interaction*, MSc. Dissertation, University of Witwatersrand. Johannesburg. South Africa

Appendix A Supersonic Wind Tunnel Components

The following section contains the descriptions, technical specifications and images of the experimental apparatus.

The experimental apparatus includes the:

- Test Section;
- Compressor;
- Storage Vessel;
- Dryer;
- Tunnel Pressure Control;
- First and Second Throat; and
- Settling Chamber

The experimental procedure and precautions can also be found in this section.

Test Section

The test section has a maximum cross sectional area of 101.6mm X 101.6mm. Visualization of the experimental test specimens is obtained through optical glass situated on either side of the test section. Access to the test section is obtained by sliding the tunnel roof and walls after the test section backward. Figure A.1 is a photograph of the test section. The basic technical specifications of the wind tunnel are shown in Table A.1.

Table A. 1: Technical specifications of the supersonic wind tunnel

Manufacturer	Aerolab
Mach Number range	2.5 - 3.0
Test Section Dimensions	101.6mm X 101.6mm
Test Section Area	10322mm^2
Second Throat Area	9460mm^2
Maximum Blow down Time	+- 25 sec
Test Section Shut-Off Pressure	210 kPa
Maximum Operating Temperature	122° C

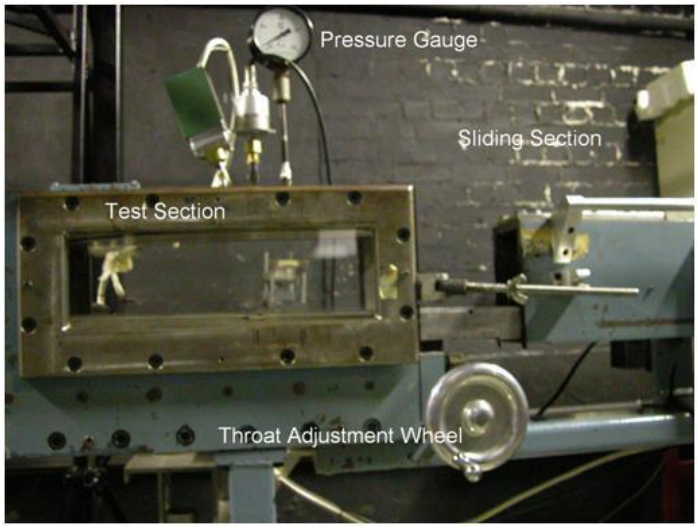

Figure A. 1: Wind tunnel test section

Compressor

The compressor that is used to pump up the storage vessel is a reciprocating compressor. It has an automatic shut down system. This shut down system is initiated once the storage vessel has been pressurized to a maximum pressure of 1.5 MPa. The automatic shut down is also initiated in the event that the oil level in the compressor drops below the acceptable limits or the water that cools the compressor is insufficient. The technical specifications of the compressor are shown in Table A.2. Figure A.2 is a photograph of the compressor.

Table A. 2: Technical specifications of the compressor

Manufacturer	Reavell and Co
Type	CSA 4, Reciprocating
Power	18.7 kW
Normal Operating Speed	960 rpm
Maximum Operating Speed	1000 rpm
Maximum Operating Delivery Pressure	1.5 Mpa
Maximum Design Delivery Pressure	3.1 Mpa



Figure A. 2: Reciprocating compressor

Storage Vessel

The storage vessel stores the air required for the experimental testing. It is pumped to a pressure of 1.5 MPa by the compressor. The technical specifications of the storage vessel are shown in Table A.3. Figure A.3 is a photograph of the storage vessel.

Table A. 3: Technical Specifications of storage vessel

Manufacturer	Kies and Traver Ltd
Storage Vessel Operating Pressure	1.5 Mpa
Design Operating Pressure	2.07 Mpa
Maximum Test Pressure	3.09 Mpa
Maximum Operating Temperature	122° C
Storage Vessel Volume	$9.04m^{3}$
Storage Vessel Length	5.7m
Storage Vessel Diameter	1.5m



Figure A. 3: Storage vessel

Dryer

The air from the compressor is not pumped directly into the storage vessel. It is passed through an air dryer element. This air dryer comprises of a pressure vessel which contains silica crystals. The function of the silica crystals is to absorb any water vapour that may be present in the air. The dryer also has a heater attached to it. The silica crystals become saturated after a certain period of use and need to be dried. The heater is used to dry the silica crystals and achieves this by passing hot air over them. Table A.4 shows the technical specifications of the dryer. Figure A.4 is a photograph of the dryer [26].

Table A. 4: Technical specifications of dryer

Manufacturer	Tegnon
Type	RB model
Pressure Vessel Manufacturer	Servex
Pressure Vessel Volume	$0.06m^3$
Operating Pressure	2.14 Mpa
Maximum Test Pressure	3.21 Mpa
Regeneration Time	12 hours

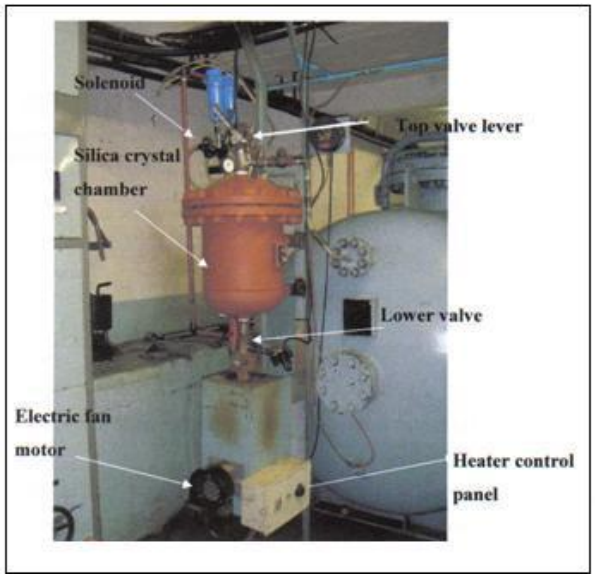

Figure A. 4: Air dryer

Settling Chamber

The air from the storage vessel is sent to the settling chamber. The settling chamber is located between the main control valve and the first throat. The function of the settling chamber is to remove any unwanted disturbances within the flow. It performs this function by making use of a flow distribution plate and three phosphor – bronze plates. The flow distribution plate is used to ensure that the flow is distributed evenly within the settling chamber. The phosphor – bronze plates ensures that any large disturbances present in the flow are removed before the flow enters the first throat. Figure A.5 is a schematic representation of the settling chamber and its internal workings. Figure A.6 is a photograph of the settling chamber.

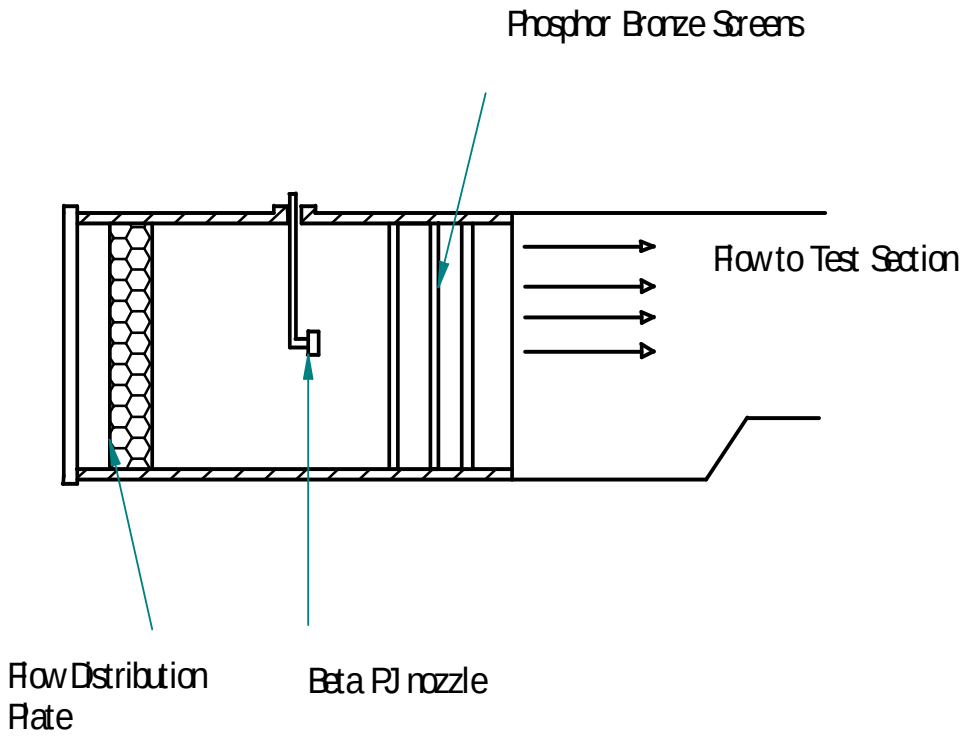

Figure A. 5: Schematic representation of the settling chamber.

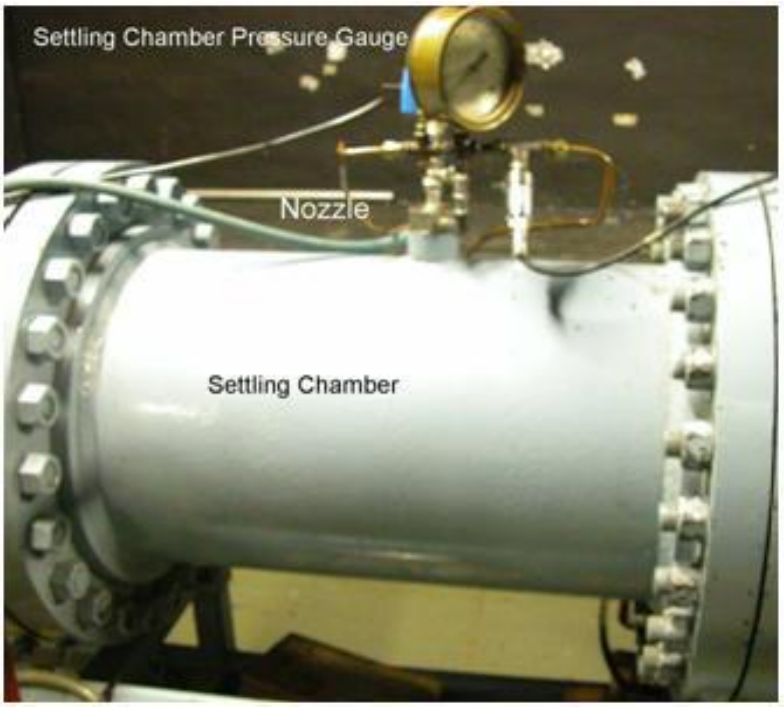

Figure A. 6: Settling chamber.

First and Second Throat

The supersonic wind tunnel has two throats. The first throat is situated between the settling chamber and the test section. The air from the settling chamber is accelerated through the first throat or converging – diverging nozzle. The area of this throat is adjusted in order to produce various Mach numbers required for experimental testing. The first throat comprises of an upper and lower block. The upper block is fixed and the lower block is able to move i.e. the movement of the lower block either opens or closes the throat. This is shown in Figure A.7. Movement of the lower block is obtained by adjusting the position of the throat adjustment wheel. The second throat is situated after the test section. As air passes through the test section, the second throat reduces the Mach number of the air before the air is vented out the building. The second throat is a small hump situated on the wind tunnel floor. This hump produces a decrease in cross section from the test section by 8.5%. As a result of this decrease in cross section, the Mach number of the flow through the test section is reduced to subsonic speeds for Mach numbers below 1.5. For the higher Mach numbers the conditions at the second throat

remain supersonic. The flow is then decelerated to subsonic conditions through a normal shock situated downstream of the second throat. Figure A.7 is a photograph of the first throat [26].

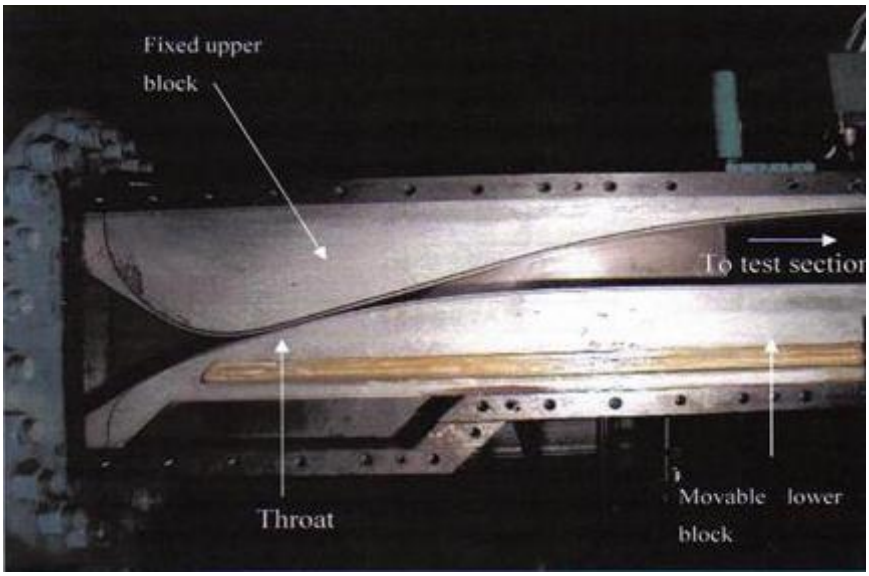

Figure A. 7: First throat

Tunnel Pressure Control

To maintain supersonic flow in the wind tunnel, a constant minimum stagnation pressure is required. During an experimental test run, the pressure in the wind tunnel must be kept above this minimum pressure. Large fluctuations of this pressure will have a direct effect on the Reynolds number; hence the Mach numbers through the tunnel will be affected. Therefore the tunnel pressure control system is used to ensure that the pressure remains constant. The pressure control system is also used as a safety mechanism. It cut-offs if the pressure in the test section becomes too high. This pressure control system is pneumatic and self regulating.

The essential operation of the supersonic wind tunnel is as follows:

The storage vessel is pumped up to a maximum pressure of 1.5 MPa using the reciprocating compressor. Air then passes from the storage vessel through the main control valve and into the settling chamber. The settling chamber stagnation pressure is set by the tunnel operator. The air expands as it passes through the first throat and into the test section. The area of the first throat determines the Mach number of the air in the test section. This area is set by the operator by adjusting the throat adjustment wheel until the desired setting is established. The calibration curve for the adjustment of the throat is shown in Figure A.8 [26]. The Mach number required for experimental tests is obtained by adjusting the throat adjustment wheel to the specified throat counter number.

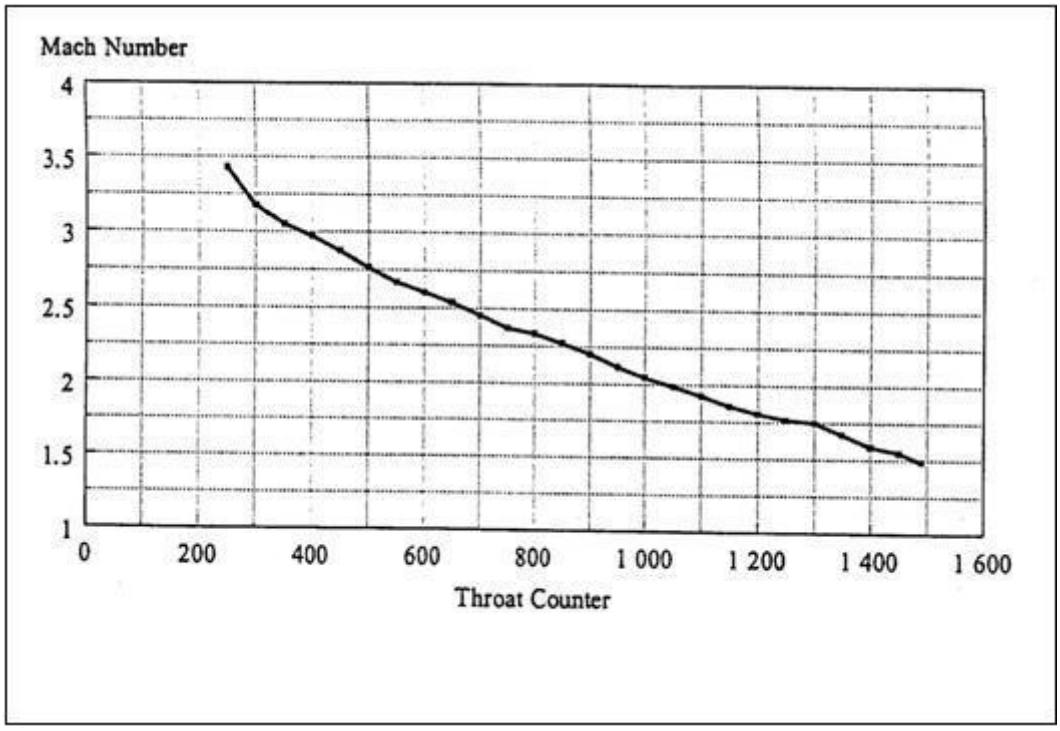

Figure A. 8: Calibration curve for the throat counter

Table A.5 describes the minimum stagnation pressure and throat counter values required to achieve the desired Mach numbers used during the experimental testing.

Table A. 5: Stagnation Pressure, Throat Counter and Mach numbers

Stagnation Pressure (Pa)	Throat Counter	Mach number
160 000	550	2.5
350 000	350	3.0
550 000	290	3.2

Mach and Reynolds number

The Mach and Reynolds numbers were plotted after a tunnel run to ensure that flow through the test section was at the required Mach number. These curves are shown in Figure A.9 for an experiment conducted at Mach 3 [27].

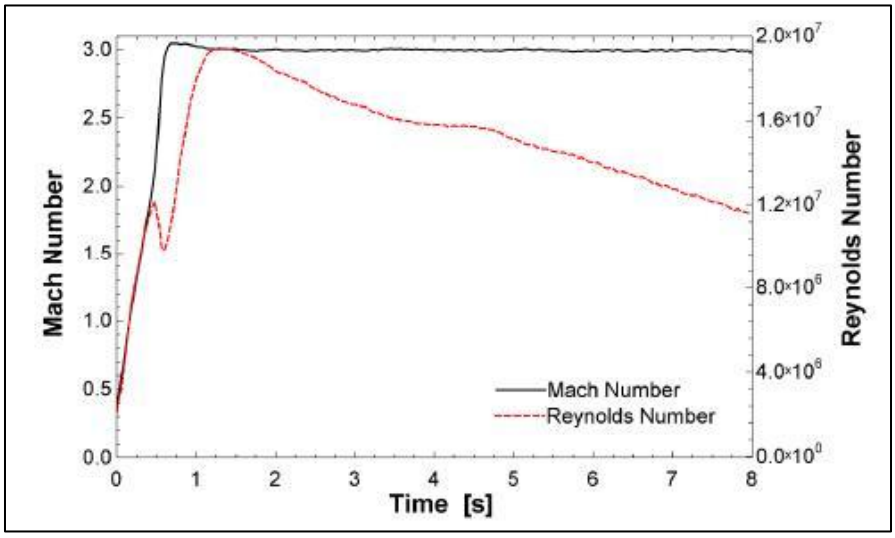

Figure A. 9: Mach and Reynolds number curves for a Mach 3.0 test run

Sting and Backing Plate

In order for the test pieces to be mounted in the wind tunnel, a sting and backing plate had to be designed. The backing plate is fixed onto the wind tunnel just after the test section and the sting enables the model to be fixed into it and the sting itself is fitted onto the backing plate.

Before the actual design of the sting and backing plate had begun it was discovered that a sting and backing plate had already been designed and built from previous year's research carried out in the supersonic wind tunnel. This sting and backing plate was ideal for experiments, as a result a new design was not required. The test pieces were fixed onto the sting using 6 5mm grub screws. Figure A.9 is a photograph of the sting and backing plate with the test piece fixed onto it.

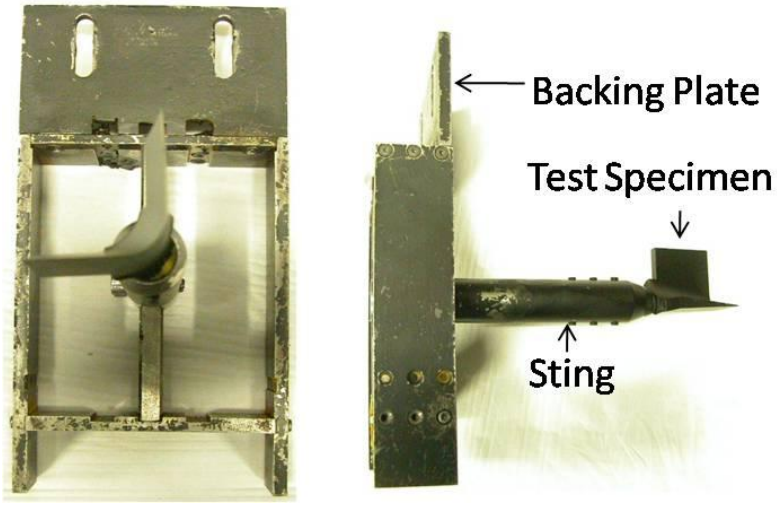

Figure A. 10: Experimental sting and backing plate

Experimental Procedure

The experimental procedure that was followed had to be performed on each day of testing. The components that were of primary importance were the compressor, storage vessel and the main component was the supersonic wind tunnel.

The following procedures were followed during a day of experimental testing.

Pumping up the Storage Vessel

- The two valves on the dryer had to be closed before turning on the compressor;
- The power to the compressor was switched on by turning on the switch located on side of the compressor main frame;
- The water supply to the compressor was initiated by rotating the valve counter-clockwise for one full revolution;
- The compressor is then started by rotating the red power button on the compressor main frame clockwise until it flicks out and the motor starts up;
- The compressor is then left to pump up the storage vessel to a maximum pressure of 1.5 MPa; after this is achieved the compressor shuts down automatically.

Turning the Compressor off

The compressor shuts down automatically after the storage vessel is fully pumped up. However if the compressor needed to be stopped at any time the following procedure was adopted:

- The compressor was turned off by depressing the red power button on the compressor;
- The water supply to the compressor was then closed;
- The power to the compressor main frame was then switched off.

- The upper valve on the dryer unit was then rotated to release any excess air present in the pressure vessel of the dryer unit;
- The heater was then switched on and allowed to run. The heater was switched on in order for the drying of the silica crystals to take place.

Once the pressure vessel was pumped to its maximum capacity and the compressor was shut down, the wind tunnel could then be used to perform the necessary experiments.

In order to ensure the effective operation of the wind tunnel the following procedures were followed during each experimental test.

Operation of the supersonic wind tunnel

Initial safety precautions were attended to and these included ensuring that the compressor was switched off, the water supply to the compressor was closed and that the upper and lower valves present on the dryer unit were open.

- The test piece is attached to the sting in the required orientation firmly by using 6 5mm grub screws;
- The sting and backing plate together with the test piece was then positioned in the wind tunnel and secured into place;
- The test section is then closed by moving the sliding section of the wind tunnel forward and locking it into place using the two wing nuts;
- The throat adjustment wheel is then adjusted to the desired setting that will enable the experimental tests to be performed at the specified Mach number;
- The tunnel control box, oscilloscope and computer were all turned on;
- The stagnation pressure in the settling chamber was set to the desired value;
- The pressure on the storage vessel is then checked and recorded;
- All the relevant experimental information was then recorded in the wind tunnel log book;

- The wind tunnel siren was then sounded notifying other people in the building of the test run;
- If no more tests are to be performed on a particular day, the settling chamber pressure is turned off;
- The tunnel was opened to allow the drying out of air in the test section

Experimental Precautions, Safety and Maintenance.

- The test section optical glass was always cleaned using acetone. This was done due to the fact that images are taken from outside the supersonic wind tunnel test section, therefore any dirt marks present on the glass will have an impact on the quality of the images;

- The test specimens and test section were always securely fastened and checked before any tests were performed;

- The siren was always sounded before any tests were performed to alert the other people in the building;

- Ear protection was worn during all tests performed;

- The heater situated on the dryer unit was always switched on once the storage vessel was pumped to ensure that the silica crystals are dry;

- The water flow through the compressor was always initially monitored before switching the compressor on;

- The oscilloscope was set to single shot and was started before any tests were performed, this was done so that the pressure trace for the tests performed can be viewed and recorded.

Appendix B Supersonic Results, Iso Surfaces of Mach number

Iso surfaces for the 90 degree dihedral angle fillet profiles

3% thickness/chord ratio

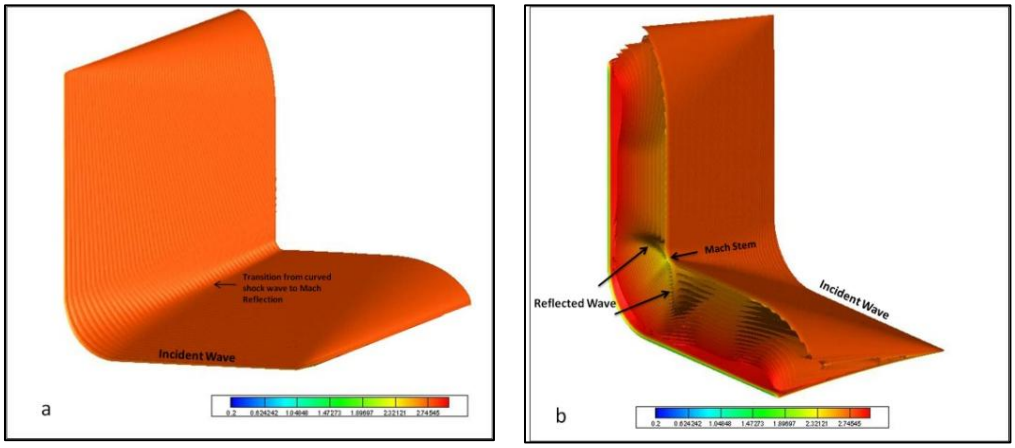

6% thickness/chord ratio

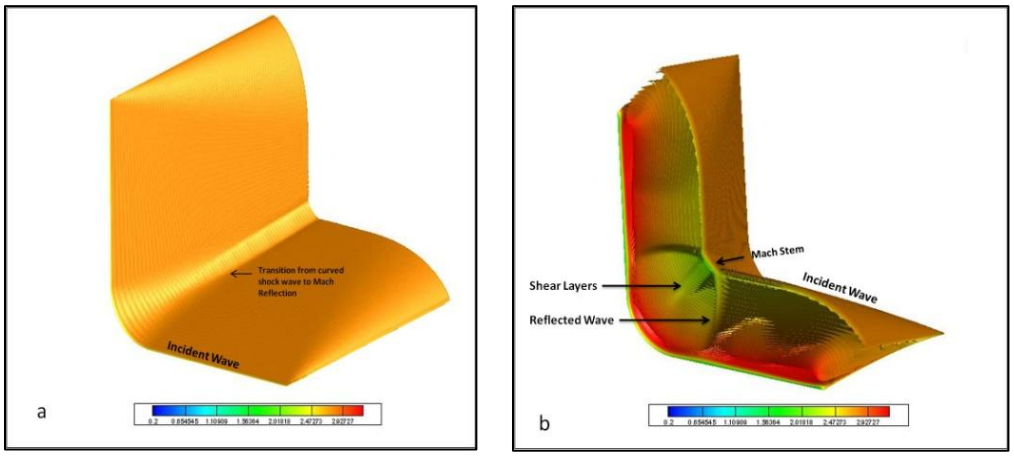

Figure B. 1: Iso surfaces of Mach number for the 90° dihedral angle 3 and 6% thickness/chord ratio fillet profiles, Isometric views, (a) Front, (b) Rear

Iso surfaces for the 120 degree dihedral angle fillet profiles

3% thickness/chord ratio

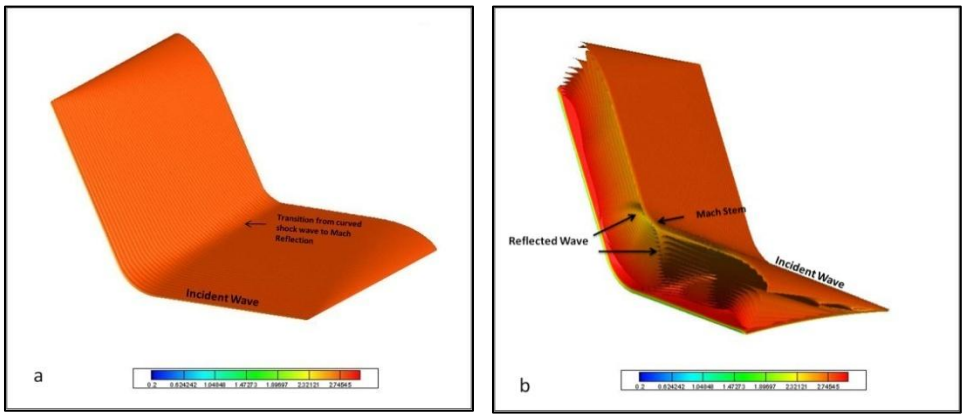

6% thickness/chord ratio

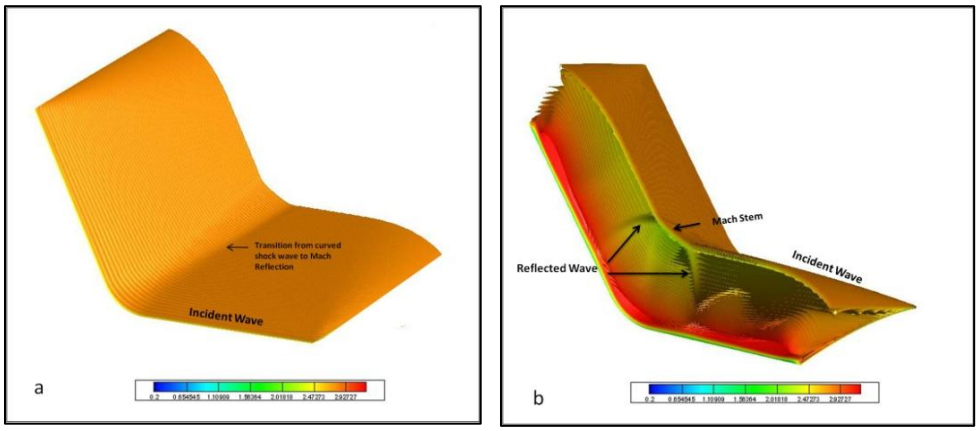

10% thickness/chord ratio

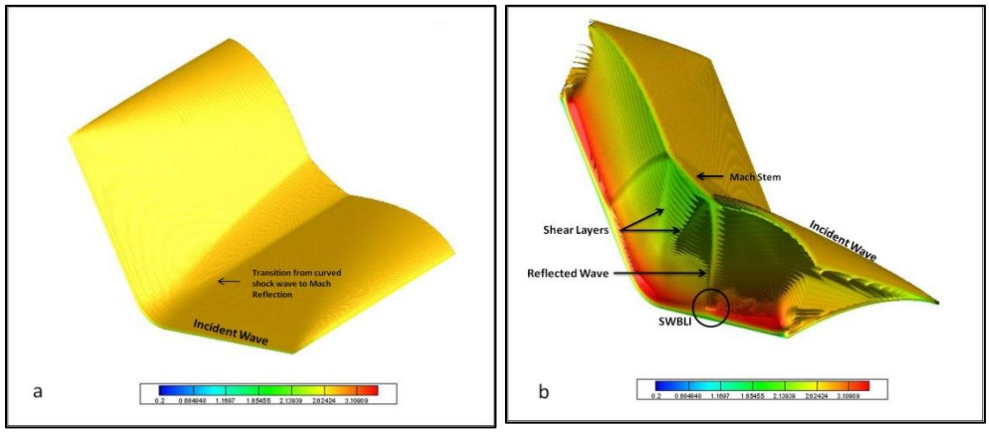

Figure B. 2: Iso surfaces of Mach number for the 120° dihedral angle 3, 6, and 10% thickness/chord ratio fillet geometries, Isometric views, (a) Front, (b) Rear

Iso surfaces for the 135 degree dihedral angle fillet profiles

6% thickness/chord ratio

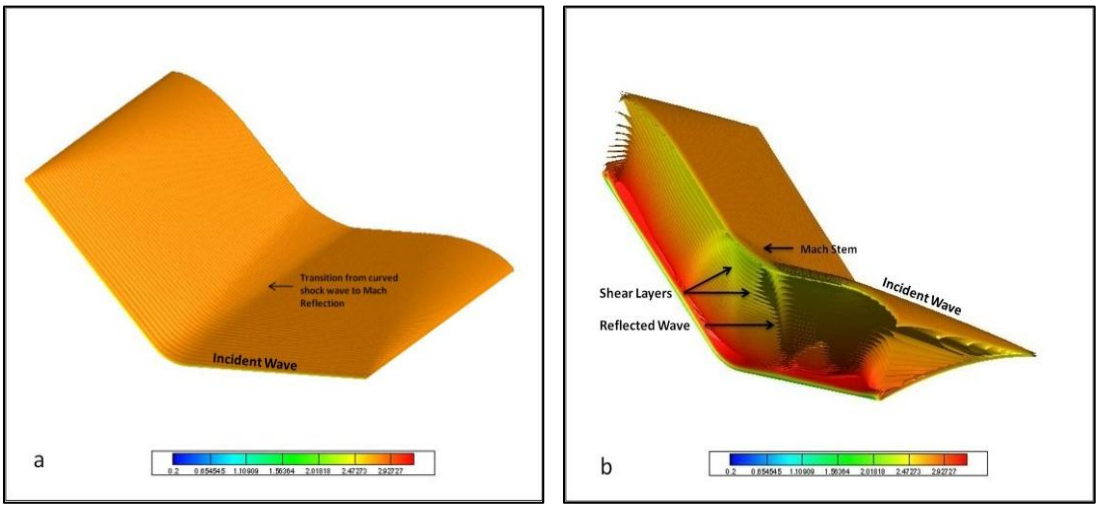

10% thickness/chord ratio

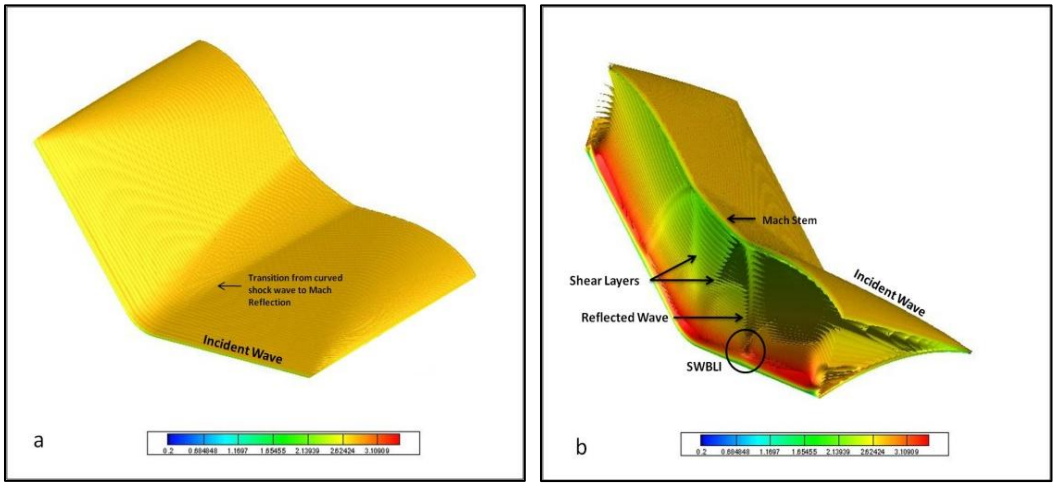

Figure B. 3: Iso surfaces of Mach number for the 135° dihedral angle 6 and 10% thickness/chord ratio fillet geometries, Isometric views, (a) Front, (b) Rear

Iso surfaces for the 90 degree dihedral angle sharp corner profiles

3% thickness/chord ratio

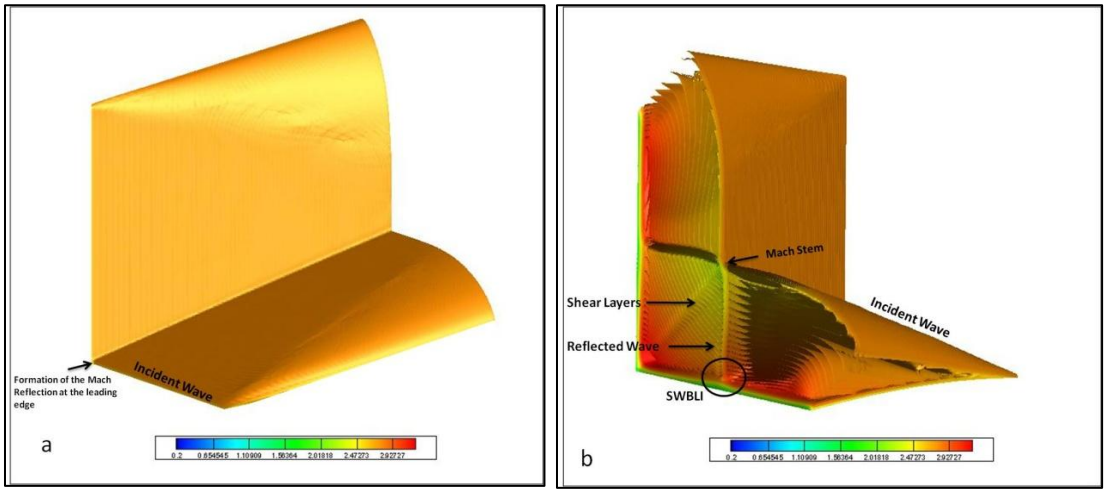

Figure B. 4: Iso surfaces of Mach number for the 90° dihedral angle 3 and 10% thickness/chord ratio sharp corner geometries, Isometric views, (a) Front, (b) Rear

Iso surfaces for the 120 degree dihedral angle sharp corner profiles

3% thickness/chord ratio

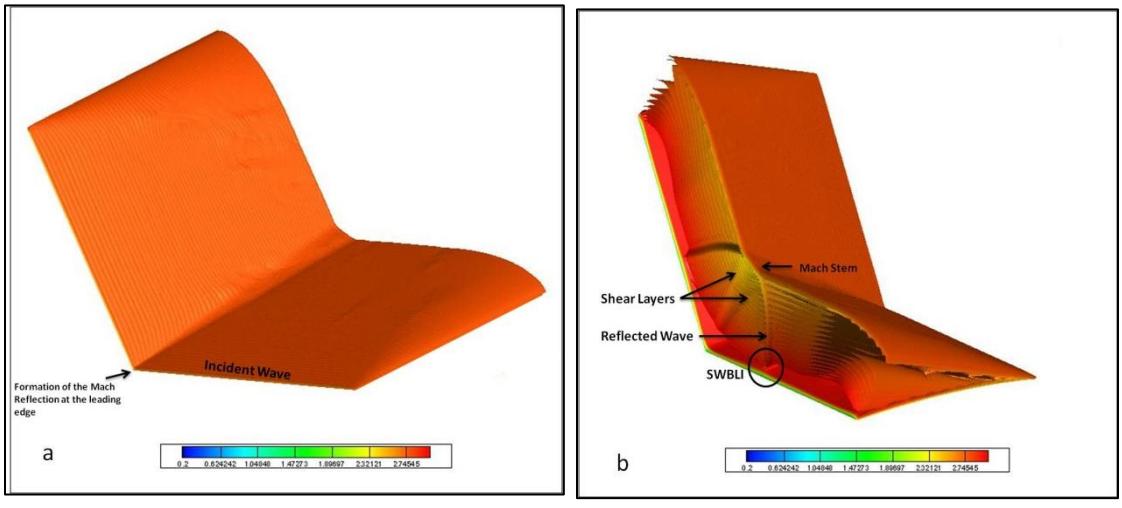

10% thickness/chord ratio

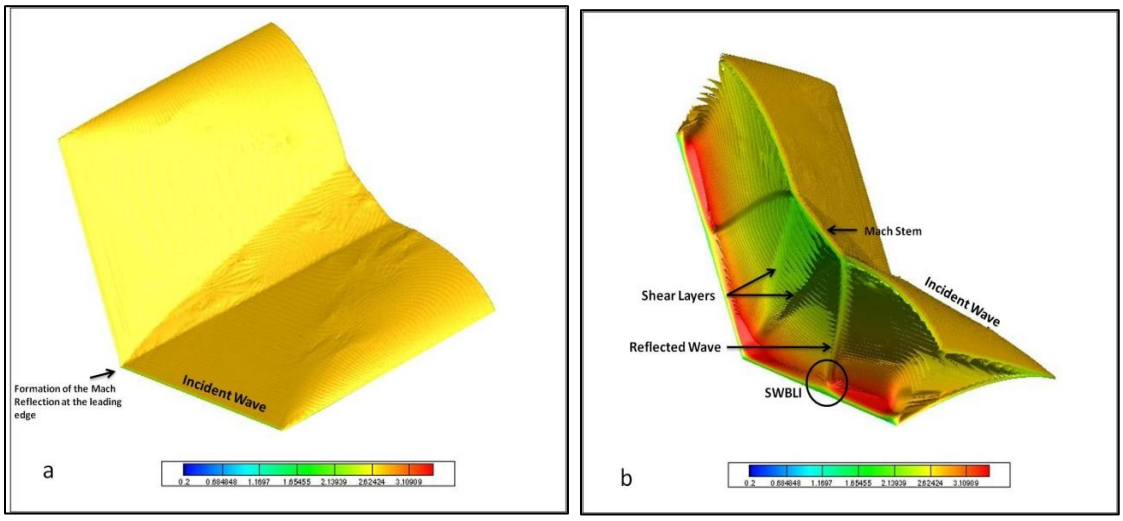

Figure B. 5: Iso surfaces of Mach number for the 120° dihedral angle 3 and 10% thickness/chord ratio sharp corner geometries, Isometric views, (a) Front, (b) Rear

Iso surfaces for the 135 degree dihedral angle sharp corner profiles

3% thickness/chord ratio

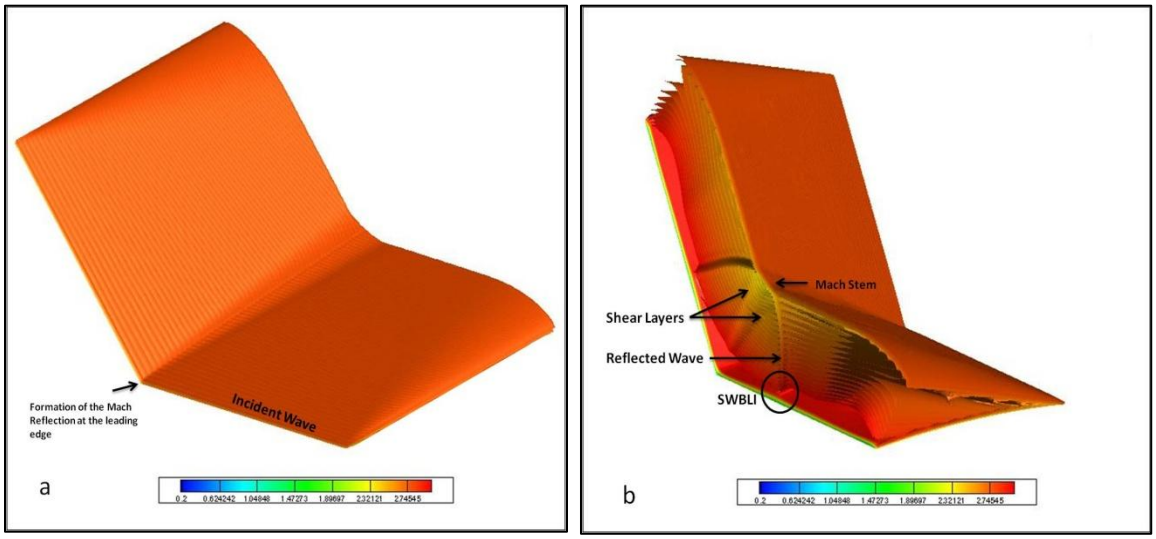

10% thickness/chord ratio

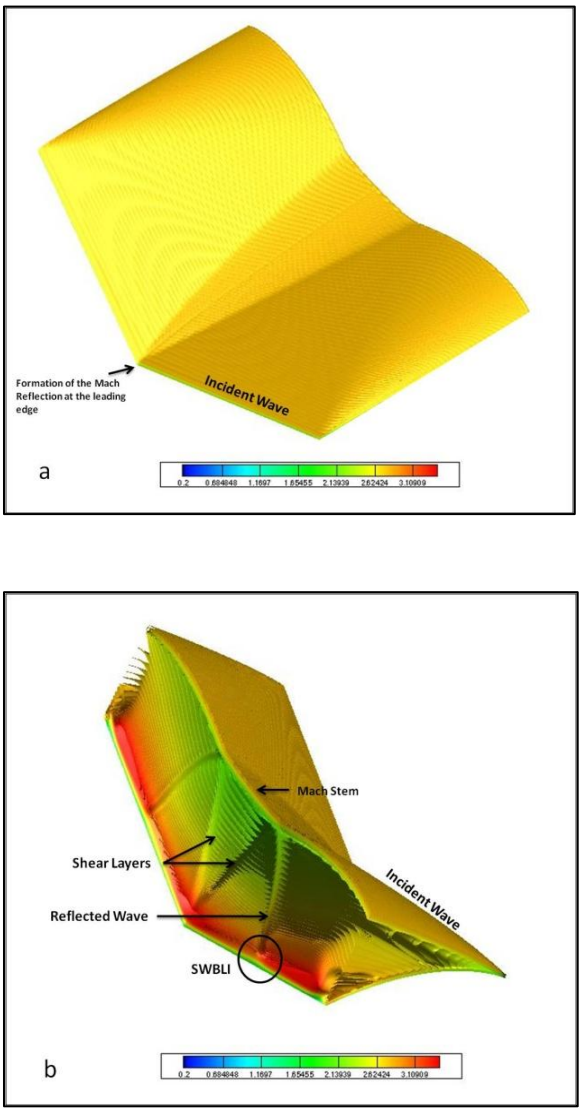

Figure B. 6: Iso surfaces of Mach number for the 135° dihedral angle 3 and 10% thickness/chord ratio sharp corner geometries, Isometric views, (a) Front, (b) Rear

Electronic Appendix